High-efficiency heat transfer devices by innovative manufacturing techniques

Original
High-efficiency heat transfer devices by innovative manufacturing techniques / Ventola, Luigi. - (2016). [10.6092/polito/porto/2644177]

Publisher:
Politecnico di Torino

Published
DOI:10.6092/polito/porto/2644177

Dissertation Politecnico di Torino number : xxxxx

High-efficiency heat transfer devices by innovative manufacturing techniques

A dissertation submitted to

Politecnico di Torino

for the degree of

Doctor of Philosophy (Ph. D. Polytechnic of Turin)

presented by

Luigi Ventola

M.Sc. Politecnico di Torino

born 9th April 1987

citizen of Italy

accepted on the recommendation of

Prof. Dr. Pietro Asinari, tutor

Dr. Eliodoro Chiavazzo, co-tutor

Torino, 2016

To my parents Armando and Antonietta, and my beloved Giovanna

Acknowledgements

I would like to thanks Prof. Pietro Asinari and Dr. Elio Chiavazzo, who supervised my work during last four years. They have guided me during this long time and have been responsible of my scientific and professional growth. I learned so much from them and I show gratitude for that. I am also grateful to Prof. Daniele Marchisio for promoting this collaboration between me and them.

I would thank people that contributed in achieving scientific results reported in this thesis, namely Flaviana Calignano and Diego Manfredi from Italian Institute of Technology, Saverio Fotia and Vincenzo Pugliese from Denso Thermal System S.p.A., and Davide Rondilone from ErreMeccanica S.r.l.

I would like to acknowledge the THERMALSKIN project: Revolutionary surface coatings by carbon nanotubes for high heat transfer efficiency (FIRB 2010 - “Futuro in Ricerca”, grant number RBFR10VZUG); It provided me financial support during my first year of work as a research fellow, paving me the way to the doctorate experience.

Thanks to my parents and grandparents, for their infinite love and support, for educating me toward honest and simple values. No word can ever be enough to express gratefulness for them.

Giovanna, thanks for being always by my side. Your love and your incessant encouragement allowed me to overcome my darkest hours.

I owe a special thanks to Pio and Sara, always so close to me. I wish them will achieve much more important goals than those that I gained.

I would thank my colleagues and friends from Small Lab: Matteo Fasano, Annalisa Cardellini, Uktam Salomov, Masoud Bigdeli e Matteo Morciano, for the happy times we spent together, the mutual support, the edifying suggestions and conversations.

I am happy to mention all students I supervised during their Bachelor and Master thesis work: Francesco Robotti, Masoud Dialameh, Saverio Affuso, Lorenzo Calvara, Davide Canavero, Davide Castignone, Francesca Clerici, Gabriele Curcuruto, Dario Gigliotti, Rocco Innamorato, Li Yue, Francesco Locorotondo, Mimmo Geraci, Luqman Herzallah, Francesco Summa, Fabio Dardano, Nan Zhao, Enrico Treggiari, Tundo Giulia. The mentoring of these young engineers has been among the most beautiful activities of my Doctorate, and I thank them all.

Thanks to Marco Vassallo, Antonio Buffo and Gianluca Boccardo, for their loyal and fraternal friendship.

Ringraziamenti

Ringrazio il Prof. Pietro Asinari e il Dott. Elio Chiavazzo, che hanno supervisionato il mio lavoro negli ultimi quattro anni. Mi hanno fatto da guida durante questo lungo periodo di tempo e sono stati responsabili della mia crescita scientifica e professionale. Ho imparato cosi tanto da loro e gli sono grato per questo. Grazie inoltre al Prof. Daniele Marchisio, che ha promosso la collaborazione fra me e loro.

Vorrei ringraziare le persone che hanno contribuito al raggiungimento dei risultati scientifici riportati in questa tesi, in particolare Flaviana Calignano e Diego Manfredi dell'Istituto Italiano di Tecnologia, Saverio Fotia e Vincenzo Pugliese di Denso Thermal System S.p.A. e Davide Rondilone di ErreMeccanica S.r.l.

Un doveroso riconoscimento da parte mia va al progetto THERMALSKIN: Revolutionary surface coatings by carbon nanotubes for high heat transfer efficiency (FIRB 2010 - “Futuro in Ricerca”, finanziamento RBFR10VZUG), che mi ha fornito il sostegno finanziario durante il mio primo anno di lavoro come assegnista di ricerca, aprendomi la strada all'esperienza di dottorato.

Grazie ai miei genitori e i miei nonni, per il loro infinito amore e comprensione, per avermi educato a perseguire sani e semplici valori. Non basterebberlo le parole per esprimere la gratidudine che provo per loro.

Giovanna, grazie per essere sempre al mio fianco. Il tuo amore e il tuo incoraggiamento incessanti mi hanno permesso di superare i momenti più bui.

Un ringraziamento speciale a Pio e Sara, che mi sono sempre stati cosi vicini. Gli auguro di raggiungere traguardi molto più importanti di quelli ai quali sono arrivato io.

Grazie ai colleghi ed amici dello Small Lab Matteo Fasano, Annalisa Cardellini, Uktam Salomov, Masoud Bigdeli e Matteo Morciano, per i bei momenti passati assieme, il reciproco sostegno, i suggerimenti e le conversazioni edificanti.

Sono anche felice di menzionare tutti gli studenti che ho supervisionato durante la loro attività di tesi: Francesco Robotti, Masoud Dialameh, Saverio Affuso, Lorenzo Calvara, Davide Canavero, Davide Castignone, Francesca Clerici, Gabriele Curcuruto, Dario Gigliotti, Rocco Innamorato, Li Yue, Francesco Locorotondo, Mimmo Geraci, Luqman Herzallah, Francesco Summa, Fabio Dardano, Nan Zhao, Enrico Treggiari, Tundo Giulia. L'attività di tutoraggio di questi giovani ingegneri è stata fra le più belle del mio dottorato, e di questo li ringrazio.

Grazie a Marco Vassallo, Antonio Buffo e Gianluca Boccardo per la loro amicizia leale e fraterna.

Contents

List of Figures

List of Tables

Nomenclature

Symbols

A	surface area $[mm^2]$
Bi	Biot number $[-]$
c_p	specific heat capacity at constant pressure $[J/kg/K]$
D	hydraulic diameter $[mm]$
d	cylinder diameter $[mm]$; protrusion base edge $[mm]$
f	friction factor $[-]$
H	fin/protrusion height $[mm]$
h	convective heat transfer coefficient $[W/m^2/K]$
h_d	hatching distance $[mm]$
I	electrical current $[A]$
K	localized pressure drop coefficient $[-]$
k	core-to-guard thermal transmittance $[W/K]$; slicing direction $[-]$
L	fin length, sensor heating edge $[mm]$
L^*	dimensionless fin length $[-]$
l	cylinder length $[mm]$
m	wave number $[mm^{-1}]$
N	fin/protrusion number $[-]$
Nu	Nusselt number $[-]$
n	direction normal to a sample face $[-]$
P	power $[W]$
Pr	Prandtl number $[-]$
p	pressure $[Pa]$; pitch between neighboring protrusions $[mm]$

Q	heat flux $[W]$
Q_k	conductive heat flux $[W]$
Q_r	radiative heat flux $[W]$
Q_c	convective heat flux $[W]$
q	generic independent quantity $[n.a.]$
q_{loss}	conductive heat loss $[W]$
R_a	average roughness $[\mu m]$
R_p	peak roughness $[\mu m]$
R_z	five-peak-valley roughness $[\mu m]$
R_h	heater electric resistance $[\Omega]$
R_{wire}	wire electric resistance $[\Omega]$
R_{ja}	junction-to-ambient thermal resistance $[K/W]$
R_{jc}	junction-to-case thermal resistance $[K/W]$
R_{cs}	case-to-sink thermal resistance $[K/W]$
R_{sa}	sink-to-ambient thermal resistance $[K/W]$
R_{spr}	spreading thermal resistance $[K/W]$
Re	Reynolds number $[-]$
Re_p^*	modified spacing Reynolds number $[-]$
r	equivalent radius $[mm]$
rs_{angle}	angle between the rough surface and the building platform $[rad]$
S	surface $[m^2]$
S_a	average surface roughness $[\mu m]$
S_{ku}	kurtosis surface roughness $[\mu m]$
S_p	peak surface roughness $[\mu m]$
S_q	root mean square surface roughness $[\mu m]$
S_{sk}	skewness surface roughness $[\mu m]$
s	spacing between neighboring fins/protrusions $[mm]$
T	temperature $[K]$
Tr	convective thermal transmittance $[W/K]$
Tr^0	flat sample convective thermal transmittance $[W/K]$
t	fin thickness $[mm]$
t_b	baseplate thickness $[mm]$
V	volume $[cm^3]$, electric potential difference $[V]$
$\dot{V}$	volumetric flow rate $[m^3/s]$
v	velocity $[m/s]$
y_0	viscous length $[mm]$
Y_0	average viscous length $[mm]$
W	baseplate width $[mm]$

Greek symbols

α	significance level $[-]$; air thermal diffusivity $[m^2/s]$
Δh	centerline-to-average convective correction term $[W/m^2/K]$
ΔNu_L	centerline-to-average Nusselt number correction term $[-]$
ϵ	dimensionless contact radius $[-]$, emissivity $[-]$
η	fin efficiency $[-]$
η_A	aerothermal efficiency $[-]$
ϑ	DMLS slicing-to-normal direction angle $[rad]$
κ	Von Kármán's constant $[-]$
λ	thermal conductivity $[W/m/K]$
λ_a	thermal conductivity of air $[W/m/K]$
λ_{Cu}	thermal conductivity of copper $[W/m/K]$
λ_p	plane solidity $[-]$
μ	dynamic viscosity $[kg/m/s]$
ν	kinematic viscosity $[m^2/s]$
ρ	density $[kg/m^3]$
Σ	standard uncertainties $[n.a.]$
$\Sigma_{h,B}$	type B standard uncertainties on h $[W/m^2/K]$
σ_B	Stefan-Boltzmann constant $[W/m^2/K^4]$
$\sigma_{h,B}$	type B relative standard uncertainties on h $[\%]$
$\sigma_{h,A}$	type A relative standard uncertainties on h $[\%]$
σ_h	overall relative standard uncertainties on h $[\%]$
σ	ratio between open channel area and heat sink frontal area $[-]$
τ	dimensionless plate thickness $[-]$, shear stress $[N/m^2]$
χ	empirical parameter for spreading resistance $[-]$
Ψ	dimensionless spreading resistance $[-]$

Subscripts and superscripts

a	air
app	apparent
ax	axial
av	average
B	Blasius
b	baseplate
bp	bypass
C	contraction
c	sample centerline; commercial heat sink
ch	channel
D	hydraulic diameter
d	approach; downstream
E	expansion
exp	experiment
f	fins
fg	G-10 fiberglass epoxy
$fluid$	FC-72 fluorocarbon liquid
g	guard (sensor)
$g1$	upstream guard (sensor)
$g2$	downstream guard (sensor)
hs	heat sink
h	heater
i	index of the i-th quantity/sample
j	junction
L	sensor heating edge
m	adiabatic mixing
n	root surface
q_i	i-th independent quantity
ref	reference
s	heat source, sample
u	upstream
W	working
w	wall
$+$	turbulence dimensionless quantities

1. Introduction

Enhancing efficiency of heat transfer processes and devices is fundamental in a plenty of the technological applications. Some meaningful examples are thermal management of electronic devices [13], air conditioning and refrigeration [14], and blades cooling for gas turbine engines [15].

Concerning electronic devices, their progressive size reduction and increase in computational performances is inevitably leading to a crucial heat dissipation issue in designing novel components [16]. In spite liquid [17, 18] and two-phase [19, 20] solutions have been investigated, cooling strategies based on air are expected to remain a rather convenient and popular approach in the next future, due to their low cost and reliability [21]. These are the so-called *heat sinks*.

With regard to air conditioning and refrigeration applications, these usually rely on compact heat exchangers [22]. The latter continuously request for enhancement in heat transfer efficiency, in order to reduce costs, weight and footprint. These requirements are very important in transportation sector (e.g. automotive, aerospace), where reduction of weight and footprint of air conditioning and refrigeration components can lead a reduction in pollutants and green-house gas emissions.

About gas turbine engines, air under forced convection is used for blade cooling system in nearly all the practical applications. Due to low thermal conductivity of air, state-of-the-art blade cooling systems rely on peculiar techniques to enhance convective heat transfer of air under forced regime [23]. For example, *protrusions* called *pin fins* are used to augment heat transfer on trailing edge by promoting turbulence and mixing.

The importance of high efficiency heat transfer in a variety of technological fields has incessantly fed the investigation in enhanced heat transfer. In order to increase heat transfer efficiency of heat exchangers and devices, a variety of techniques have been investigated in last decades [24]. This thesis work focuses on heat transfer enhancement techniques under forced air convection. Concerning forced convection regime, many augmentation techniques have been already proposed [25], including plane fins [26, 27], pin fins [28–30], dimpled surfaces [31–33], surfaces with arrays of protrusions [34, 35], metal foams [36], and scale roughened surfaces [37]. The key idea behind all the aforementioned heat transfer enhancement techniques is patterning surfaces devoted to heat transfer in order to (i) increase heat transfer surface area, and (ii) induce fluid dynamic effects aiming to enhance convective heat transfer coefficient [38]. As a consequence, geometrical design is fundamental to achieve high efficiency in heat transfer [38], and manufacturing techniques guaranteeing high geometrical flexibility in fabricating parts (devices) made of high thermally conductive bulk material, e.g. metal, are claimed to have tremendous potential in design of high efficiency heat transfer devices. Among them, 3D printing technologies (also referred to as additive manufacturing - AM) for metal materials, seem to be promising in thermal applications [39]. Nowadays, AM is an economical way to fabricate single items, small batches, and, potentially, mass-produced items, and it is used in particular by large aerospace companies. For example, GE Aviation™ (a General Electrics™ branch) produces a huge number of metallic parts for gas turbine engines, including turbine blades by direct metal laser sintering (DMLS). As previously pointed out, thermal management of turbine blades is a challenging issue. Consequently, investigation of AM peculiarities (e.g. complex shapes) devoted to heat transfer augmentation is highly desirable.

The present work aims to face the incessant need of high efficiency heat transfer solutions requested by many technological fields. Thermal fluid-dynamics features of both traditional and advanced heat transfer devices are studied, and novel optimization strategies are developed. Moreover, AM techniques are used to design high efficiency heat transfer devices, through ”think additive” attitude, i.e. exploitation of peculiar features of AM not allowed by traditional techniques. Content of the thesis is synthesized in Fig. 1.1. In particular, in Chapter 2, the efficiency-to-cost optimization of an industrial heat exchanger, namely a plate fins *heat sink* fabricated by extrusion, is faced. Taking into account the dimensions and shape constrains associated to extrusion process, a geometrical optimization procedure is applied on a heat sink from a real industrial application in automotive field. This study relies on an experimental campaign carried on by DENSO™ Thermal System in their laboratories [1]. Then, an in house experimental test bench has been developed to experimentally investigate advanced heat transfer enhancement methods. This experimental rig is introduced in Chapter 3. A novel sensor based on ”thermal guard” for convective heat fluxes measurements has been conceived, designed and validated [4]. That is used to measure small heat fluxes (air cooled applications) on small size heat transfer surfaces (i.e. *micro-structured* surfaces, such as artificial roughness, micro-protruded patterns and pin fins) and heat exchangers (e.g. heat sinks) as follows: In Chapter 4, patterns of *micro-pin fins* (i.e. *micro-protrusions*) on flush mounted heat sinks are investigated as a heat transfer enhancement technique. The effect of geometrical and fluid-dynamics lengths is highlighted. Moreover a methodology suited for efficiency-to-cost optimization of these micro-protruded patterns by ”not subtractive” technologies (e.g. AM) is designed and tested with regard to a commercial available pin fin heat sink [7].

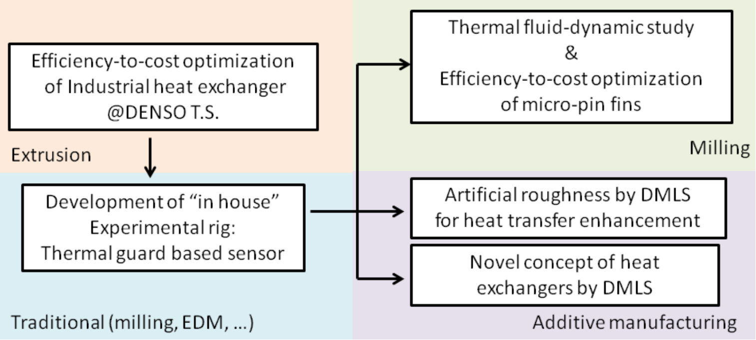

Figure 1.1: Thesis contents are summarized in five conceptual pillars. Study of an industrial heat exchanger motivates the design of an *ad hoc* experimental rig. That allows investigation of various heat transfer enhancement methodologies. Colors aim to distinguish different manufacturing techniques involved in each activity.

In Chapter 5, DMLS is exploited to fabricate high efficiency heat transfer surfaces, taking advantage of *artificial roughness* under fully turbulent regime. DMLS technique is introduced in detail, and rough surfaces morphology, radiative and convective heat transfer features are characterized. Finally, experimental evidences are reported on the potential of DMLS in manufacturing flat and finned heat sinks with a remarkably enhanced convective heat transfer coefficient [3]. In Chapter 6 a novel heat exchanger is designed. Due to its *unusual morphology*, this device is extremely challenging to be fabricated by traditional manufacturing techniques. Here it is easily manufactured in one step by DMLS. Remarkable heat transfer efficiency is achieved. More important, it demonstrates additive manufacturing can lead a revolution in conceiving heat transfer devices, when its *extreme flexibility in shapes* is fully exploited through ”think additive” approach [10]. Finally, Conclusions and perspectives of this work are drawn in Chapter 7.

2. Optimization of traditional heat exchanger: extruded heat sink

In this chapter, a comprehensive thermal model for plate fin heat sinks (PFHS) is presented and used to optimize heat transfer efficiency of extruded heat sink from a real industrial application in automotive sector. The model has a broad field of applicability, being comprehensive of the effects of flow bypass, developing boundary layer, fin efficiency and spreading resistance. Experimental data are used to validate the proposed thermal model, and demonstrate its accuracy. An optimization methodology based on genetic algorithms is proposed for efficiency maximization. The latter maximize the efficiency-to-cost ratio of the heat transfer device, to guarantee a cost-effective selection of the design parameters of PFHS. Such optimization methodology is then tested on a commercial heat sink, resulting in a possible 64% cost reduction at fixed thermal performances. Contents of this Chapter can be also found in [1].

2.1. Motivations

In Chapter 1 thermal problems concerning electronic cooling have been discussed and importance of cooling strategies based on air cooled heat sinks has been argued. In particular, heat sinks with plate fins are among the most common and studied thermal management solutions for electronic and automotive devices [40, 41]. Plate fin heat sinks (PFHS) differ in manufacturing methods (stamping, extrusion, bonding, folding, additive manufacturing), type of coolant (air, liquid), material (aluminum, copper, alloys, polymeric or composite materials) and flow regime (natural, forced) [42]. Nowadays, the metal extruded, air-cooled heat sinks are the most widespread solution, being a satisfactory compromise between costs and thermal performances [42, 43], both in *active* (purposely designed fan) and *semi-active* (fan already existing in the system) configurations. However, the choice of the heat sink characteristics maximizing thermal performances and minimizing production and operating costs for a particular application may be extremely complex, due to the multiple design options and restraints to be considered at the same time.

In the last decades, many studies focused on a more fundamental understanding of the thermal and fluid-dynamics phenomena involved in air-cooled PFHS have been carried out [44–50]. In particular, the main phenomena to be taken into account for a comprehensive thermal model are (1) base-to-fins spreading resistance, (2) thermal conduction through fins, (3) boundary layer development along fins, and (4) flow bypass (in case of unshrouded heat sinks) [42].

Starting from an adequate thermal and fluid-dynamic model, the optimal configuration for the air-cooled PFHS can be then investigated. To this purpose, conventional thermal analysis tools are usually inadequate, because both geometry and boundary conditions are not known *a priori*. Therefore, numerous optimization procedures have been proposed in the last years [51–57]. One of the most valid studies on this topic has been conducted by Culham *et al.* [58], where a thermal model for shrouded (i.e. no flow bypass) heat sinks and an optimization procedure based on entropy generation minimization have been coupled. However, optimization strategies based on entropy generation minimization only focus on operating costs, while neglecting production ones. This may lead to oversizing the heat sink, which implies an increased amount of material and thus production costs [59].

Here, both a thermal model and a methodological approach to designing air-cooled PFHS, which allow to optimize the production costs at given thermal performances, are presented. First, a comprehensive thermal model suited for unshrouded heat sinks is developed, considering the effect of flow bypass, developing boundary layer along fins, heat conduction through fins and base-to-fins spreading resistance. It is worth to stress that the proposed thermal model has rather general validity, being easily applicable also to shrouded heat sink (no flow bypass). Second, this thermal model is validated by the experimental characterization of a commercial heat sink for the thermal management of HVAC control unit in the automotive field. Finally, the thermal model is coupled to an optimization procedure based on genetic algorithms, in order to find the optimal geometric parameters of PFHS in *semi-active* configurations. That procedure is rather general, taking into account both the full range of possible working conditions and the technological constrains due to the adopted manufacturing process (e.g. extrusion, additive manufacturing). In particular, this optimization methodology is adopted to find the most cost-effective configuration for the considered commercial heat sink in a *semi-active* configuration.

2.2. Theoretical model for PFHS

A comprehensive model for predicting the thermal and fluid-dynamic behavior of air-cooled, unshrouded PFHS under forced convection regime is here introduced [1].

As schematically depicted in Fig. 2.1, the heat sink geometry considered in this work is characterized by L, H, t, and N parameters, which are the fins length, height, thickness and number, respectively. Moreover, W and t_b are the base plate width and thickness, while s is the spacing between neighboring fins.

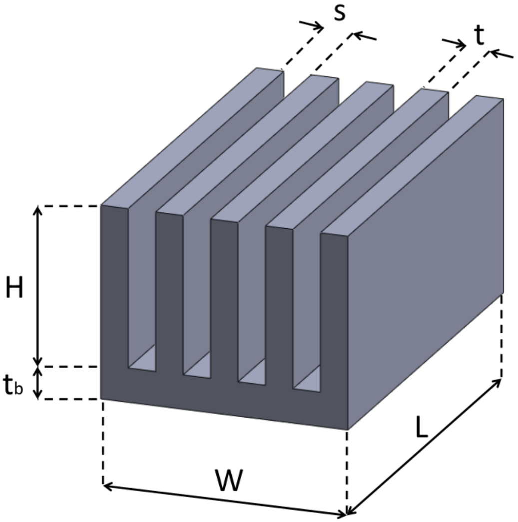

Figure 2.1: Heat sink geometry (See Ref. [1]).

The effectiveness of heat dissipation by heat sinks depends on their effective thermal resistance, which is given by the overall effect of thermal resistances along the heat flux path, from the source to the ambient. Here, the overall junction-to-ambient thermal resistance (R_{ja}) of the electronic package is estimated relying on the classical equivalent thermal resistance network depicted in Fig. 2.2 [42].

In fact, despite the film resistance at the fluid-solid boundary usually dominates, it has been demonstrated that the effect of other resistance elements on the heat path cannot be safely neglected in the optimization of the design characteristics of heat sinks [58].

Therefore, R_{ja} is here decomposed in four discrete components, namely:

$$R_{ja} = R_{jc} + R_{cs} + R_{sa} + R_{spr}, \tag{2.1}$$

where R_{jc}, R_{cs}, R_{sa}, and R_{spr} are the junction-to-case, case-to-sink, sink-to-ambient, and spreading resistances, respectively.

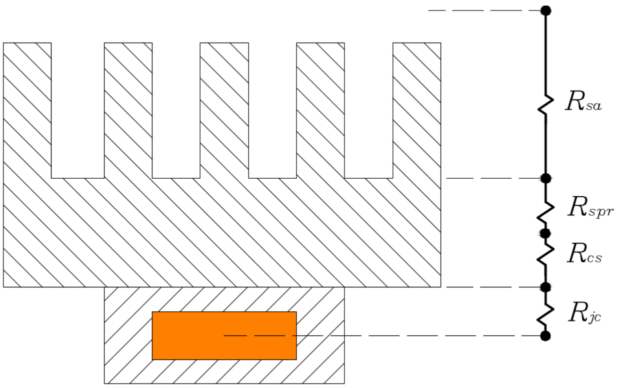

Figure 2.2: Scheme of the thermal resistance network of the considered heat sink (See Ref. [1]).

First, in most applications R_{jc} is given by the manufacturer, who provides the electronic components already embedded into the cases. Hence, R_{jc}

is not directly modeled here, being specific to the considered application and usually experimentally known.

Second, case-to-sink resistance R_{cs} is calculated as:

$$R_{cs} = \frac{t_b}{\lambda A_b}, \tag{2.2}$$

where λ is the thermal conductivity of the heat sink, t_b and A_b are the thickness and cross section surface area of base plate.

Sink-to-ambient resistance R_{sa} is then computed by analytically modeling the air flow and pressure drops across the unshrouded heat sink. Note that the following considerations are safely applicable to any type of flow bypass (top, side or both) or to fully shrouded configurations. Fig. 2.3 reports the average air flow velocities in the different sections of the duct where heat sink is placed, namely: the approach velocity (v_d) at the entrance of the duct; the channel velocity (v_{ch}) through the channels made by neighboring fins (fin channels); the bypass velocity (v_{bp}) in the section of the duct not occupied by the heat sink.

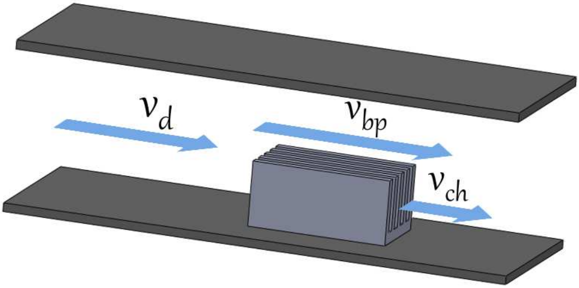

Figure 2.3: Scheme of the bypass phenomenon (See Ref. [1]).

The air flowing through the fin channels experiences pressure drops due to contraction and expansion of the flow field at channel inlet and outlet, respectively. Let us introduce the cross section area of the duct A_d, and the overall cross section area of the fin channels $A_{ch} = (N-1)sH$. The air flow velocities in the different sections of the duct can be therefore obtained by applying the conservation of mass and momentum in the duct [60], namely:

$$\begin{cases} v_d A_d = v_{ch} A_{ch} + v_{bp}(A_d - A_{ch}) \\ \frac{1}{2}\rho v_{bp}^2 = \frac{1}{2}\rho v_{ch}^2 + \Delta p_{hs}, \end{cases} \tag{2.3}$$

where ρ is the air density and Δp_{hs} is the pressure drop experienced by air flowing through fin channels. The latter quantity can be decomposed as:

$$\Delta p_{hs} = \left(K_C + K_E + 4 f_{app} \frac{L}{D_{ch}} \right) \rho \frac{v_{ch}^2}{2}, \tag{2.4}$$

where K_C and K_E are the contraction and expansion pressure drop coefficients, f_{app} is the apparent friction factor coefficient for developing laminar flows and $D_{ch} = 2s$ is the hydraulic diameter of the fin channel.

K_C and K_E take into account the pressure drops generated by the contraction and expansion of flow field at the inlet and outlet of fin channels, respectively. It can be demonstrated that $K_C = 0.42(1 - \sigma^2)$ and $K_E = (1 - \sigma^2)\sigma^2$, where $\sigma = 1 - NtW^{-1}$ is the ratio between open channels area and overall frontal area of the heat sink [61]. f_{app} allows to evaluate the pressure drop experienced by air while flowing through the fin channel, and it can be computed as [62]:

$$f_{app} = \frac{\left[\frac{11.8}{L^*} + (f Re_{ch})^2 \right]^{\frac{1}{2}}}{Re_{ch}}, \tag{2.5}$$

where $Re_{ch} = \rho v_{ch} D_{ch} \mu^{-1}$ is the channel Reynolds number and μ the air dynamic viscosity; $L^* = L(D_{ch} Re_{ch})^{-1}$ is the dimensionless fin length, whereas the friction factor for fully developed channel flows is:

$$f = \frac{24 - 32.53\left(\frac{s}{H}\right) + 46.72\left(\frac{s}{H}\right)^2 - 40.83\left(\frac{s}{H}\right)^3 + 22.96\left(\frac{s}{H}\right)^4 - 6.09\left(\frac{s}{H}\right)^5}{Re_{ch}}. \tag{2.6}$$

Once the fluid-dynamics quantities within the duct have been fully determined, the sink-to-ambient thermal resistance can be finally computed as:

$$R_{sa} = \frac{1}{\eta h A_{hs}}, \tag{2.7}$$

being A_{hs} the total heat sink surface involved in the convective heat transfer, h the average convective heat transfer coefficient and η the fin efficiency. The average convective heat transfer coefficient can be calculated as:

$$h = \frac{Nu_s \lambda_a}{s}, \tag{2.8}$$

where λ_a is the thermal conductivity of air and Nu_s can be estimated as

$$Nu_s = \left[\frac{1}{\left(0.5 Re_s^* Pr\right)^3} + \frac{1}{\left(0.664 \sqrt{Re_s^*} Pr^{\frac{1}{3}} \sqrt{1 + 3.65 (Re_s^*)^{-\frac{1}{2}}}\right)^3} \right]^{-\frac{1}{3}} \tag{2.9}$$

in the range $0.1 < Re_s^* < 100$ [63]. In Eq. 2.9, $Re_s^* = 0.5 Re_{ch} s L^{-1}$ is the modified spacing Reynolds number, $Pr = \mu c_{p,a} / \lambda_a$ is the Prandtl number and $c_{p,a}$ is the specific heat capacity at constant pressure for the flowing air. The fin efficiency can be then determined as [63]

$$\eta = \frac{\tanh \sqrt{2 Nu_s \lambda_a H^2 (t + L) / (\lambda s t L)}}{\sqrt{2 Nu_s \lambda_a H^2 (t + L) / (\lambda s t L)}}. \tag{2.10}$$

It is worth to note, in case of unshrouded heat sinks, the main effect of enhancement in pressure drops induced by the heat sink Δp_{hs} (e.g. due to reduction of spacing between fins s, hence reduction in A_{ch}) is to reduce air velocity over the fins v_{ch} and increase bypass velocity v_{bp} (See Eq. 2.3 and Fig. 2.3). As a consequence of diminishing v_{ch}, convective heat transfer coefficient drops down according Eq. 2.9. That can be interpreted as follows: If heat sink package became too dense (i.e. s reduces) air flow avoids fin surface and pass through the portion of duct cross section not occupied by heat sink. As a result, in unshrouded configuration, increase in Δp_{hs} generally could not lead to significant increase pressure drops along the air circuit, but could lead instead to a significant reduction in heat sink thermal performances (i.e. convective heat transfer). Hence, relying on the proposed model, evaluation of thermal parameters implicitly takes into account pressure drops too.

The fourth thermal resistance considered in the model depicted in Fig. 2.2 takes into account the spreading resistance between the heat source and the base plate of heat sink. As sketched in Fig. 2.4, spreading resistance occurs in configurations where heat flows from a small heat source to the base of a larger heat sink. In this way, the heat cannot uniformly distribute through the base plate, therefore limiting the convective cooling effect by the fins.

Spreading resistance is progressively becoming an important issue in modern microelectronics, and it can be mitigated by either increasing the thickness of the base plate or by adopting materials with higher thermal conductivity (e.g. novel micro- and nano-structured materials [64]). Here, a perfect thermal contact between case and heat sink base plate (i.e. negligible thermal contact resistances) is assumed, and R_{spr} is estimated following the work by Lee *et al.* [65], where further details are available. Let us define the base plate and heat source (i.e. case) equivalent radii as $r_b = \sqrt{A_b/\pi}$ and $r_s = \sqrt{A_s/\pi}$, respectively, where A_s is the cross section area of the heat source.

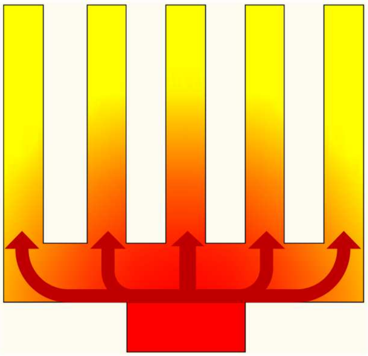

Figure 2.4: Scheme of heat spreading phenomenon in a PFHS: red and yellow represent high and low temperature regions, respectively; arrows represent heat propagation paths (See Ref. [1]).

Moreover, let us introduce the dimensionless contact radius (ϵ) and plate thickness (τ):

$$\epsilon = \frac{r_s}{r_b}, \tag{2.11}$$

$$\tau = \frac{t_b}{r_b}. \tag{2.12}$$

Considering the dimensionless Biot number of the base plate as $Bi_b = hr_b/\lambda$, it is possible to calculate the dimensionless spreading resistance $\Psi = \Psi(\epsilon, \tau, Bi_b)$ as:

$$\Psi = \frac{1}{2}(1-\epsilon)^{3/2}\frac{\tanh(\chi\tau) + \frac{\chi}{Bi_b}}{1 + \frac{\chi}{Bi_b}\tanh(\chi\tau)}, \tag{2.13}$$

where $\chi = \chi(\epsilon)$ is an empirical parameter found as $\chi = \pi + (\sqrt{\pi}\epsilon)^{-1}$ [65]. Finally, the spreading resistance R_{spr} is calculated as:

$$R_{spr} = \frac{\Psi}{\lambda\sqrt{A_s}}. \tag{2.14}$$

Even though the overall thermal resistance model for R_{ja} has been developed for unshrouded heat sinks, it is worth to stress that it has general validity. In fact, it can be easily applied to shrouded heat sinks, by neglecting bypass phenomenon.

2.3. Experimental validation of model

Experiments are carried out to validate the comprehensive thermal model of the heat sink discussed in Section 2.2. In particular, a commercially available PFHS (DENSO™ Thermal Systems) is considered as a representative case study. The experimental measurements of the junction-to-ambient thermal resistance ($R_{ja,exp}$) are then compared with the modeling predictions ($R_{ja,model}$), at different approach velocities (v_d) in a *semi-active*, unshrouded configuration.

Table 2.1: Geometrical parameters of the commercially available heat sink experimentally tested (See Ref. [1]).

L [mm]	W [mm]	t_b [mm]	N [mm]	H [mm]	t [mm]	s [mm]
57.2	41.4	8.4	14	21.8	1	2.1

The geometrical parameters of the sample heat sink experimentally tested are reported in Tab. 2.1. The considered heat sink is made out of extruded AL EN AW 6060 aluminum alloy, and it is currently used for the heat dissipation of power transistors for the air flow control in HVAC.

The experimental campaign has been designed to thermally characterize the heat sink in the full range of typical working conditions. Test have been performed by DENSO™ Thermal Systems in their laboratory for experimental characterization of HVAC unit located in Poirino, Turin, Italy. During the tests, the heat sink is flush mounted on one wall of the HVAC rectangular air duct (cross section area $A_{duct} = 97.67$ cm^2), which usually feeds the vehicle passenger area. Hence, the heat sink is tested (and it usually operates) in a *semi-active* configuration, i.e. it takes advantage of an existing fan in the HVAC.

The experimental rig used to test HVAC, hence to characterize the heat sink, is described in the following: air at ambient temperature enters from the rig inlet pipe of diameter 150 mm, where air flow rate is measured; Then air flow enters in a plenum chamber of dimensions 2 x 2 x 1.5 m; Finally, air flow passes through a feeding branch and enters in the HVAC. HVAC fan is used to flow the air through the experimental rig and into the HVAC itself.

The transistor voltage drop (V), electric current (I), junction temperature (T_j), and temperature of air approaching heat sink (T_a) are measured by a Graphtec™ GL220 data logger. Type T thermocouples are used for temperature measurements. Consequently, power supplied to the transistor ($P = VI$) and thermal resistance $R_{ja,exp} = (T_j - T_a)/P$ can be calculated.

Air flow is measured by orifice plate method. An AISI 304 steel plate is inserted in the inlet pipe. Orifice in the plate has a diameter of 79 mm. Pressure taps are inserted upstream and downstream the plate, so that differential pressure can be measured by a Fuji electric™ FKK differential pressure transmitter. By measuring differential pressure, volumetric air flow rate ($\dot{V}$), can be easily calculated [66]. Finally, the approach velocity can be calculated as $v_d = \dot{V}/A_{duct}$.

A schematic of the experimental rig is shown in Fig. 2.5, while experimental results are reported in Tab. 2.2.

Modeling predictions are then obtained relying on $R_{ja,model} = R_{jc} + R_{cs} + R_{sa} + R_{spr}$, as described in Section 2.2. First, $R_{jc} = 0.5$ K/W is considered, as suggested by the manufacturer of the power transistor, which is embedded into the case. Second, R_{cs} is calculated from Eq. 2.2, considering $A_b = LW = 23.68$ cm^2 and $\lambda = 209$ W/m/K. Third, R_{sa} is calculated by means of Eqs. 2.3 - 2.10, considering $c_{p,a} = 1013.4$ J/kg/K, $\lambda_a = 0.0259$ W/m/K, $\rho = 1.1794$ kg/m^3, and $\mu = 1.8415\ 10^{-5}$ kg/m/s. It is worth mentioning that the lateral area of the base plate is not involved in the heat transfer phenomenon, because the heat sink is flush mounted on the wall during the experiments. Consequently, the overall heat transfer area A_{hs} can be calculated as:

$$A_{hs} = WL + 2(L + t)HN, \tag{2.15}$$

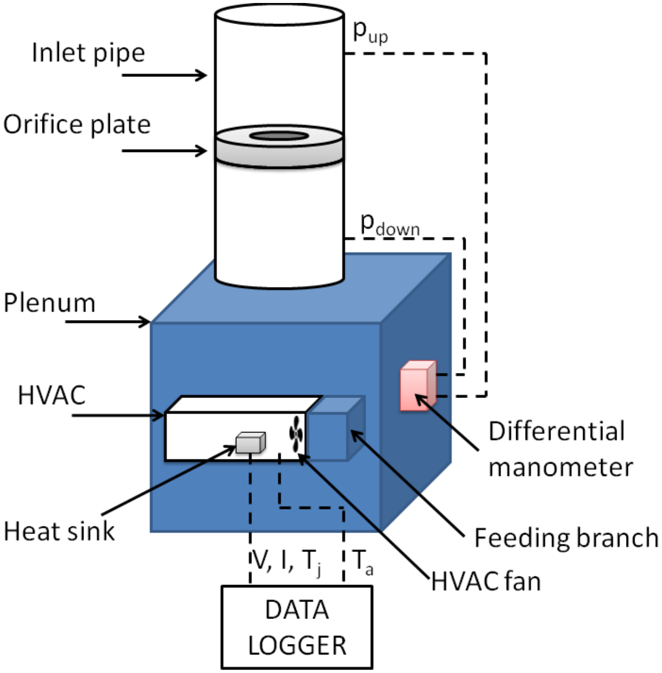

Figure 2.5: Schematic of experimental test rig used for heat sink characterization. Facility belongs to DENSO™ Thermal Systems laboratories located in Poirino, Turin, Italy (See Ref. [1]).

while the overall heat sink volume (V) as:

$$V = WLt_b + NtLH. \tag{2.16}$$

Finally, R_{spr} is calculated by Eqs. 2.11 - 2.14, considering $A_s = 1.555$ cm^2.

Experimental results and model predictions are compared in Tab. 2.3 and Fig. 2.6. It can be noticed that model predictions for R_{ja} values are systematically higher than experimental measures. This may be due to the partial dissipation of P by both radiative (from heat sink to duct walls) and conductive (through the transistor case holder) heat transfer mechanisms. As a first approximation, radiative and conductive heat transfer phenomena have been neglected in the thermal model presented in Section 2.2. In fact, the extruded aluminum alloy has low emissivity (≈ 0.1

Table 2.2: Experimental results for the commercially available heat sink (See Ref. [1]).

$\dot{V}$ [m^3/s]	P [W]	T_j [°C]	T_a [°C]	v_d [m/s]	$R_{ja,exp}$ [K/W]
0.136	60.24	84.4	26.5	13.9	0.96
0.125	76.3	104.3	26.1	12.8	1.02
0.112	85.07	118	25.8	11.5	1.08
0.099	87.32	121.9	25.1	10.2	1.11
0.086	82.36	118.7	24.8	8.8	1.14
0.070	71.4	111	24.2	7.2	1.22
0.054	56.64	98.1	23.8	5.6	1.31
0.036	38.15	86.1	23.1	3.6	1.65

Table 2.3: Comparison between experimental results ($R_{ja,exp}$) and model predictions ($R_{ja,model}$) on the considered commercial heat sink for different values of approach velocity (v_d), with corresponding percent deviations between model and experiments (See Ref. [1]).

v_d [m/s]	$R_{ja,exp}$ [K/W]	$R_{ja,model}$ [K/W]	Deviation [%]
13.9	0.96	1.18	22.9
12.8	1.02	1.20	17.3
11.5	1.08	1.23	13.5
10.2	1.11	1.26	13.9
8.8	1.14	1.31	14.7
7.2	1.22	1.38	13.4
5.6	1.31	1.49	13.7
3.6	1.65	1.79	8.4

[43, 67]), whereas the base plate heat sink and transistor case are mounted in a thermally insulating plastic holder.

Nevertheless, despite convection is the main heat transfer mechanism occurring in flush mounted heat sinks, neglecting radiative and conductive heat transfer contributions in the experiments leads to slightly underestimate the overall thermal resistance $R_{ja,exp}$.

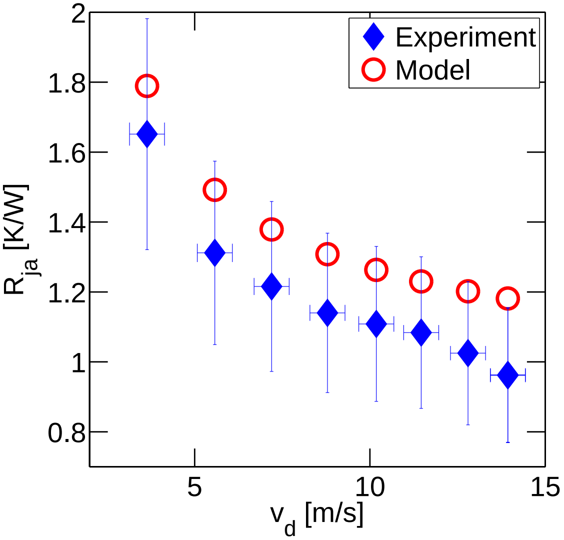

Figure 2.6: Comparison between experimental results and modeling predictions on the considered commercial heat sink. Experimental error bar values have been estimated relying on similar measurements [2–7] (See Ref. [1]).

However, the remarkable shape similarity between experimental and modeling results (Fig. 2.6), and their narrow average deviation (15.6%, Tab. 2.3) allow to consider the thermal model presented in Section 2.2 as an accurate reference for optimizing the plate fins configuration.

2.4. Optimization procedure and results

The majority of existing approaches aims optimizing heat sinks geometry to achieve the best thermal and fluid-dynamics performances at the same time [26, 42, 58], in order to fulfill the thermal dissipation requirements with minimum operating costs (i.e. fan power, which is directly linked to pressure drops). Differently, the present study focuses on optimizing the material needed to manufacture a heat sink while meeting the requested thermal performances, in order to reduce production costs. This approach is particularly effective in case of unshrouded PFHS operating in *semi-active* configurations, namely when the air flows on the heat sink thanks to an already existing fan, and thus no additional operating costs are generally involved. In particular, being unshrouded, increase of pressure props induced by heat sink lead to augmentation of bypass phenomenon. Hence, overall air circuit pressure do not increase, while thermal dissipation decreases. Here, the optimization procedure is introduced and then tested on a case study, namely the heat sink tested in Section 2.3.

First, the optimization algorithm takes as inputs the thermal conductivity of the heat sink material (λ), the maximum values of heat sink thermal resistances ($R_{ja,W}$) to be guaranteed for different approach velocities ($v_{d,W}$, i.e. the working conditions), and a first guess geometry. Then, the optimization procedure finds the heat sink geometry that: (1) guarantees $R_{ja} \leq R_{ja,W}$ for each $v_{d,W}$ (i.e. the *problem constraints*); and (2) minimize the heat sink volume, hence the production cost.

This tool considers the heat sink volume, i.e. the amount of material needed to manufacture the part, as the cost index. Consequently, it is suitable to deal with heat sinks manufactured by ”not subtractive” techniques, both traditional (e.g. extrusion, casting, stamping, folding [42]) and innovative (e.g additive manufacturing [3, 4, 7], carbon nanotube bundles [2]) ones.

Despite cost optimization generally means both production and operating costs minimization, here only production costs (i.e. heat sink volume and thus material amount) are considered for the optimization procedure. In fact, operating costs come from the power consumption of the dedicated fan, which is directly linked to the overall pressure drops of the circuit where the heat sink is placed. However, the optimization procedure suggested in this study is particularly designed for the common case of heat sinks in unshrouded *semi-active* configurations, where pressure drops induced by heat sink are usually negligible if compared with other pressure drops in the circuit, i.e. augmentation in Δp_{hs} do not lead to augmentation in overall circuit pressure drop, but lead to augmentation of bypass effect. Hence, operating costs can be considered as independent from the heat sink geometry and, consequently, the cost optimization becomes a sole production cost minimization [68].

Nevertheless, it is worth stressing that the generality of the reported procedure is not affected. In fact, the optimization strategy proposed can be easily adapted for operating costs by substituting V with $1/\eta_A$

($\eta_A = \frac{Nu/Nu_{ref}}{(f/f_{ref})^{0.33}}$ is the aerothermal efficiency [69]) as the cost indicator to be minimized. In such a way, the proposed optimization methodology finds the heat sink configuration able to minimize the overall pressure drop due to the heat sink, which determines the additional fan power consumption and thus operating costs. The latter could be relevant in case of shrouded heat sink, where bypass phenomenon do not take place.

Considering real applications, the set of possible heat sink geometries is extremely large. Hence, an algorithm able to explore the geometry parameters space in a "smart" way is needed to find the optimal solution while spending a reasonable amount of computational time. In this study, genetic algorithms are exploited to guide the problem minimum search with a more rational generation of the heat sink geometries to be evaluated.

Genetic algorithms are used to minimize an objective function (V) while respecting some problem constraints ($R_{ja} \leq R_{ja,W}$). Starting from the first guess solution given as input, the algorithm randomly generates a set of possible solutions for the problem (heat sink geometries), which is called *initial population*. For each of those possible solutions, the algorithm checks whether problem constraints are verified or not, and it evaluates the objective function. Among the solutions within the problem constraints, the algorithm chooses the ones with the smallest values of the objective function. Starting from the chosen solutions, the algorithm then generates a new population (i.e. a new set of possible solutions), relying on *crossover* and *mutation* operators. Therefore, the algorithm is designed to guide the evolution of the population toward a global, optimal solution. The population generation process is repeated until a termination condition is met, such as reaching a plateau in the objective function value or exceeding a certain number of generations.

The proposed heat sink optimization algorithm is implemented in the MATLAB™ environment. Basically, the *ga* function is here adopted to generate successive iterations of possible heat sink geometries. The thermal model defined in Section 2.2 and experimentally validated in Section 2.3 is then used to compute R_{ja} corresponding to each generated solution and working condition. Geometries with $R_{ja} > R_{ja,W}$ are then discarded, whereas the heat sink volume (V) is computed for the remaining ones. The latter is the objective function to be minimized by the genetic algorithm. Lower and upper boundary values for each geometry parameter can be specified in the genetic algorithm routine.

The heat sink characterized in Section 2.3 is then considered as a test case for the suggested optimization strategy. The actual geometry and material parameters of the heat sink by DENSO™ Thermal Systems are adopted as first guess geometry for the genetic algorithm (see Tab. 2.1). Regarding the problem constrains, it is imposed that the thermal resistances of the optimized solution (R_{ja}) must be equal or lower than the ones predicted for the commercial heat sink (i.e. $R_{ja,W} = R_{ja,model}$, as from Tab. 2.3), for each working condition considered (i.e. $v_{d,W} = v_d$, as from Tab. 2.3). The boundary values for the geometry parameter imposed in the optimization problem are reported in Tab. 2.4, being dictated by the peculiar manufacturing technique (extrusion in this case) [42].

Although genetic algorithm optimization schemes are already embedded in MATLAB™ environment by *ga* function, choosing proper settings for genetic algorithm is fundamental to achieve an optimal solution [70]. In particular, the *ga* settings adopted are: 100 generations (maximum iteration number); 100 population size (number of solutions generated by *ga* at each iteration); 95% crossover rate (ratio between *crossover* and *mutation* operators usage in generating a new population) and 10^{-14} TolFun (lower bound for the change of objective function below which optimal solution is considered to be reached).

Table 2.4: Lower (LB) and upper (UB) boundary values for geometry parameters of the PFHS (See Ref. [1]).

	L [mm]	W [mm]	t_b [mm]	H [mm]	N	t [mm]
LB	10	10	1	10	2	0.8
UB	100	100	10	80	20	2

Tab. 2.5 reports a comparison between the initial geometry of the commercial heat sink and the one obtained by the optimization procedure. Moreover, the base plate (V_b), fins (V_f) and overall (V) volumes of initial and optimized heat sinks are reported in Tab. 2.6. Results show that the optimal heat sink volume is 13.4 cm^3, that is a remarkable 64% less respect to the actual commercial heat sink volume (37.4 cm^3). Therefore, the presented optimization procedure would allow to save 24 cm^3 of material and thus reduce production costs, without affecting the overall thermal performances of the heat sink (i.e. $R_{ja} \leq R_{ja,W}$ for each $v_{d,W}$).

Table 2.5: Initial VS optimized release heat sink geometries (See Ref. [1]).

	L [mm]	W [mm]	t_b [mm]	N [mm]	H [mm]	t [mm]	b [mm]
Initial	57.2	41.4	8.4	14	21.8	1	2.1
Optimized	19.4	40.7	4.1	20	32.9	0.8	1.3

Table 2.6: Initial VS optimized release heat sink volumes (See Ref. [1]).

	V_b [cm^3]	V_f [cm^3]	V [cm^3]
Initial	19.9	17.5	37.4
Optimized	3.2	10.2	13.4

2.5. Discussion

Given the large amount of geometric, thermal and fluid-dynamics parameters strongly coupled each other, the cost-effective selection and design of heat sinks for thermal management can be often a complex procedure. In this Chapter, a comprehensive thermal model of unshrouded plate fin heat sinks including (1) flow bypass, (2) developing boundary layer along fins, (3) conduction through fins (fin efficiency), and (4) plate to fins spreading resistance, has been developed and experimentally validated. The experimental campaign has been carried out to characterize a commercially available plate fins heat sink, which is currently adopted for automotive applications (millions of units manufactured per year). Deviations between experimental results and modeling predictions allow to consider the developed thermal model as an accurate reference for optimizing the plate fins configuration.

Then, a strategy for the cost optimization of unshrouded PFHS operating in *semi-active* configurations has been proposed. Such approach is based on computationally efficient genetic algorithms and, as a test case, it has been adopted to optimize the geometry parameters of the commercial heat sink. The optimized heat sink configuration shows a remarkable 64% volume (i.e. production costs) decrease respect to the commercial one, while guaranteeing the same thermal performances.

The suggested optimization methodology has been designed for heat sinks operating in unshrouded *semi-active* configurations, where the relevant cost factor is the amount of material used to manufacture the heat sink (i.e. production cost). However, it is worth to highlight that the reported procedure is rather general, being easily transferable to operating costs (i.e. pressure drop) and to a broad variety of thermal management solutions for electronic and industrial components.

Experimental results shown in this Chapter have been collected by DENSO™ Thermal System in their laboratories. Nevertheless, a more accurate and flexible test rig is required to investigate different heat transfer enhancement techniques. Consequently, a purposely developed experimental test bench has been developed in this work. That is described in the following Chapter.

3. Experimental rig: a purposely developed heat flux sensor

In this Chapter the experimental rig used to characterize the enhanced convective heat transfer performances of surfaces and devices, proposed below in this work, is described. That allows to study a plenty of heat transfer solutions, including (but not limited to) the one investigated in Chapter. 2. Problems in neglecting conductive and radiative contributions in a convection dominated heat transfer phenomenon have been pointed out in the previous Chapter. In particular, them resulted in an underestimation of the convective heat transfer resistance experimentally measured in Chapter 2. Those difficulties have been solved in this Chapter by designing a novel convective heat flux sensor. That is conceived to exploit the notion of thermal guard. Sensor is purposely designed to measure small convective heat flows (<0.2 W/cm^2) from micro-structured surfaces and small heat exchangers, that would have been hard to be characterized with enough accuracy by mean of the experimental rig introduced in Chapter 2. It deals with metal samples, e.g. by DMLS. Sensor design and validation are described in details. For validation purposes, both experimental literature data and a computational fluid dynamic (CFD) model are used. Maximum and average deviations from CDF model in terms of the Nusselt number are on the order of ±13.7% and ±6.3%, respectively while deviations from literature data are even smaller. Contents of this Chapter can be also found in [4].

3.1. Motivations

Measuring the convective heat transfer coefficient locally (i.e. on small ares on the order of 1 cm^2) usually presents difficulties; The reason (among others) is that such a quantity depends on both the flow regime and the fluid properties. Moreover, even though one assumes that the velocity boundary layer is fully developed (which might not be the case for jets impinging on surfaces), still the local convective heat transfer coefficient strongly depends on the development of the thermal boundary layer. The latter remark is particularly relevant to electronics cooling, due to small dimensions of hot spots. In fact, experiments on flush mounted heat sinks [71–73] clearly show that the local convective heat transfer coefficient is affected by the chip location on the electronic board. In particular, Authors in Ref. [71] found that the average convective heat transfer for the rows of heating arrays decreases approximately 25% from the first to the second row and by less than 5% from the third to the fourth row. Ref. [72] reports that, in steady state conditions, heat transfer coefficient is strongly affected by the number of chips and their locations in the streamwise flow direction. The latter results have been proved also in transient conditions [73]. The peak in the convective heat transfer coefficient at the edge of the heating surface is due to the small thickness of the thermal boundary layer in the early development region. Small thickness of the thermal boundary layer makes the developing region ideal to investigate the heat transfer enhancement due to micro-structures (e.g. process roughness, protruded patterns). For this reason, in the present Chapter, a single flush-mounted heat source such as the one considered in [8] is considered.

Classical methods for measuring the local heat flow can be divided in three main categories: Methods based on thermography, on sensible capacitors and on diffusion meters [38]. During the past several years, infrared thermography has evolved into powerful tool to measure convective heat fluxes as well as to investigate the surface flow field over complicated bodies [74]. In spite of the advantages of the latter technique, e.g. the modest intrusiveness [75], infrared thermography suffers from some drawbacks. First of all, the measurement accuracy depends on the knowledge of the emissivity coefficient of the surface exposed to the infrared camera [74]. This effect is more susceptible to highly polished surfaces: In fact, due to low emissivity coefficient and high reflectivity of the surface one has to cope with a low signal-to-noise ratio [74]. Moreover, surface structuring/patterning might create problems in estimating non-homogeneous emissivity. In case of high density applications, there might also be a problem in positioning the access window to the test surface for the infrared camera [74]. Finally, when measuring the local convective heat transfer coefficient over a fin, the temperature value identified at each image pixel by the infrared camera must be post-processed by a numerical model in order to estimate the desired quantity [76, 77]. Hence, it is an indirect measurement technique, which might be further affected by the uncertainties of the underlaying numerical model.

Measurements by sensible capacitors require that heat flow is used to transfer energy to a capacitor, where energy is stored in the form of sensible heat [38]. The heat flux is then measured by the time evolution of the temperature. Large thermal inertia is required, so that the time for thermal equilibrium is long and easily measurable. It is important that the temperature within the device is as uniform as possible and the volume/surface area ratio of the capacitor very small. Some disadvantages of sensible capacitors include inaccuracy in obtaining the time evolution of the temperature, the need to cool down the device to a temperature lower than the temperature where the heat flow is to be measured before measurements can be taken and the intrusiveness of the device [38].

On the other hand, diffusion meters are based on the Fourier's law of heat conduction at steady state [38]. Here, it is necessary that the heat flow within the device stays unidirectional. Consequently, some proper insulation must be ensured and the heat flux can be measured by a series of thermocouples installed along the main heat flow direction. Some disadvantages of diffusion meters include difficulties in maintaining the heat flow direction, the need for truly insulating layers around the measuring elements and the need for a steady-state measurement [38]. In addition, establishing an (easily) measurable temperature gradient in a highly conductive material requires large thermal fluxes. In case of forced air convection, thermal fluxes may be quite small (e.g. $< 0.2\ W/cm^2$) and this introduces significant difficulties in measuring a temperature gradient within a copper bar as in Ref. [8], where thermal fluxes larger than 5 W/cm^2 are indeed considered. Moreover, in case of small thermal fluxes, the relative magnitude of the conduction losses increases and it makes less accurate the measurement by a diffusive meter. It is worth to note that the conduction losses are, in general, non-linear. In fact, some thermal power is inevitably lost and reaches the air stream passing through the sensor holder. More dramatically, the amount of surface area which is crossed by conduction losses, is affected in turn by convection, thus making the thermal resistance due to conduction losses flow dependent. In this research activity, the latter issue was experienced during the development of a previous release of the presented sensor (not reported), and it was successfully solved by introducing the thermal guard. More details about the latter issue are provided below in Section 3.2.

Another type of sensor that has recently gained great popularity are flush mounted sensors [78] [79], which are commonly used in heat transfer characterization of flat surfaces. However for micro-structured surfaces a reliable measure of the convective heat transfer coefficient is difficult to obtain with those sensors. In fact, if the latter sensors are mounted on micro-structured surfaces, then the fluid-dynamics interactions between micro-structures and fluid flow are (at least locally) perturbed. This implies that heat transfer is altered by the presence of the sensor and hence the measurement is not reliable. On the other hand, positioning such sensors at the bottom of samples is not always an accurate solution, owing to an unavoidable change of the heat flux direction. Although one might think that the adoption of insulating materials (surrounding the sample facets that are not exposed to the fluid) represents an effective solution, that this may lead to non-negligible deviations in the heat flux estimates as demonstrated in Section 3.2. In addition, the issue of undesired heat losses in such convective heat transfer measurements becomes even more serious when small fluxes are to be measured, thus making questionable the use of those sensors in the context of micro-electromechanical systems (MEMS), which is an active research area gaining and increasing popularity (see e.g. [79, 80]).

Motivated by all this, a sensor that is able to tackle the above drawbacks by resorting to the notion of thermal guard has been designed and validated (against both experimental data from literature and a computational fluid dynamic model). As a result, a few advantages of the proposed device are summarized in the following:

1. The sensor does not perturb the fluid-dynamic interactions between micro-structures and fluid flow.

2. The uncertainties due to (spreading) conduction losses can be effectively made negligible by adopting the thermal guard, which keeps the temperature within the device very uniform.

3. The experimental procedure is remarkably simple, because it only requires the measurement of an electrical power and three temperatures. No numerical model is required to post-process each time the measured quantities, leading to a direct measurement technique.

4. The sensor design can be miniaturized, making it an ideal candidate for studies with small heat fluxes (e.g. forced air convection and MEMS applications).

5. Unlike state-of-the-art flush mounted foil sensors, which are often limited in terms of the operating temperature due to delamination issues (i.e. 120-150 C°, see [81]), the present sensor can be easily designed to withstand high temperatures by a proper choice of materials.

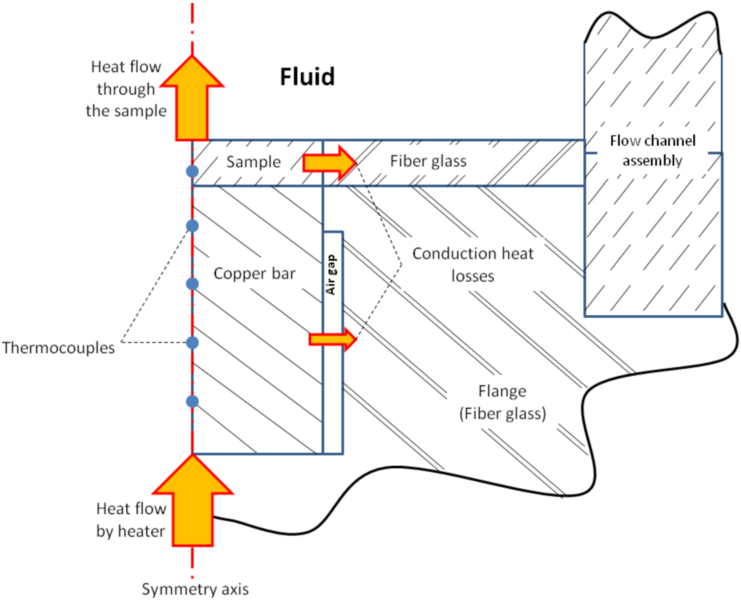

Figure 3.1: Example of a heat flow sensor as used in [8] (see Ref. [4]).

The Chapter is organized as follow. The main traditional approaches for convective heat transfer measurements are reviewed in Section 3.1. In Section 3.2, the issue of spreading conduction losses when addressing the measurement of small heat fluxes by traditional devices is discussed. The key-idea behind the proposed sensor is presented in Section 3.3.1, whereas details about the sensor design are provided in Sections 3.3.2 and 3.3.3. In Section 3.4, the equipment and the procedure adopted in the validation process are discussed. In Section 3.5, the experimental results are presented and a comparison with both independent experimental data from literature and the results of a fluid-dynamic model (whose details are discussed in the Appendix A) are reported. In Section 3.6, results are discussed.

3.2. Limitation of traditional diffusion meters

In the following, referring to the diffusion meter utilized in [8], will be highlighted possible issues arising when measuring small heat fluxes, as those experienced with low thermal conductive fluids (e.g. air) and/or small heat exchange surface areas (e.g. small chips and/or MEMS devices). The device proposed in [8] is schematically reported in Fig. 3.1 and, similarly to the sensor proposed below in this work, utilizes a copper sample (with slightly different dimensions, namely $12.7 \times 12.7 \times 5.51\ mm^3$) upon which the convective heat transfer coefficient is to be measured. The latter sample is flush mounted on one side of a flow channel, and surrounded by low thermal conductive G-10 fiberglass epoxy, for reducing conduction heat losses. Heat is generated by a cartridge heater positioned at the bottom of the bar and reaches the sample through a copper bar. The bar is embedded in a G-10 fiberglass flange. While an air gap is present along most of the bar length (roughly 30 mm), the remaining part of the bar (comparable to the sample thickness) is in direct thermal contact with the G-10 fiberglass epoxy. The temperature gradient (hence the heat flux) through the copper bar can be measured by means of four thermocouples located along the centerline of the copper bar. A linear trend of the temperature profile along the bar is demonstrated, hence the local heat flux at the copper bar axis can be accurately estimated by Fourier's law. Strictly speaking, owing to unavoidable conduction heat losses, the above heat flux is only accurate along the symmetry axis in Fig. 3.1. On the other hand, if the aim of the study is measuring the heat flux from the entire sample surface, the average heat flux is the quantity of interest. For instance, this is certainly true in electronics cooling, where the total dissipated heat from a chip surface is often the only concern. In those cases, the measurement accuracy of diffusion meters fully relies upon the possibility of neglecting the conduction heat losses (as compared to the heat flux exiting the sample surface exposed to the fluid flow) and on the assumption that the average heat flux can be safely approximated by the value measured at the centerline. Whenever the above approximation does not hold, the use of correlations such as the one proposed in [8] (and derived from measurement along the copper bar centerline) clearly leads to overestimates of the average convective heat transfer. Towards an effort of quantifying the effect of the conduction heat losses in the experiments reported in [8], the following analytical formula expressing the conduction heat from a hot vertical cylinder (copper sample attached to the bar) embedded within a semi-infinite medium (air gap and G-10 fiberglass epoxy) is invoked (see

Ref. [38] p. 224):

$$q_{loss} = \frac{2\pi l}{ln\left(4l/d\right)}\lambda_{fg}\left(T_s - T_a\right), \tag{3.1}$$

where l, d and λ_{fg} denote the cylinder length, the cylinder diameter and the thermal conductivity of the fiberglass flange, respectively. The average convective heat transfer coefficient h over the sample surface can be cast into the form:

$$h = \frac{h_c L^2\left(T_s - T_a\right) - q_{loss}}{L^2\left(T_s - T_a\right)}, \tag{3.2}$$

where h_c is the convective heat transfer coefficient at the centerline (consistently with the one measured in [8]). In the ideal case of $q_{loss} = 0$, it follows $h = h_c$. Owing to (3.1), the equation (3.2) reduces to the explicit expression:

$$h = h_c - \frac{2\pi l}{L^2 ln\left(4l/d\right)}\lambda_{fg} \tag{3.3}$$

By referring to Fig. 3.1, the cylinder presents a square cross-section and two different media are surrounding its mantel. To first approximation, even with a conservative assumption of neglecting the heat loss through the cylinder mantel facing the air gap, it results $l \approx l_{fg} \approx 11\ mm$ with l_{fg} being the cylinder length in direct contact with the fiber glass. Finally, considering G-10 garolite [82] with $\lambda_{fg} = 0.27\ Wm^{-1}K^{-1}$ and an effective cylinder diameter $d = 14.3\ mm$ (chosen to preserve the heat transfer surface area by $L^2 = \pi d^2/4$), it yields the following estimate:

$$h \approx h_c - \Delta h, \tag{3.4}$$

with $\Delta h = 103\ Wm^{-2}K^{-1}$. In [8] an empirical correlation is provided for samples with a smooth surface:

$$Nu_L^c = 0.237 Re^{0.608} Pr^{1/3}, \tag{3.5}$$

where the superscript in the Nusselt number Nu_L^c is used to stress that this quantity is based on measurements of h_c: $Nu_L^c = h_c L/\lambda_{fluid}$. In particular, because an inert flourocarbon liquid (FC-72) is used in the work of Maddox & Mudawar, the correction term Δh in equation (3.4) can be translated in terms of a corresponding Nusselt number as follows:

$$\Delta Nu_L = \frac{\Delta h L}{\lambda_{fluid}} \approx \frac{103[Wm^{-2}K^{-1}]\ 0.0127[m]}{0.057[Wm^{-1}K^{-1}]} = 22.9, \tag{3.6}$$

and consequently the following dimensionless group:

$$\frac{\Delta Nu_L}{Pr^{1/3}} = \frac{40.1}{12.3^{1/3}} = 9.9, \tag{3.7}$$

where the Prandtl number is assumed to be $Pr = 12.3$ (see also Fig. 6 in Ref. [8]). As a result, if the average heat transfer coefficient h is of interest (instead of h_c), the correlation (3.5) should be expressed as follows:

$$\frac{Nu_L + \Delta Nu_L}{Pr^{1/3}} = 0.237 Re^{0.608}, \tag{3.8}$$

where $Nu_L = hL/\lambda_{fluid}$ and $Nu_L^c = Nu_L + \Delta Nu_L$. It is worth stressing that the above analysis aims at providing only an estimate of the conduction heat losses for the set-up in Fig. 3.1. Hence, for the sake of simplicity, the contact thermal resistance between the cylinder and the surrounding medium has been neglected to first approximation. As a consequence, (3.7) is expected to slightly overestimate the group $\Delta Nu_L/Pr^{1/3}$. However, judging from (3.7), in the low Reynolds numbers regime (e.g. $Re \approx 3000$) and for the analyzed configuration, the influence of the correction term ΔNu_L can be on the order of 0.35 Nu_L^c. Hence, as long as the average convective heat transfer coefficient is of interest, there are certainly conditions where conduction losses cannot be neglected and should be properly taken into account during the measurement process. The above argument also shows that, due to difficulties in evaluating the correction term (3.7) with a desired accuracy (e.g. owing to possible unpredictable thermal contact resistances), the use of diffusion meters (or other sensors suffering from conduction heat losses) in such a context may become quite problematic.

For the sake of completeness, a computational fluid dynamic (CFD) model has been developed to compute the average convective heat transfer coefficient through a square shaped sample (consistently with the set-up of interest for this study). Details of the model are reported in the Appendix A. Most importantly, it is worth to note that the latter numerical model is found to be in good accordance with the empirical correlation proposed by [8], and here re-formulated in terms of the Nusselt number based on the average convective heat transfer coefficient following Eq.(3.8). The comparison in reported in Fig. 3.2, where the adoption of a linear vertical scale (instead of the usual logarithmic one) makes the matching even more appreciable. Hence, as long as smooth samples are concerned, both an experimental correlation (3.8) and numerical results from CFD are available for validating the proposed sensor.

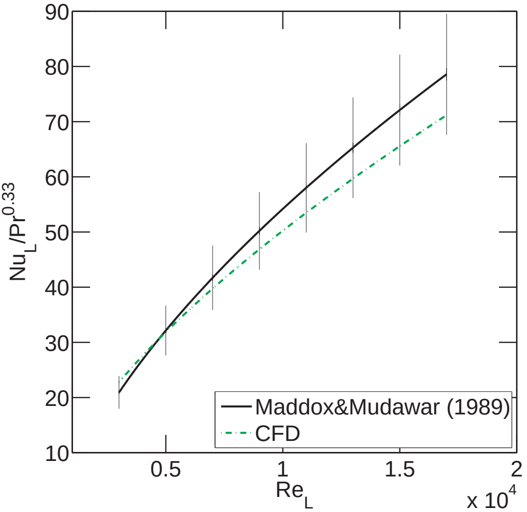

Figure 3.2: Maddox&Mudawar experimental correlation [8] re-formulated in terms of Nusselt number based on the average convective heat transfer coefficient according to the Eq. (3.8) (solid line) vs the CFD results (dot-dashed). Error bars with amplitude ± 13.9 % are shown as vertical bars for the Maddox&Mudawar experimental correlation (see Ref. [4]).

It is also worth to stress that, although the above discussion focused on conduction heat losses in a diffusion meter, a similar analysis also applies to devices where a flush mounted foil sensor is adopted for instance between the bar and the sample. In fact, reducing at will the heat losses through the finite thickness of the sample (e.g. by means of insulating materials) is not a trivial task, especially when the fluid thermal conductivity is comparable to (or even smaller than) the adopted insulating material.

As a result, in this work, a new sensor for the direct and accurate measurement of the average convective heat transfer coefficient over small surfaces has been designed. In the presented implementation, the sensor is conceived for dealing with forced air cooling a sample surface (roughly 1 cm^2), and details are reported in the sections below.

In principle, there are no limitations to a further miniaturization of the sensor. As mentioned in Ref. [79], such a feature is highly desirable and still represents a challenge for state-of-the-art flush mounted foil sensors.

3.3. Design of a new sensor

3.3.1. The key idea

The key-idea is to exploit the notion of thermal guard for local convective heat transfer measurements. Guarded hot plate method has been extensively used in measuring thermal conductivity. When attaching two thermostats at different temperatures to the opposite faces of the sample, heat flows from the hot to cold side typically following three-dimensional paths. However, a one-dimensional flow can be established within a sample by surrounding it with temperature-controlled "guards" designed to prevent the heat flow in all directions other than the desired one [83].

The ability of the guard to prevent undesired heat flows can be conveniently used for measuring convective heat transfer coefficients as well. Sensors based on this concept may be so accurate that can be used even for calibration purposes. For instance, the US National Institute of Standards and Technology (NIST) has developed a convective heat flux facility to allow calibration of heat flux sensors based on a guarded calibration plate ($30\,cm \times 10\,cm \times 3\,cm$) [84].

In this work, a similar idea is developed at a smaller scale, and used beyond calibration purposes for developing a simple though accurate sensor. An isometric view of the proposed sensor is reported in Fig. 3.3. The proposed sensor is made of three essential parts: (i) sample, (ii) insulation shield and (iii) guard. A heater is placed at the bottom of the sample and the latter is made of highly conductive material, because it has to efficiently transfer heat towards the flushing flow. The sensor presents an onion-like structure: Insulation shield wraps the sample, while a highly conductive guard wraps the assembly consisting of both the sample and the insulation shield. The insulation shield and the guard are shaped such that the guard sharply joins the sample, and the sensor surface exposed to the air flow appears as a unique element. As a result, two independent thermal circuits are obtained, where the sample heater generates the thermal power to be removed by the tested surface, while an auxiliary heater supplies thermal energy to the guard until isothermal condition is reached (i.e. negligible heat transfer between the guard and the sample).

3.3.2. Mechanical design

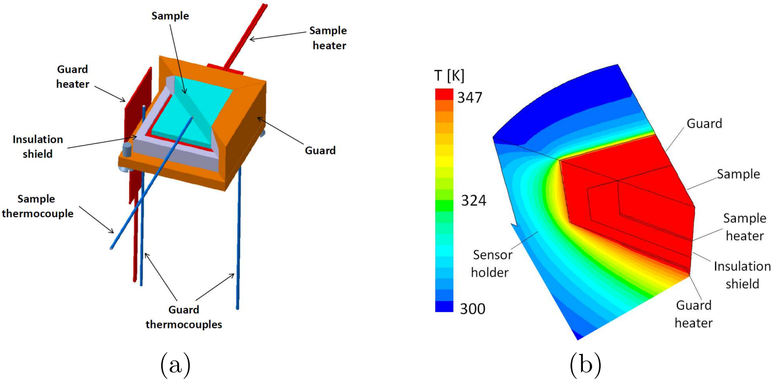

Figure 3.3: Isometric view of the proposed sensor is shown in (a). The design process has been assisted by a three-dimensional numerical model solving the energy balance equation, depicted in (b). This model is particularly useful to compute the sample-to-guard coupling transmittance k. To this purpose, the guard heater location does not play a crucial role (k mainly depends on the sensor geometry), and particularly in the model the heater is placed at the bottom of the guard, while in the isometric view it is displayed laterally (see Ref. [4]).

Fig. 3.3 shows the sample (in this realization, a box of $11.1\,mm \times 11.1\,mm \times 5\,mm$), which is heated at the bottom and cooled from above by air flushing in a wind tunnel. The top surface of the sample can be possibly patterned in order to investigate different techniques for heat transfer enhancement. The sensor sample is heated by an electrical heater (a $12.7\,mm \times 12.7\,mm$ Minco heater with a nominal resistance of $26.5\ \Omega$). Thermal grease, with conductivity $2.9\ W/m/K$, was used for reducing thermal resistances at all contact surfaces of the device, when appropriate. The sample is surrounded by an insulation shield made of Teflon. This element consists of a $16\,mm \times 16\,mm \times 3\ mm$ plate at the bottom and a $2.4\ mm$-thick square-shaped tapered ring with negligible thickness at the test surface. Finally, the sample and shield assembly is embedded within the thermal guard which comprises a square-shaped complement of the insulation shield on top of a flat plate. The latter two elements are made of copper and their mechanical and thermal contact is ensured by two watch screws (M1.6). The upper part of the guard is built by electrical discharge machining (EDM) in order to have sharp edges leading to minimal sample/guard contact (important for having two independent thermal circuits). The guard heater (same electrical resistance by Minco is used) is positioned upstream for (partially) compensating the higher convective heat transfer coefficient due to the development of the thermal boundary layer (induced by the guard). The sensor assembly is held by an insulator holder made of nylon, which is fixed to the wind tunnel (discussed below).

Three temperatures are measured by means of Chromel-Alumel (type K) thermocouples with probe sheath diameter of 0.5 mm. A first thermocouple crosses all layers and reaches the center of the sensor sample. The remaining two thermocouples are inserted in the upstream and downstream wall, respectively. Although the development of the thermal boundary layer might lead to small temperature differences streamwise, having three thermocouples in a row aligned along the fluid flow is twofold advantageous. First, this enables to check that only a minimal temperature differences is established between two sufficiently far locations of the guard (in this setup, on the order of 0.2 K). Second, imposing that the sample temperature T_s is the arithmetic mean of the two temperature values in the guard, namely $T_s = (T_{g1} + T_{g2})/2$, enables to minimize the net heat exchange between sample and guard due to possible balance mismatches.

3.3.3. Computational support to design

The design process has been assisted by numerical computations. In particular, a three-dimensional numerical model has been developed and solved by Fluent™. A simplified non-coupled model solves the stationary energy balance equation within the sensor assembly, assuming a fixed convective heat transfer coefficient.

Let us suppose to use copper (thermal conductivity 388 $W/m/K$) for both the sample and the guard, Teflon™ (0.25 $W/m/K$) for the insulation shield and nylon (0.25 $W/m/K$) for the external sensor holder. This model includes the convective heat transfer as a boundary condition on the surface in contact with the flushing flow. A fixed convective heat transfer coefficient is assumed for both the sample and the guard, namely 70

$W/m^2/K$. The back side of the sensor is subject to a different boundary condition due to natural convection with a coefficient of 10 $W/m^2/K$.

In the model, the thermal power of the sample heater and the one of the guard heater can be independently controlled. Let us suppose to provide 0.05 W to the sample heater. The balance condition will be defined by matching the sample temperature T_s, measured at the sample center, and the guard temperature T_g, measured in the guard lateral wall, up to a certain precision. Let us suppose that $T_s - T_g = 0.2\,K$ and consequently that part of the power provided by the sample heater flows towards the guard. The numerical model can be used to evaluate the power lost towards the guard. In this set-up, it was found to be 0.002 W), corresponding to 4 % of the sample heater power. Hence, by linear extrapolation, the conduction losses towards the guard can be expressed as $k\,(T_s - T_g)$ where $k = 0.01$ W/K.

It is worth stressing that the transmittance k depends on the sensor geometry, hence it is only required to be computed once for ever (for a given sensor design).

3.4. Experimental rig description

3.4.1. Experimental equipment

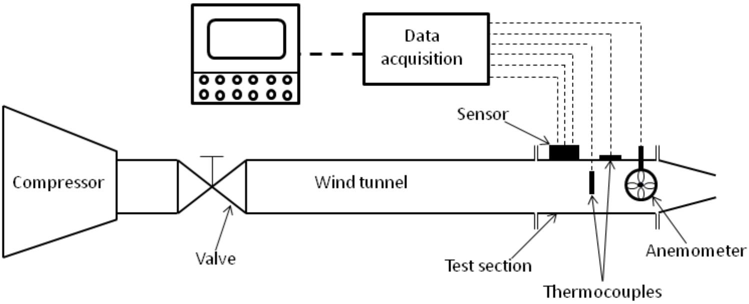

Figure 3.4: Schematic diagram of the experimental facility (see Ref. [4]).

The flow loop of the experimental system is schematically shown in Fig. 3.4. The developed sensor is installed at the center of the vertical wall of a horizontal rectangular flow channel, which resembles a small open-loop wind tunnel. The channel has a smooth inner surface, a cross section of $228\,mm \times 158\ mm$ (hydraulic diameter $187\ mm$) and an entrance length of $5\,m$ (corresponding roughly to 26 hydraulic diameters). The air is blown by a Savio s.r.l. centrifugal fan type SFL 25-A (maximum flow rate 70 m^3/min at 420 Pa, maximum pressure difference 1900 Pa at 18 m^3/min), with a throttling valve for regulating the mass flow rate. At the end of the channel, downstream from the test section, a vane anemometer Testo 450 by Testo AG (sensitivity $\pm 0.1\ m/s$) was used for measuring the axial velocity. The air temperature is measured at the same location where the anemometer is installed (not affected by the power released by the convective sensor). The thermocouple probe sheath is embedded in a block of polystyrene foam, covered by an aluminum foil, ensuring stable measurements and negligible effects due to radiation. Similarly, the channel wall temperature is measured by a thermocouple installed on the inner surface of the channel, covered by a block of polystyrene foam with an external aluminum foil. Also in this case, Chromel-Alumel (type K) thermocouples were used. Two HQ PS3003 variable power suppliers (voltage range $0-30\ V$ and $0-3\ A$) are used to feed both the sample and the guard heater. Finally, a six-digits, electronic multimeter (Agilent 34401A) is used to measure the voltage to the sample heater circuit, made of the heater itself and the wires to connect the heater to the power supplier.

3.4.2. Experimental procedure

The axial velocity v_{ax}, measured by the vane anemometer, is used to compute the Reynolds number $\mathrm{Re}_D^x = v_{ax}\, D/\nu$ where D is the hydraulic diameter of the channel. However, it is worth to note that the experimental data are usually reported in terms of a differently defined Reynolds number $\mathrm{Re}_D = v_{av}\, D/\nu$, which depends on the average velocity v_{av} instead. These two velocities have been correlated by a purposely-developed fluid-dynamic numerical model, which was solved by Fluent™ and described in the Appendix A. The previous numerical model was used to construct the following relation, $\mathrm{Re}_D = 0.694\ \left(\mathrm{Re}_D^x\right)^{1.0162}$, which correlates the average velocity to the axial velocity (measured by the vane anemometer) through the corresponding Reynolds numbers.

For computing the average convective heat transfer coefficient at the sample surface, the following relation is used

$$h = \frac{V_h^2/R_h - \sigma_B \epsilon A(T_s^4 - T_w^4) - k[T_s - (T_{g1} + T_{g2})/2]}{A(T_s - T_a)}, \tag{3.9}$$

where V_h is the potential difference across the sample resistance, R_h is the sample resistance, $\sigma_B = 5.67 \times 10^{-8}\ W/m^2/K^4$ is the Stefan-Boltzmann constant, ϵ is the emissivity of the sample surface, T_s is the sample temperature measured by the thermocouple inserted in the center of the sample, T_w is the temperature of the channel wall, $k = 0.01\ W/K$ is the sample-to-guard coupling transmittance (see Section 3.3.3), T_{g1} and T_{g2} are the temperatures measured by the (upstream and downstream) thermocouples installed into the thermal guard, $A = 1.23\ cm^2$ is the flat sample surface and, finally, T_a is the air temperature. V_h is calculated by the following equation:

$$V_h = V \frac{R_h}{R_h + R_{wire}}, \tag{3.10}$$

where V is the voltage applied to the sample heater circuit, measured by the multimeter for each test, while R_{wire} is the resistance of heater wires, which measures 0.015 Ω. Before proceeding with the experimental results, a discussion about the estimate of uncertainties and their propagation by the proposed measurement chain is required. Eqs. (3.9) and (3.10) allow to compute h as a function of other measurements $(V, T_s, T_{g1}, T_{g2}, T_a, T_w)$ and parameters $(R_h, R_{wire}, \epsilon)$, namely:

$$h = h(V, T_s, T_{g1}, T_{g2}, T_a, T_w; R_h, R_{wire}, \epsilon). \tag{3.11}$$

These independent quantities can be organized in a vector, namely:

$$\mathbf{q} = \{V, T_s, T_{g1}, T_{g2}, T_a, T_w; R_h, R_{wire}, \epsilon\}, \tag{3.12}$$

where $q_i \in \mathbf{q}$ denotes the generic i-th quantity. The type B standard uncertainty (coverage factor: 2) of the quantity h, namely $\Sigma_{h,B}$, can be computed by the following uncertainty estimation method [85]:

$$\Sigma_{h,B} = \frac{1}{h} \sqrt{\sum_{i=1}^{9} \left(\Sigma_{q_i} \frac{\partial h}{\partial q_i} \right)^2}, \tag{3.13}$$

where Σ_{q_i} is the standard uncertainty for the quantity q_i. Instead of assuming the nominal value of R_h (namely 26.5 Ω), the value of the sample resistance has been measured as function of the sample temperature (thermal drift), in order to obtain the functional dependence $R_h = f(T_s)$. Hence Eqs. (3.9) and (3.10) are based on the measured potential difference only. The standard uncertainty of the voltage measured by the multimeter can be assumed Σ_V=0.0016 V. The temperatures T_s, T_{g1} and T_{g2} are critical and, therefore, thermocouples calibrated by thermostatic bath were used. The corresponding uncertainties can be assumed $\Sigma_{T_s} = \Sigma_{T_{g1}} = \Sigma_{T_{g2}} = 0.05\ K$. On the other hand, other thermocouples might be characterized by $\Sigma_{T_a} = \Sigma_{T_w} = 0.4\ K$, because of the intrinsic uncertainties of the installation setup. $\Sigma_{R_h} = \Sigma_{R_{wire}} = 0.014\Omega$ has been chosen. Anemometer calibration has been performed and corresponding uncertainty has been calculated. The latter depends on measured velocity according to a polynomial function. Minimum and maximum calculated values of uncertainty $\Sigma_{v_{ax}}$ are 0.1 m/s and 0.38 m/s respectively.

The estimate of the sample surface emissivity ϵ requires more care, and the following procedure is adopted. The sample temperature was measured first by the calibrated thermocouple. Next, the surface emissivity was tuned by a thermal camera (NEC TH9100 Series Infrared Thermal Imaging Camera), in order to match the latter (independently) measured temperature. This procedure provided $\epsilon = 0.23$ and 0.1 for copper and aluminum alloy AlSi10Mg, respectively (below the reason for characterizing also AlSi10Mg is clarified). A quite large value of uncertainty has been assumed, i.e. $\Sigma_\epsilon = 0.1$, owing to the poor quality of the infrared image. In table 3.1, uncertainties of measured quantities and sensitivities of measurement devices used in this work are reported.

Using the above values of standard uncertainties Σ_{q_i}, type B uncertainty $\Sigma_{h,B}$ has been calculated through Eq. (3.13); Consequently, the type B relative standard uncertainty $\sigma_{h,B}$ has been calculated by $\sigma_{h,B} = \Sigma_{h,B}/h_F$, where h_F is a power-law least squares fitting of the experimental data for each sample. In particular, $h_F = h_F(v_{av}) = d_1\, {v_{av}}^{d_2}$, where d_1 and d_2 are proper fitting parameters.

On the other hand, a novel method has been proposed here for calculating type A uncertainties. This method aims to take advantage of measurements performed at different velocities to properly calculate tolerance intervals [4]. Given a set of n measurements of convective heat transfer coefficients h_i, performed at different velocities v_i, the latter have been normalized with regards to the corresponding power-law fitting, namely

Table 3.1: measured quantities uncertainties and measurement devices sensitivities (see Ref. [4]).

Measured quantity	Σ_{qi}	Device	Sensitivity
V	0.0016 V	Multimeter	0.00001 V
T_s	0.05 K	Thermocouple	0.041 mV/K
T_{g1}	0.05 K	Thermocouple	0.041 mV/K
T_{g2}	0.05 K	Thermocouple	0.041 mV/K
T_a	0.4 K	Thermocouple	0.041 mV/K
T_w	0.4 K	Thermocouple	0.041 mV/K
R_h	0.014 Ω	Multimeter	0.0001 Ω
R_{wire}	0.014 Ω	Multimeter	0.0001 Ω
ϵ	0.1	Thermal camera	0.08 K
v_{ax}	0.1–0.38 m/s	Vane anemometer	0.1 m/s

$h'_i = h_i/h_F(v_i)$. Consequently, a new set composed by n elements h'_i, distributed according a Gaussian function, has been obtained. Hence, the mean value μ' and the standard deviation σ' of the latter set can be computed. Finally, the population mean μ and the maximum population standard deviation σ of the set can be calculated by the Student's t-distribution and the Chi-squared distribution, respectively. In particular, $\mu = \mu' \pm \sigma_\mu$, where $\sigma_\mu = t_{1-\alpha/2,\,n-1}\,\sigma'/\sqrt{n}$ and $\sigma = \sigma'/\chi_{\alpha/2}\,\sqrt{n-1}$ [85]. Combining the previous standard deviations, namely $\sigma_{h,A} = \sqrt{\sigma_\mu^2 + \sigma^2}$, it results

$$\sigma_{h,A} = \sigma' \sqrt{\frac{t^2_{1-\alpha/2,\,n-1}}{n} + \frac{n-1}{\chi^2_{\alpha/2}}}. \tag{3.14}$$

Finally, the overall relative standard uncertainty can be obtained as

$$\sigma_h = \sqrt{\sigma^2_{h,A} + \sigma^2_{h,B}}. \tag{3.15}$$

It is worth to highlight that the previous procedure allows one to compute tolerance intervals, which are wider than confidence intervals, and more robustly estimate the experimental uncertainty. Anticipating the experimental results described in Section 3.5, the maximum and mean relative uncertainty for the convective heat transfer coefficient is ±9.9% and ±6.7%, respectively. Moreover, in these experiments, A-type uncertainty is wider than B-type uncertainty (the latter being ±2%), proving that the overall accuracy of the measurement procedure is satisfactory.

Values of type A uncertainties depend on the number of experimental tests n (See Eq. 3.14). In particular, they are supposed to decrease as n increases (See Ref. [4]). Finally, a comprehensive statistical analysis of experimental data must include a procedure able to detect outliers in the data sets. In this study Grubb's test has been used to identify outliers among extreme data. For these particular data sets no outliers have been found, hence no data have been canceled out. The latter result proves good repeatability of the proposed sensor and experimental rig.

3.5. Experimental rig validation

In this section, experimental results are reported in order to validate the proposed sensor and experimental rig. In particular, 15 and 13 experimental points were investigated for aluminum alloy AlSi10Mg and copper samples smooth surfaces respectively, by varying the axial velocity in the range $3.1 - 15.5\ m/s$. A sample made of AlSi10Mg has been tested in order to make sure that the proposed sensor can properly function with samples made of a different material compared to the guard. In particular, AlSi10Mg has a thermal conductivity of $150\ W/m/K$, which is roughly one-third compared to copper, and is often used in DLMS application [3]. Experimental points are reported in Tables 3.2 and 3.3. The sample heater thermal power in the proposed experiments is roughly $0.126\ W$ (corresponding to power densities of $0.102\ W/cm^2$). The power densities are quite small (due to air), which make accurate measurement pretty challenging. For each test, the thermal power supplied to the guard is adjusted in order to satisfy the following condition at steady state: $T_s = (T_{g1} + T_{g2})/2$. During tests, the thermal balance was found to be well satisfied: For the upstream part of the guard, the average temperature difference $T_{g1} - T_s$ is $0.19\,K$ (maximum $0.40\ K$) while, for the downstream part, the average temperature difference $T_s - T_{g2}$ is $0.23\ K$ (maximum $0.40\ K$).

Experimental data are reported in Fig. 3.5, where they are compared to both an experimental correlation from literature [8] (with conduction losses properly taken into account by Eq. (3.8)) and numerical results from CFD model (see the Appendix A for details). As visible in Fig. 3.5, the accordance of experimental results with the two chosen benchmarks is

Table 3.2: Experimental data about convective heat transfer for AlSi10Mg sample (see Ref. [4]).

v $[\frac{m}{s}]$	Re_L $[-]$	T_s [°C]	T_a [°C]	$\frac{V_h^2}{R_h}$ $[W]$	h $[\frac{W}{m^2K}]$	$\frac{Nu_L}{Pr^{1/3}}$ $[-]$	σ_h [%]
3.3	3493	61.9	29.2	0.1271	30.80	26.47	6.55
4.2	4528	57.9	29.1	0.1271	35.10	30.17	5.97
5.2	5585	54.0	29.0	0.1270	40.58	34.88	5.48
6.2	6659	51.1	29.3	0.1270	46.75	40.17	5.14
7.2	7747	48.0	28.7	0.1270	52.67	45.27	4.88
8.2	8843	46.7	28.2	0.1270	54.95	47.23	4.79
9.2	9944	45.0	27.5	0.1269	58.08	49.91	4.69
9.2	9944	44.0	27.3	0.1275	60.96	52.39	4.65
10.3	11159	43.2	27.3	0.1274	64.24	55.21	4.59
10.3	11159	43.4	27.7	0.1273	65.00	55.86	4.58
11.3	12263	42.2	27.3	0.1274	68.85	59.17	4.52
12.2	13256	41.1	27.3	0.1273	74.19	63.76	4.46
13.2	14357	40.1	27.2	0.1273	79.07	67.96	4.42
14.2	15454	39.4	27.3	0.1273	84.75	72.83	4.38
15.1	16549	38.9	27.3	0.1274	88.97	76.47	4.36

Table 3.3: Experimental data about convective heat transfer for copper sample (see Ref. [4]).

v $[\frac{m}{s}]$	Re_L $[-]$	T_s [°C]	T_a [°C]	$\frac{V_h^2}{R_h}$ $[W]$	h $[\frac{W}{m^2K}]$	$\frac{Nu_L}{Pr^{1/3}}$ $[-]$	σ_h $[\%]$
3.1	3289	62.0	29.2	0.1248	28.74	24.70	8.42
3.3	3493	62.7	29.1	0.1259	28.23	24.26	8.50
3.8	4111	58.0	29.3	0.1241	33.63	28.90	8.32
4.8	5160	52.0	27.4	0.1253	38.94	33.47	8.63
6.3	6768	48.5	27.9	0.1254	47.48	40.80	9.33
8.8	9503	42.5	27.2	0.1261	64.70	55.61	8.55
8.8	9503	44.5	28.6	0.1253	62.16	53.42	8.79
10.1	10938	42.6	27.5	0.1244	64.93	55.81	9.77
12.2	13256	40.2	26.9	0.1254	74.70	64.20	8.54
13.0	14137	39.6	27.1	0.1255	79.84	68.62	8.58
14.1	15345	39.1	27.1	0.1257	83.01	71.34	9.85
14.9	16330	39.3	28.4	0.1251	91.99	79.06	8.52
15.1	16549	37.3	26.3	0.1264	91.68	78.79	8.30

good. Maximum and average deviations from CFD model are 13.7% and 6.3%, respectively, whereas the same devations with respect to literature [8] are 10.7% and 3.4%, respectively. The results of copper and aluminum alloy are consistent, showing that the proposed sensor can operate with samples made of different materials (as long as the thermal conductivity is high enough to ensure a uniform temperature field).

In Fig. 3.6, are reported the result of additional experimental tests, where the power supplied to the sample is the varying parameter, in order to understand the optimal heat flux for the measurement. In this case, flow velocity equal to 3.4 m/s at the channel axis is kept fixed. Standard theoretical arguments require that a variation of the supplied power should not affect the value of the convective heat transfer coefficient, meaning that the supplied power is expected to show a linear behavior with respect to temperature difference.

This is confirmed in Fig. 3.6, where a linear best fit reveals a positive supplied power for a null temperature rise, defined as the difference between the temperature of the sample and that of air: $T_s - T_a$. However, we would expect that such a linear correlation passes through the origin of axes (i.e. no temperature difference is observed when the power supplier is

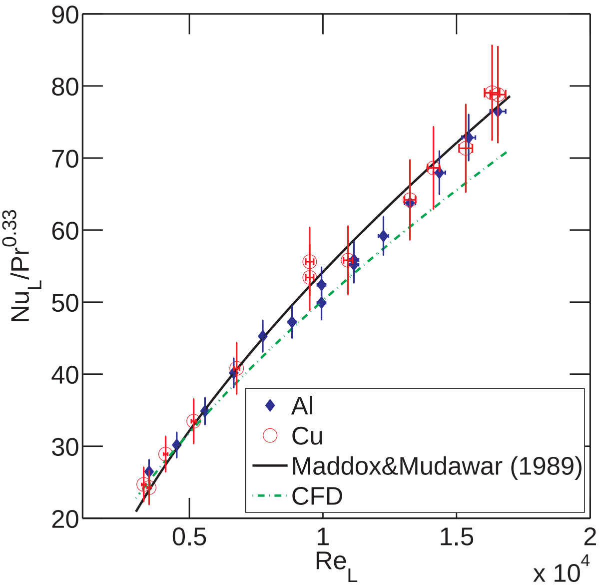

Figure 3.5: Comparison between experimental data, Maddox&Mudawar experimental correlation[8] and CFD model for aluminum alloy and copper smooth surface (see Ref. [4]).

off). This evidence can be explained as follows. All the measurements are based on the air temperature at the channel axis, see Eq. (3.9). However, in the present case, there is a small temperature difference between the air flowing inside the wind tunnel and the environment, because of the irreversibilities caused by the blower. The blower increases air temperature of roughly 2 K, and this generates a temperature difference between air and the channel walls. While air flows through the channel, the portion of air flushing close to the walls is cooled down by the walls. On the contrary, the air flowing at the channel axis experiences a weaker cooling. At the test section, the air thermal profile is slightly non-uniform: namely, air temperature at channel axis is slightly higher than the temperature of air flushing on the sample. When the latter is at the same temperature of the air flowing at the channel axis (the difference $T_s - T_a = 0\ K$), the sample is warmer than air passing in its close proximity and a small thermal power removal is observed (See Fig. 3.6).

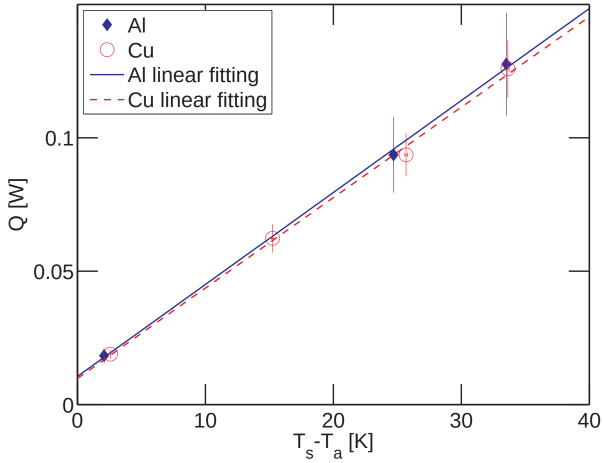

Figure 3.6: Linear correlation between power given to the sample and temperature difference between sample and air, for a constant air velocity (see Ref. [4]).

Now the experimental data shown in Table 3.2 and 3.3 are examined, in order to estimate how much this phenomenon affects the measurements reliability. At the test section, the temperature difference between air and walls is highly variable, with a maximum recorded value of $1.78\,K$ and a minimum one of $0.16\ K$. This means that slightly different thermal boundary layers showed up at the test section during the experimental campaign. This fact may have an effect on the measurement of the average convective heat transfer, as it is directly influencing the considered T_a at the denominator of Eq. (3.9). Instead of using the air temperature at the channel axis, i.e. T_a, one could use a proper corrected value, namely the adiabatic mixing temperature T_m, in Eq. (3.9), taking into account the actual temperature profile. For each experimental data shown in Table 3.2 and 3.3, one could estimate two values of h by setting $T_m = T_a$ (thus obtaining the value of h shown in Fig. 3.5) or $T_m = T_w$. Calculating the relative errors, defined as the differences between the h values calculated using $T_m = T_a$ and the h values calculated using $T_m = T_w$, a maximum and an average relative error equal to ±2.6% and ±1.5% has been found, respectively. The latter values are much smaller than the estimated overall measurement uncertainties, namely ±9.9% and ±6.7%. Hence it is possible to assume that the above phenomenon has a negligible effect for value of the heat flux equals or higher than those used in these experiments (i.e. $Q \geq 0.126\ W$), corresponding to a power density of $\geq 0.102\ W/cm^2$. The present release of the sensor works in range of $0.102 - 3.100\ W/cm^2$, where the maximum power density depends on the adopted heater. Maximum working temperatures are also estimated to be equal to $50 - 100$ Celsius for previous power densities. It is worth to point out that the above maximum working temperature and power density are mainly limited by the chosen heater, as well as by the present selection of materials. These thresholds can be easily overcome by proper design choices, without changing the main idea of the proposed sensor.

3.6. Discussion

In the present Chapter the experimental rig, used to characterize convective heat transfer coefficient of high efficient surfaces and devices proposed in the following of this work, has been described. In particular, design and validation of a purposely developed sensor for measuring convective heat flows is described in details. The key idea is to exploit the notion of thermal guard in order to significantly reduce the effects of spreading heat conduction losses. The maximum and mean estimated relative uncertainties for the convective heat transfer coefficient are found to be ±9.9% and ±6.7%, respectively. The experimental results are found to be in good agreement with both experimental data from the literature and a purposely developed computational fluid dynamic model. Maximum and average deviations of the measured Nusselt number from the estimated value by the numerical model are 13.7% and 6.3%, respectively. The comparison of reported measurement with literature [8] is even more satisfactory: Maximum and average deviations of Nu_L are found to be 10.7% and 3.4%, respectively.

The evidence that uncertainties due to (spreading) conduction losses can be effectively reduced by the thermal guard implies that no numerical model is required to post-process the measured quantities, and this leads to a direct measurement technique. The experimental rig can cope with quite small thermal fluxes (i.e. $< 0.2\ W/cm^2$), thus enabling the study of convective heat transfer enhancement methodologies in forced air (specific thermal fluxes here are order of magnitudes smaller than the one measured in [8]).

In the next Chapter, micro-pin fins arranged in regular patterns are investigated as a heat transfer enhancement technique. The aim is to develop a novel optimization method, suited for ”not subtractive” manufacturing technologies, devoted to design cost-effective heat transfer solutions. A certain number of configurations is experimentally characterized using the test rig described here. Such a long-lasting investigation necessarily require a purposely dedicated experimental bench for thermal characterization.

4. Patterns of micro-protrusions for enhanced convective heat transfer

In Chapter 3, the design of a purposely dedicated experimental rig has been presented. This has been developed in order to characterize thermal performances of high efficiency heat transfer surfaces and devices. In the present Chapter, this experimental rig is used to investigate patterns of diamond shaped, micro-pin fins (i.e. patterns of micro-protrusions or micro-protruded patterns) on flush mounted heat sinks for convective heat transfer enhancement. The role played by geometrical parameters and fluid-dynamic scales are discussed, and novel findings are pointed out. Moreover, a novel methodology specifically suited for micro-protruded patterns thermal optimization is designed, leading to 73 % enhancement in thermal performance respect to commercially available heat sinks, at fixed costs. Such a methodology is tailored to deal with devices fabricated by ”not subtractive” manufacturing technologies, e.g. Additive Manufacturing (AM). Contents of this Chapter can be also found in [7].

4.1. Motivations

This Chapter focuses on diamond shaped micro-protruded patterns, which are investigated as a promising method to enhance heat transfer performances of flush mounted heat sinks. More specifically, a systematic procedure based on design of experiments approach is proposed to:

- Investigate the convective heat transfer phenomenon, in order to understand, interpret and describe the effect of geometrical parameters and fluid-dynamic scales on heat transfer;

- Design a novel methodology suitable for a reliable and automatic thermal optimization of micro-protruded patterns fabricated by ”not subtractive” techniques (e.g. AM).

The Chapter is organized as follows. In Section 4.2, different diamond protruded patterns are rationally designed by taking advantage of the design of experiments approach. In Section 4.3, the results of experimental characterization are reported and a mathematical model describing the influence of geometrical parameters and flow regimes on thermal transmittance of diamond protruded patterns is developed. In Section 4.4, the thermal fluid-dynamics features of diamond micro-protruded patterns for heat sinks are discussed. Optimization methodology is proposed in Section 4.5. Finally, in Section 4.6, results are discussed.

4.2. Design of experiments

To obtain an independent benchmark of data, nine copper samples, each characterized by a peculiar Diamond micro-Protruded Pattern (DPP), are designed and manufactured by milling. The convective heat transfer coefficient for each sample is measured. The bottom part of each sample consists in a parallelepiped block (11.1 x 11.1 x 5 mm^3), which can be mounted in the experimental test bench described in Chapter 3. Samples are characterized by diamond micro-protrusions, which are arranged in a regular pattern. Each diamond shaped micro-protrusion is a parallelepiped pin, with a d x d square section rotated by 45 degrees with respect to the main flow direction. Protrusions are arranged according to a staggered configuration, as represented in Fig. 4.1.

A DPP is fully determined by 3 geometrical independent degrees of freedom (DoF). There are no constrains in choosing the DoF to use for the design, except for their property of independence. As an example, given the height of the protrusion H, the base edge of the protrusion d, the pitch between neighboring protrusions p (see Fig. 4.1), the number of protrusions N and $s = p - d$, a possible choice for the 3 DoF could be $\{H, p, d\}$. However, the use of dimensionless parameters is preferable, as they typically ensure a wider generality of results.

In previous studies on heat transfer through protruded patterns, the ratios between characteristic geometrical lengths have been adopted as governing parameters for the measured thermal performances. For example, Garimella *et al.* [34] chose the ratios between (i) spacing and protrusions height and (ii) channel height and protrusions height as significant parameters for characterizing heat transfer phenomenon in arrays of protruding elements. Leung *et al* [86], instead, chose the ratio between base length and height of protrusions, as well as the ratio between channel height and protrusions height as characterizing parameters.

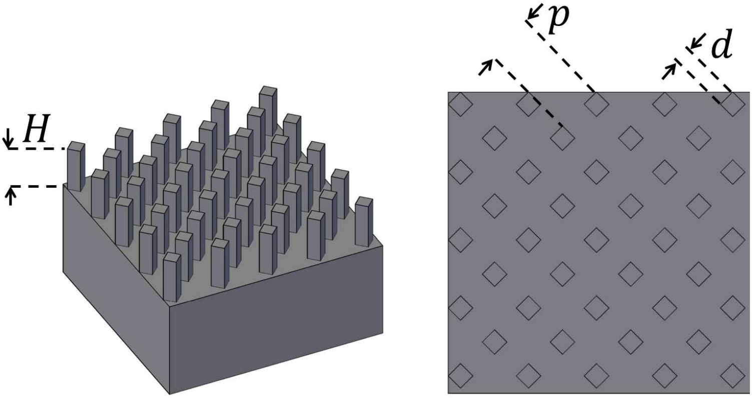

Figure 4.1: Sample geometry: Isometric view on left-hand side; Top view on right-hand side (See Ref. [7]).

In this work, to design the test matrix, a novel set of geometrical dimensionless parameters is considered. The investigation of those specific parameters is proved to be suitable in developing a novel methodology for the thermal optimization of micro-protruded patterns for heat sinks. In this context, the optimal configuration is the one ensuring the maximum thermal transmittance, at fixed amount of material needed to manufacture the micro-protrusions. In fact, the amount of used material is a suitable production cost indicator for most of the ”not subtractive” manufacturing technologies, both traditional (e.g. extrusion) and innovative (e.g. additive manufacturing) ones. In other words, optimal configuration is intended to be the one that guarantees the maximum thermal performance per unit of production costs. Parameters investigated in this study are:

- Plane solidity (or plan area density) λ_p, defined as the fraction of the root surface area (i.e. in our case $A_n = 11.1^2\ mm^2 = 123\ mm^2$) covered by protrusions (see Fig. 4.1, top view). This parameter expresses the pattern density, and it ranges from 0 to 1; Low values of λ_p refer to sparse patterns, whilst high values denote dense patterns (see also Fig. 2 in ref. [87]).

- Enhancement ratio in convective heat transfer surface area A/A_n, where A is the sample area, which is defined as the sum of root surface area and protrusions surface area, namely $A = A_n + 4dHN$.

- Dimensionless mixed length $V/(AY_0)$, where $V = NHd^2$ is the volume of the micro-protrusions and $Y_0 = 0.0503$ mm is the average viscous length (or average wall unit [88]), which is calculated as the mean viscous length over the range of fluid flows (i.e. Reynolds numbers) investigated in this study. The dimensionless mixed length is obtained as a ratio between geometric (V/A) and fluid-dynamic (Y_0) lengths. In particular, V/A represents the ratio between the amount of material for manufacturing the protrusions (i.e. production cost indicator) and the available surface area involved in the heat transfer phenomenon, while Y_0 is strictly related to the boundary layer thickness.

Comparing geometric and fluid-dynamics scales is essential to understand their interactions, as well as to determine how the optimal geometrical DPP configuration depends on the flow field. It is worth to mention that $V/(AY_0)$ is not the only mixed length analyzed in this study. In the following, the importance of the dimensionless protrusion height H/Y_0 is also discussed. This parameter represents the ratio between protrusion height and boundary layer thickness, and it quantifies the penetration of protrusions into the boundary layer. In the following, we refer to the three parameters defined above as *model* parameters, because they are expected to significantly affect both the thermal transmittance of the heat sink Tr $[W/K]$ and the volume of the micro-protruded pattern, therefore allowing to define an optimization criteria. λ_p plays a key role on the interactions between thermal fluid-dynamics structures (i.e. eddies, boundary layers, etc.) and micro-structures, thus strongly affecting the convective heat transfer coefficient h $[W/m^2/K]$. For instance, λ_p is often used to study the interactions between buildings and the atmospheric boundary layer [87] , but it has been demonstrated to be very effective in describing interactions between fluid-dynamics structures and micro-structures in a macroscopic channel too [3]. The A/A_n parameter is considered because heat flux, thus Tr, is strongly affected by the surface area involved in the heat transfer phenomenon. Since these two parameters are not directly linked to the production cost parameter (V), a third parameter $V/(AY_0)$ is also included.

The three model parameter described above can be expressed as function of the geometrical parameters $\{H, p, d\}$ as:

$$\lambda_p = \frac{Nd^2}{A_n} = \frac{d^2}{p^2}, \tag{4.1}$$

$$\frac{A}{A_n} = \frac{4dH}{p^2} + 1, \tag{4.2}$$

$$\frac{V}{AY_0} = \frac{Hd^2}{Y_0(4dH + p^2)}. \tag{4.3}$$

These equations are valid under the assumption that the number of protrusions N can be expressed as:

$$N = \frac{A_n}{p^2}. \tag{4.4}$$

Obviously, the model parameters have a physical meaning only if:

$$\begin{cases} 0 < \lambda_p < 1, \\ A/A_n > 1, \\ V/(AY_0) > 0. \end{cases} \tag{4.5}$$

Any existing DPP is fully determined by defining all components of the vector $\left\{\lambda_p, \frac{A}{A_n}, \frac{V}{AY_0}\right\}$. In this study the tested DPPs are designed taking advantage of the Design Of Experiments (DOE) approach. In particular, a Taguchi (or L9 orthogonal arrays) based, 3 levels - 3 factors, fractional DOE is applied [11]. Each parameter (or factor) can assume three possible values (or levels), namely low (1), medium (2) or high (3), as listed in Table 4.1. Therefore, once the levels per each parameters have been defined, the geometry of the nine DPPs to be tested is determined according to the test matrix proposed in ref. [11] and reported in Table 4.2.

Due to the rough tolerances of the milling process, the actual parameters of the samples are slightly different from the design values reported in Table 4.1: in Table 4.3, the model parameters and the extra geometrical quantities are reported for each sample. Fig. 4.2 shows how all samples are located in the parameter space; whereas Fig. 4.3 reports the pictures of the analyzed samples.

Table 4.1: Design values and associated levels for each model parameter (See Ref. [7]).

parameter level	λ_p	A/A_n	$V/(AY_0)$
1	0.15	1.5	2
2	0.35	2.5	2.75
3	0.55	3.5	3.5

Table 4.2: Test matrix [11] (See Ref. [7]).

sample	λ_p level	A/A_n level	$V/(AY_0)$ level
#1	1	1	1
#2	1	2	2
#3	1	3	3
#4	2	1	2
#5	2	2	3
#6	3	3	2
#7	3	1	3
#8	3	2	1
#9	2	3	1

It is worth to provide more details on the calculation of Y_0. The average viscous length Y_0 can be defined as:

$$Y_0 = \frac{1}{Re_{D,max} - Re_{D,min}} \int_{Re_{D,min}}^{Re_{D,max}} y_0(Re_D)\,\mathrm{d}Re_D \quad . \tag{4.6}$$

As demonstrated in [3], in case of smooth pipe turbulent flow, viscous length y_0 depends on the hydraulic diameter based Reynolds number $Re_D = vD/\nu$ as:

$$y_0 = \frac{D}{Re_D\,\sqrt{f_B/8}}, \tag{4.7}$$

where $f_B = f_B(Re_D) = 0.3164\,Re_D^{-1/4}$ is the friction factor expressed by the phenomenological correlation proposed by Blasius [89], v is the average fluid velocity, D is the hydraulic diameter, and ν is the fluid kinematic viscosity.

Table 4.3: Values of model parameters and extra geometrical quantities for the tested samples (See Ref. [7]).

Sample	λ_p	A/A_n	$V/(AY_0)$	H [mm]	d [mm]	p [mm]	s [mm]
#1	0.15	1.52	2.04	1.03	1.20	3.08	1.88
#2	0.15	2.57	2.99	2.45	1.00	2.62	1.62
#3	0.13	3.12	3.55	4.78	1.05	2.90	1.85
#4	0.28	1.47	2.55	0.70	1.60	3.00	1.40
#5	0.28	2.52	3.60	1.56	1.20	2.28	1.08
#6	0.44	3.28	2.76	1.05	0.80	1.20	0.40
#7	0.52	1.49	3.60	0.55	2.30	3.20	0.90
#8	0.37	2.32	2.21	0.56	0.67	1.10	0.43
#9	0.26	3.71	1.85	1.16	0.52	1.02	0.50

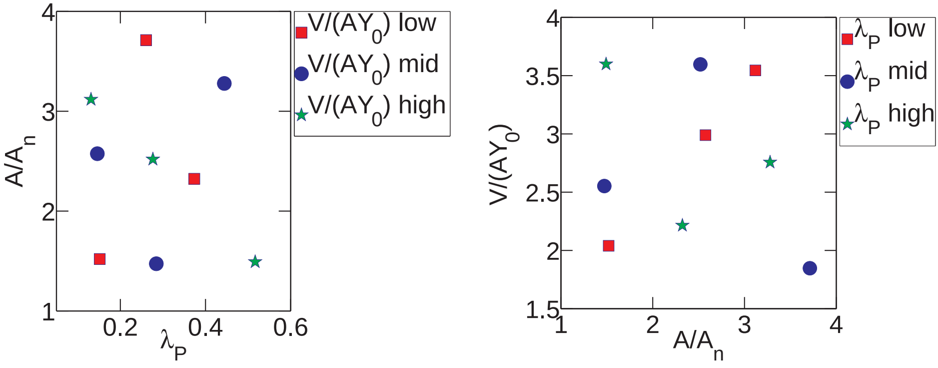

(a) (b)

Figure 4.2: Collocation of samples in the model parameter space. Due to manufacturing tolerances, a non uniform sampling of the parameter space is considered (See Ref. [7]).

4.3. Experimental characterization and data reduction

In this section, the experimental thermal characterization of all samples is provided. Moreover, the experimental results are compared to the model obtained by data reduction analysis.

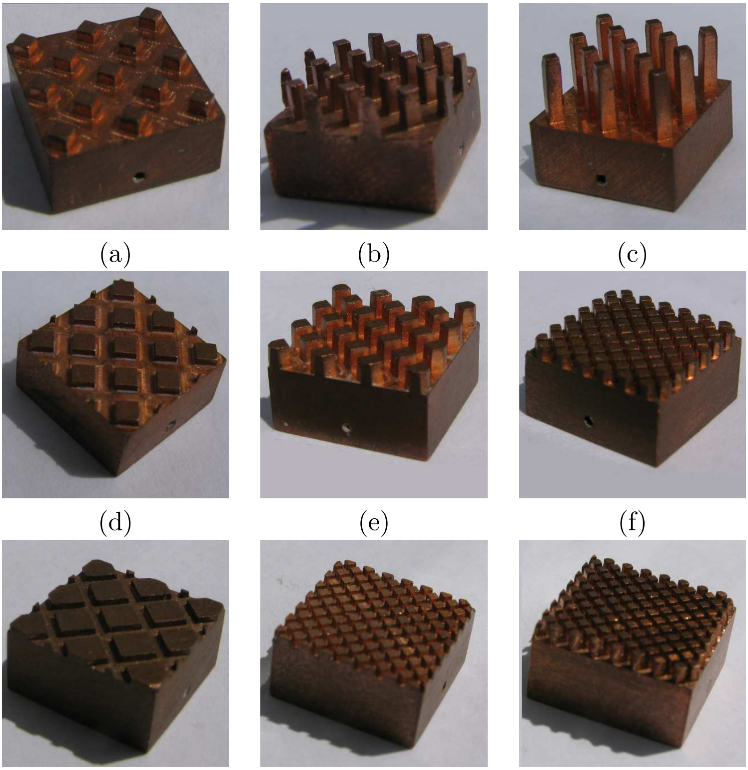

(a) (b) (c)

(d) (e) (f)

(g) (h) (i)

Figure 4.3: Tested samples (See Ref. [7]).

Experimental characterization has been carried on by the experimental rig described in Chapter 3. Heat transfer performance of each sample is reported as function of the heated edge, average velocity based Reynolds number $Re_L = vL/\nu$,, defined in Chapter 3.

In Fig. 4.4, the convective heat transfer coefficient of all samples is reported in terms of $Nu_L/Pr^{0.33}$, where Nu_L and Pr are respectively the dimensionless Nusselt and Prandtl numbers, defined in Chapter 3. In Fig. 4.5, thermal transmittances $Tr = hA$ of samples are shown. In both Fig. 4.4 and Fig. 4.5, the experimental characterization of a reference flat sample (i.e. without protrusion) is reported. The model is obtained by data reduction analysis discussed in the following. Finally, in Fig. 4.6, the results in terms of quantity Tr/V are reported. Error bars reported in Figs. 4.4, 4.5, 4.6 are estimated according to the methodology discussed in Chapter 3. It is worth to mention samples, with the same protruded patterns presented in Section 4.2, have been also fabricated by direct metal laser sintering (DMLS). Preliminary experiments, aiming to characterize these samples, revealed thermal performance of each sample by DMLS was similar than counterpart by milling. Hence the complete experimental characterization has been carried on for milled samples only.

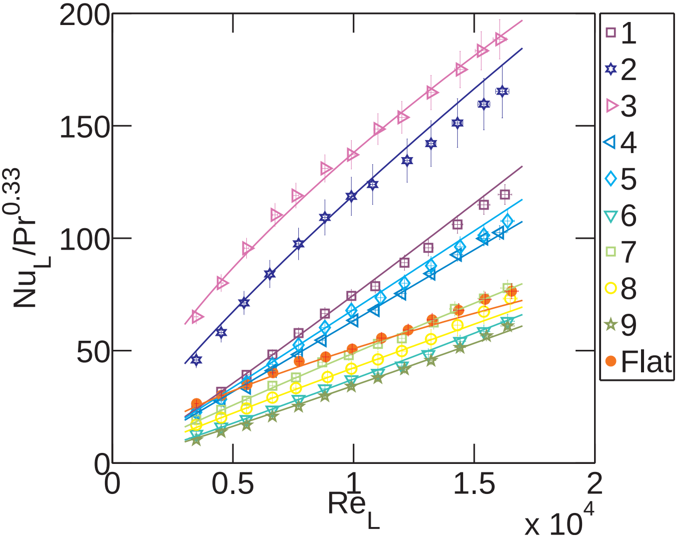

Figure 4.4: Comparison between experimental (symbols) and model (solid lines) results in terms of $Nu_L/Pr^{0.33}$ (See Ref. [7]).

In the following, a model able to predict the convective thermal transmittance of a generic DPP heat sink as a function of model parameters $\left\{\lambda_p, \frac{A}{A_n}, \frac{V}{AY_0}\right\}$ and fluid flow regime, namely Re_L, is presented. The model is based on data reduction on the experimental measurements of Tr. A reference Reynolds number is defined:

$$Re_{L,R} = 10^4, \tag{4.8}$$

while Tr is modeled as the product of two functions:

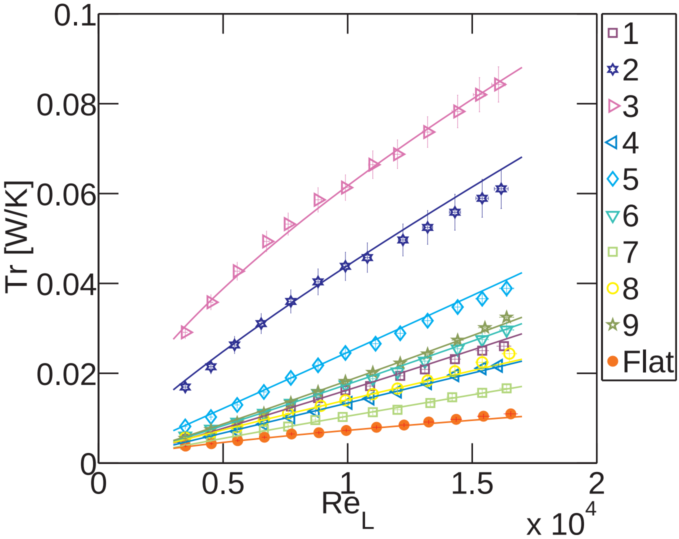

Figure 4.5: Comparison between experimental (symbols) and model (solid lines) results in terms of Tr (See Ref. [7]).

$$Tr = gTr_R. \tag{4.9}$$

In Eq. 4.9, Tr_R is the transmittance value at the reference Reynolds number, which is expected to depend on the model parameters $\left\{\lambda_p, \frac{A}{A_n}, \frac{V}{AY_0}\right\}$. On the other hand, g accounts for thermal transmittance as we move away from the reference flow regime, and it is modeled as a function of $\frac{H}{Y_0} = \frac{H}{Y_0}\left(\lambda_p, \frac{A}{A_n}, \frac{V}{AY_0}\right)$ and Reynolds number ratio $Re_L/Re_{L,R}$.

The quantity Tr_R can be split into $Tr_R = Tr_R^0 + \Delta Tr_R$, where Tr_R^0 is the transmittance of flat surface at the reference Reynolds number, while ΔTr_R is the additional transmittance due to the presence of DPP on the heat sink. Consequently, Tr_R can be modeled as:

$$Tr_R = Tr_R^0 + V\frac{\Delta Tr_R}{V}. \tag{4.10}$$

In this form, V represents the amount of additional raw material needed to manufacture the protruded pattern, while the parameter $\frac{\Delta Tr_R}{V}$ represents the enhancement in thermal transmittance of the device achieved per unit volume. $\frac{\Delta Tr_R}{V}$ is modeled by a second order polynomial function as:

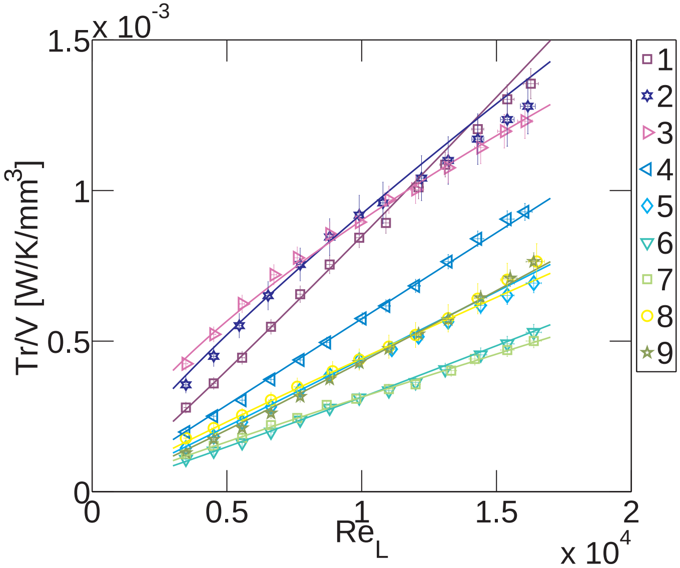

Figure 4.6: Comparison between experimental (symbols) and model (solid lines) results in terms of Tr/V (See Ref. [7]).

$$\frac{\Delta Tr_R}{V} = c_1\widehat{\lambda_p} + c_2\widehat{\frac{A}{A_n}} + c_3\widehat{\frac{V}{AY_0}} + c_4\widehat{\lambda_p}^2 + c_5\widehat{\frac{A}{A_n}}^2 + c_6\widehat{\frac{V}{AY_0}}^2 + c_7\widehat{\lambda_p}\widehat{\frac{A}{A_n}} + c_8\widehat{\lambda_p}\widehat{\frac{V}{AY_0}} + c_9\widehat{\frac{A}{A_n}}\widehat{\frac{V}{AY_0}}. \tag{4.11}$$

where the superscript $\widehat{}$ indicates the *normalized* model parameters, obtained as:

$$\begin{cases} \widehat{\lambda_p} = \frac{\lambda_p}{(\lambda_p)_{Avr}}, & (\lambda_p)_{Avr} = \frac{1}{9}\sum_{i=1}^{9}(\lambda_p)_i \\ \widehat{\frac{A}{A_n}} = \frac{\frac{A}{A_n}}{\left(\frac{A}{A_n}\right)_{Avr}}, & \left(\frac{A}{A_n}\right)_{Avr} = \frac{1}{9}\sum_{i=1}^{9}\left(\frac{A}{A_n}\right)_i \\ \widehat{\frac{V}{AY_0}} = \frac{\frac{V}{AY_0}}{\left(\frac{V}{AY_0}\right)_{Avr}}, & \left(\frac{V}{AY_0}\right)_{Avr} = \frac{1}{9}\sum_{i=1}^{9}\left(\frac{V}{AY_0}\right)_i \end{cases} \tag{4.12}$$

Subscript i in equation above denotes the i-th sample.

The vector $\{C\}$ =$\{c_1, c_2, c_3, c_4, c_5, c_6, c_7, c_8, c_9\}$ collects all the model coefficients, which are obtained by a regression procedure from the experimental data (see Appendix B for further details). In particular, from the data regression, $c_1 = -0.0003$, $c_2 = +0.0010$, $c_3 = -0.0003$, $c_4 = -0.0013$, $c_5 = -0.0011$, $c_6 = -0.0073$, $c_7 = -0.0041$, $c_8 = +0.0067$, $c_9 = +0.0076$ are obtained.

The function $g = \frac{Tr}{Tr_R}$ is modeled as:

$$g = \left(\frac{Re_L}{Re_{L,R}}\right)^B = \left(\frac{Re_L}{10^4}\right)^B, \tag{4.13}$$

where $B = B\left(\frac{H}{Y_0}\right)$ is computed as:

$$B = \log_{\frac{Re_L}{10^4}} \frac{Tr}{Tr_R}. \tag{4.14}$$

From the tested samples, ten experimental values of B are available for data regression. Considering a least mean squares fitting procedure, results are best fitted by:

$$B = d_1 \left(\frac{H}{Y_0}\right)^{d_2} exp\left(-d_3 \frac{H}{Y_0}\right) + d_4, \tag{4.15}$$

where the fitting parameters d_1, d_2, d_3, d_4 assume the values 0.003316, 2.3, 0.1039 and 0.66, respectively. In Fig. 4.7, the comparison between experimental values of B and the corresponding analytical model described by Eq. 4.15 is shown.

The proposed model reveals an excellent agreement with experimental data, as shown in Figs. 4.4, 4.5, 4.6.

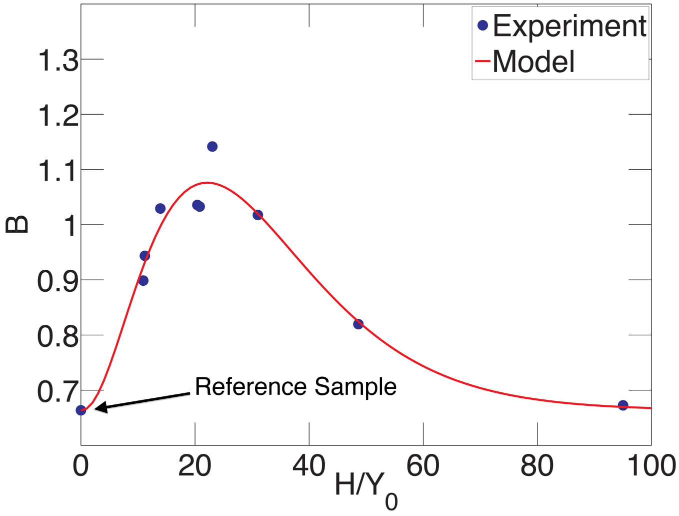

Figure 4.7: Comparison between experimental values of B and the best fitted analytical model (See Ref. [7]).

Finally, dimensionless fin parameter ml is introduced, where l is the protrusion height H defined in Table 4.3, and m is defined as [38]:

$$m = \left(\frac{4h}{\lambda_{Cu} d}\right)^{0.5}, \tag{4.16}$$

where $\lambda_{Cu} = 388\ W/m/K$ is the thermal conductivity of copper.

4.4. Thermal fluid-dynamics features of micro-protruded patterns

In the following, the experimental results presented in Section 4.3 are interpreted, and the main thermal fluid-dynamic features of diamond micro-protruded patterns discussed.

Before proceeding further, it is worth of note that the fin efficiency plays negligible role in convective heat transfer of the considered diamond micro-protruded patterns. In fact, here the temperature gradient along the protrusions length is very small. To prove this, for each protrusion ml is calculated by Eq. 4.16 considering $h = h_{max} = 200\ W/m^2/K$, i.e. the maximum convective heat transfer coefficient experimentally measured. As a result, the fin efficiency is higher than 98 % in all the considered samples, hence its effect is negligible.

The parameter λ_p plays a key role in controlling the condition of fluid stagnation and, consequently, the convective heat transfer coefficient. As shown in Fig. 4.4, samples characterized by low λ_p (i.e. #1, #2 and #3) experience larger values of $Nu_L/Pr^{0.33}$ than samples with higher λ_p (i.e. #6, #7, #8 and #9). Focusing on sparse patterns (low λ_p) it can be noticed that H significantly influences $Nu_L/Pr^{0.33}$, which monotonically increases with H. This is due to the fact that higher protrusions are able to penetrate deeper in the fluid boundary layer, hence they are flushed by stronger flow field (see Fig. 4.4). This phenomenon allows to achieve a huge increase in convective heat transfer: the sample with the highest protrusions (sample #3) experiences an enhancement in $Nu_L/Pr^{0.33}$, almost constant over the entire range of Re_L under study, up to 150 % as compared to flat surfaces, while Tr increases up to 700 %. On the other hand, by increasing the density of patterns (i.e. increasing λ_p), fluid stagnation takes place and consequently $Nu_L/Pr^{0.33}$ decreases. In particular, very high density patterns, can experience values of $Nu_L/Pr^{0.33}$ even lower than flat surface (see sample #6, #7, #8 and #9). In Fig. 4.8, the influence of λ_p on $Nu_L/Pr^{0.33}$ is shown. Here, a comparison of nine experimental points with an exponential-based fitting curve is reported. This clearly demonstrates that λ_p plays a significant role: $Nu_L/Pr^{0.33}$ monotonically decreases with increasing λ_p, even though this result is limited to the range of λ_p considered in this work. The latter experimental evidence underlay a phenomenon very similar to the one of bypass flow experienced by unshrouded heat sinks and described in Section 2.2: If heat sink package became too dense (i.e. λ_p increases) air flows avoid to pass through fins (i.e. protrusions), resolving in a reduction of convective heat transfer.

In all the tested samples, H/Y_0 plays a key role in determining how the fluid flow regime, i.e. Re_L, influences the thermal transmittance. In particular, Fig. 4.7 suggests that an optimal value of H/Y_0 exists, which lies in the range $10 < H/y_0 < 40$, where protrusions are at least twice the viscous sub-layer height ($\approx 5\ y_0$ according [88]), but still short enough to remain in the viscous wall region ($\leq 50\ y_0$ according [88]). Being y_0 inversely proportional to the Reynolds number (according Eq. 4.7) the optimal height H is expected to be function (monotonically decreasing) of the Reynolds number too. This is confirmed by experimental results: Being $\frac{Tr}{V}$ the pa-

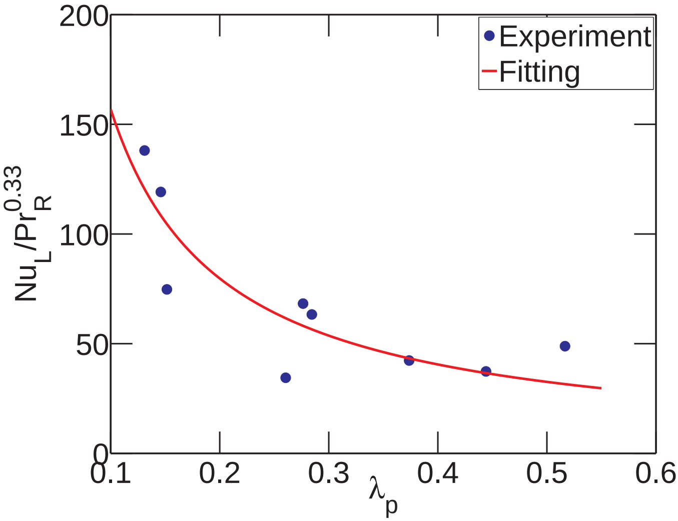

Figure 4.8: Influence of λ_p on $Nu_L/Pr^{0.33}$ (See Ref. [7]).

rameter to maximize, and focusing on the three samples characterized by the lowest values of λ_p (hence the highest convective heat transfer coefficient), it could be noticed in Fig. 4.6 that in the low Reynolds number range ($0.3 \times 10^4 < Re_L < 0.9 \times 10^4$) the sample #3 (with the highest value of H), experiences the highest $\frac{Tr}{V}$. In the intermediate Reynolds number range ($0.9 \times 10^4 < Re_L < 1.4 \times 10^4$), the sample #2 (with the intermediate H, among the three ones) experiences the highest $\frac{Tr}{V}$. Finally, in the high Reynolds number range ($1.4 \times 10^4 < Re_L < 1.7 \times 10^4$), the sample #1 (with the lowest H) experiences the highest $\frac{Tr}{V}$. Consequently, The optimal configuration depends on Re_L.

4.5. Optimization methodology for micro-protruded patterns

In this section, an automatic methodology for thermal optimization of diamond micro-protruded patterns for heat sinks is presented. In addition, the algorithm is implemented and applied to a real case study and results are reported and discussed.

Input parameters of the algorithm are the heat sink working conditions, namely Reynolds number $Re_{L,W}$, heat flux to be removed Q_W and the temperature difference between heat sink and cooling fluid ΔT_W. As a result, the automatic optimization algorithm provides geometrical configurations, (in terms of $\left\{\lambda_p, \frac{A}{A_n}, \frac{V}{AY_0}\right\}$ or equivalently $\{H, d, p\}$) that maximize $\frac{Tr_W}{V}$ (namely the thermal transmittance per unit of production cost), while guarantee $Tr = Tr_W = \frac{Q_W}{\Delta T_W}$.

The proposed algorithm considers all the possible configurations, i.e. parameter combinations $\left\{\lambda_p, \frac{A}{A_n}, \frac{V}{AY_0}\right\}$, within the parameter range investigated by experiments (where data regression is proved to be valid). For each configuration, the algorithm calculates the corresponding values of V and Tr through the model provided by data regression (Eq. 4.9). Among all the possible configurations, the algorithm retains the ones that guarantee $Tr = Tr_W$ and discard the others. Finally, among the retained configurations, the one characterized by the minimum value of V is chosen. In particular, the parameter space (i.e. the possible DPP configurations) is numerically explored as follows: Each parameter can assumes 20 possible discrete values, by uniformly partitioning the parameter range. Then, the algorithm calculates the value of Tr associated to each of the $20^3 = 8000$ possible DPP configurations (i.e. possible combination of the 3 model parameters). Tr_W is compared to the value of Tr for each configuration, and configurations that match Tr_W with a tolerance of 5% are retained.

As discussed in section 2.4 heat transfer devices typically includes both thermal transmittances and pressure losses, hence optimization problems usually deal with efficiency parameters that consider both the aforementioned phenomena, e.g. aerothermal efficiency η_A defined in Section 2.4. In this work, the effects of protruded patterns on pressure losses are neglected, because this study is focused on applications where these effects are not significant. Nevertheless, it is worth to stress that the methodology presented in this work could be extended to a more general case, by simply substituting $\frac{Tr_W}{V}$ (thermal performances per unit of production cost) with η_A as the parameter to be maximized, as described in Section 2.4

As a real case study, the developed algorithm is used to perform thermal optimization of DPP heat sink, i.e. maximum transmittance per unit of production costs, for three different Reynolds numbers, namely $Re_L = 0.5 \times 10^4, 10^4$ and 1.5×10^4, and with a range of transmittance values: $0.02 < Tr_W < 0.1\ W/K$. In Tables 4.4, 4.5, and 4.6 the optimal geometrical parameters of DPP heat sinks for different Tr are reported, in the case of $Re_L = 0.5 \times 10^4, 10^4$ and 1.5×10^4, respectively. It is worth of note that for $Re_L = 0.5 \times 10^4$ the maximum transmittance is $Tr = 0.045\ W/K$, because the parameter space explored in the optimization process is limited to the one investigated by experiments. Fig. 4.9 summarizes results of that case study: on the abscissa is reported DPP volume V, namely the production cost index, while on the ordinate the maximum (hence optimal) thermal transmittance Tr_{max} achieved for the three Reynolds numbers under exam is shown. It can be noticed that the volume, and consequently the production cost of the device, increases by decreasing Re_L (worst convective heat transfer). In Table 4.7 optimal designs obtained by imposing $Tr_W = 0.03\ W/K$ for the three different Re_L are compared. It is worth of note that optimal values of H chosen by optimization algorithm are such that the corresponding ratio H/y_0 lies in the range $30 \div 35$. This result strengthen the hypothesis, exposed in Section 4.4, of the existence of an optimal value of H/y_0 lying in the range $10 < H/y_0 < 40$. Finally, it is interesting to compare the configurations obtained from the optimization algorithm with the nine tested samples. Focusing on reference flow conditions ($Re_{L,R} = 10^4$), Fig. 4.6 shows that sample #2 has the best value of transmittance per production costs unit (i.e. highest Tr/V) among the tested samples, being characterized by $Tr = 0.044\ W/K$ and $V = 47.7\ mm^3$. Instead, As shown in Fig. 4.9 and Tab. 4.5, the optimal configuration found by the algorithm allows to achieve $Tr = 0.092$ with the same amount of material, i.e. at fixed production costs. Therefore, this example shows that the presented thermal optimization procedure would allow to achieve a 110 % enhancement in the thermal transmittance of the best performing tested sample, while keeping production costs unchanged.

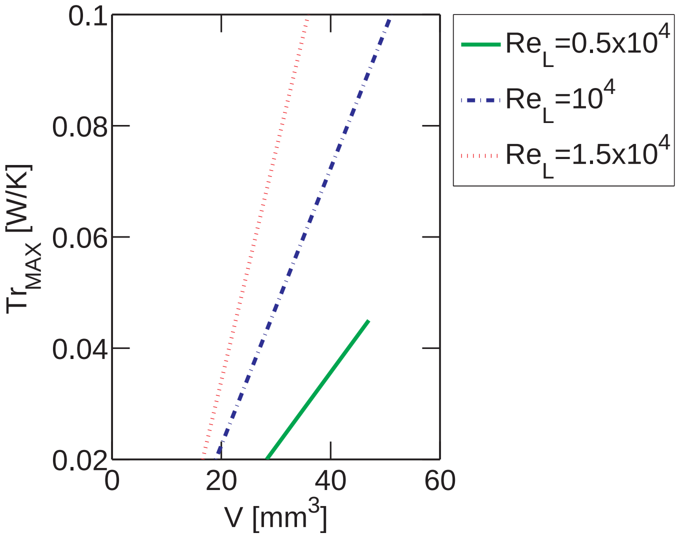

Figure 4.9: Case study results: Optimal thermal transmittance versus DPP volume (See Ref. [7]).

Table 4.4: Optimal design parameters for $0.02 < Tr < 0.045$ $[W/K]$ and $Re_L = 0.5 \times 10^4$ (See Ref. [7]).

H $[mm]$	d $[mm]$	p $[mm]$	λ_p $[-]$	$\frac{A}{A_n}$ $[-]$	$\frac{V}{AY_0}$ $[-]$	Tr $[W/K]$	V $[mm^3]$
1.77	0.59	1.64	0.13	2.55	1.79	0.020	28.31
2.03	0.64	1.77	0.13	2.66	1.98	0.026	32.58
2.30	0.64	1.77	0.13	2.87	2.07	0.031	36.83
2.55	0.61	1.69	0.13	3.18	2.07	0.037	40.88
2.81	0.58	1.62	0.13	3.50	2.07	0.042	44.94
2.93	0.61	1.69	0.13	3.50	2.17	0.045	46.98

Table 4.5: Optimal design parameters for $0.02 < Tr < 0.1$ $[W/K]$ and $Re_L = 10^4$ (See Ref. [7]).

H $[mm]$	d $[mm]$	p $[mm]$	λ_p $[-]$	$\frac{A}{A_n}$ $[-]$	$\frac{V}{AY_0}$ $[-]$	Tr $[W/K]$	V $[mm^3]$
1.18	0.87	2.40	0.13	1.71	1.79	0.020	19.0
1.69	0.61	1.69	0.13	2.45	1.79	0.038	27.1
2.17	0.57	1.58	0.13	2.97	1.88	0.056	34.7
2.55	0.61	1.69	0.13	3.18	2.07	0.073	40.9
2.93	0.61	1.69	0.13	3.50	2.17	0.091	47.0
3.19	0.66	1.84	0.13	3.50	2.35	0.100	51.1

Table 4.6: Optimal design parameters for $0.02 < Tr < 0.1$ $[W/K]$ and $Re_L = 1.5 \times 10^4$ (See Ref. [7]).

H $[mm]$	d $[mm]$	p $[mm]$	λ_p $[-]$	$\frac{A}{A_n}$ $[-]$	$\frac{V}{AY_0}$ $[-]$	Tr $[W/K]$	V $[mm^3]$
0.59	1.08	2.25	0.13	1.50	1.79	0.020	16.6
1.33	0.75	2.08	0.13	1.92	1.79	0.038	21.3
1.62	0.63	1.74	0.13	2.34	1.79	0.056	26.0
1.84	0.58	1.60	0.13	2.66	1.79	0.073	29.5
2.13	0.53	1.48	0.13	3.08	1.79	0.091	34.1
2.24	0.56	1.56	0.13	3.08	1.88	0.100	35.9

Table 4.7: Optimal design parameters for $Tr = 0.03\ W/K$ at three different Reynolds numbers (See Ref. [7]).

Re_L	Isometric view	Side view	Top view	H	y_0	H/y_0
$[-]$				$[mm]$	$[mm]$	$[-]$
0.5×10^4	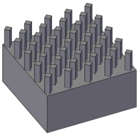	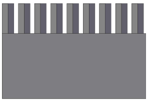	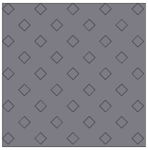	2.3	0.076	30
10^4	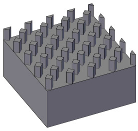	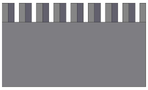	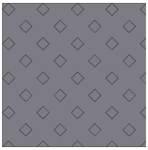	1.48	0.041	35
1.5×10^4	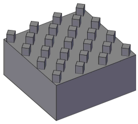		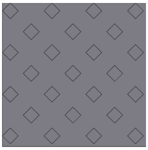	1.07	0.029	36.5

4.6. Discussion

Diamond shaped micro-protruded patterns to enhance convective heat transfer have been investigated in this Chapter. Two main goals are achieved:

- The effect of geometrical parameters and fluid-dynamic scales on convective heat transfer phenomenon are illustrated.
- A methodology suited for the thermal optimization of diamond micro-protruded patterns, fabricated by ”not subtractive” techniques (e.g. AM), is proposed and implemented.

Concerning the effect of geometrical parameters and fluid-dynamic scales, $Nu_L/Pr^{0.33}$ exhibits a decreasing trend with increasing λ_p. In particular, All DPPs characterized by $\lambda_p > 0.33$ clearly show a heat transfer coefficient lower than the flat case (i.e. no protrusions), due to fluid stagnation. Concerning sparse patterns (low λ_p), it is proved that H plays a key role, namely the dimensionless group $Nu_L/Pr^{0.33}$ monotonically increases with H. In fact, DPP #3, characterized by low λ_p and the highest H among all the tested samples, shows the maximum enhancement in $Nu_L/Pr^{0.33}$ and Tr, up to 150 % and 700 %, respectively. This is due to the fact that high protrusions are able to penetrate deeper in the fluid boundary layer. On the other hand, experimental evidence and optimization procedure suggest the maximum Tr/V, i.e. thermal transmittance per unit of production costs, is reached when $H/y_0 = 30 \div 35$.

A novel methodology is developed for thermal optimization of diamond micro-protruded patterns for heat sinks. An automatic algorithm based on this methodology is implemented and tested. Provided the heat sink working conditions, an optimization procedure is suggested that calculates the optimal geometrical configuration ensuring the required thermal performances while maximizing the thermal transmittance per unit of production costs. Comparing a representative commercial micro-protrusion patterned heat sink with the optimal configuration determined by the algorithm, the second achieves an enhance in thermal performance per unit production cost up to 73% (refer to Appendix C for details). This demonstrates that the proposed methodology may lead to significant improvement in heat transfer performances, while keeping unchanged the production costs. The proposed optimization methodology has rather a general validity, and can be extended to different micro-protruded or micro-structured patterns, especially if manufactured by ”not subtractive” techniques (e.g. Additive manufacturing). Moreover, this methodology can be easily extended in order to deal with operational costs too (i.e. pressure drops induced by heat sink), by simply substituting η_A to Tr/V as objective function to be maximized.

It is worth to mention samples, with the same geometrical features of the ones presented in this Chapter, have been fabricated in aluminum alloy by direct metal laser sintering (DMLS) too. The latter is an additive manufacturing (AM), i.e. ”not subtractive”, technique. Preliminary test revealed each sample by DMLS experienced similar thermal performances than counterpart by milling. In the next Chapter peculiarities of DMLS are further investigated. In particular, *artificial roughness* by DMLS is optimized to obtain convective heat transfer performances superior than milled counterparts.

5. Rough surfaces with enhanced heat transfer by direct metal laser sintering

In Chapter 4 diamond protruded patterns (DPPs) produced by both additive manufacturing (AM) and milling have been fabricated and convective heat transfer coefficient has been measured by mean of experimental rig described in Chapter 3. In particular, AM samples have been manufactured in aluminum alloy by direct metal laser sintering (DMLS). Thermal characterization reveals DPPs produced by AM have similar performance than milled ones. Nevertheless, AM allows heat transfer performances higher than traditional manufacturing techniques, when its peculiarities are properly exploited. Aiming to unveil potentiality of AM in heat transfer, in this Chapter different rough surfaces obtained by DMLS are fabricated and thermally characterized. In fact, surface roughness of parts fabricated by DMLS can be tuned by controlling DMLS process parameters. As a result, convective heat transfer enhancement up to 73%, compared with smooth surfaces by milling, is demonstrated. Contents of this Chapter can be also found in [3].

5.1. Motivations

Additive manufacturing (AM) techniques (often referred to as layer manufacturing or rapid prototyping) allow to build highly complex components from a three-dimensional computer-aided design (CAD) model without part-specific tooling [90]. Selective Laser Melting (SLM) (also referred to as direct metal laser sintering - DMLS) is an AM process where a laser source selectively scans a powder bed according to the CAD-data of the part to be produced. The high intensity laser beam makes it possible to completely melt and fuse the metal powder particles together to obtain almost fully dense parts. Successive layers of metal powder particles are melted and consolidated on top of each other resulting in near-net-shaped parts [90]. Research in recent years has identified the potential of this process to build metallic components that can act as functional prototypes. The ability of SLM to produce complex three-dimensional structures with features that would be difficult if not impossible to manufacture using conventional methods has been already explored for building heat sinks [91], as well as miniature heat exchangers and radiators [39]. Moreover, with the proper choice of input conditions, DMLS can build full dense parts with mechanical properties equivalent or even superior to those of parts produced by conventional manufacturing [92, 93]. Finally, the surface morphology of these parts can also be tuned, in order to produce artificial roughness with some desired features.

The Chapter is organized as follows. Samples manufacturing methodology is discussed in detail in Section 5.2; Morphological and radiative characterization of rough surfaces is reported in Section 5.3; Experimental data on convective heat transfer measurements are discussed in Section. 5.4. Finally, in Section 5.5, conclusions are drawn.

5.2. Rough surfaces by direct metal laser sintering (DMLS)

Current state-of-the-art DMLS techniques allow to produce bulk object without significant porosity. Using optimized process parameters is possible to obtain a residual porosity below 0.8% [93]. Due to its versatility in terms of both materials and shapes, the main advantage of DMLS is to produce metal complex-shaped components in one step. In the present study, all samples are made of AlSiMg alloy supplied by EOS GmbH. The above alloy comes as a powder, whose element shape, dimensions, size distribution (with volume assumption), chemical composition and percentage in weight were assessed in a previous work [93]. The aluminum alloy specimens were prepared by DMLS with an EOSINT M270 Xtended version. In this machine, a powerful Yb (Ytterbium) fiber laser system in an Argon atmosphere is used to melt powders.

DMLS process starts with the creation of a three-dimensional CAD-model of an object. Then the model is converted to a STL file format. This file defines optimal building direction of the physical object and it is based on small triangles, which determine the accuracy and contours of the whole object. Then, the support structures are generated and subsequently, together with the STL model, are sliced into horizontal layer of 30 μm thickness. These SLI format files are then transferred to the computer of the DMLS machine, which now has the necessary information to build up each layer. The essential operation in the DMLS process is the laser beam scanning over the surface of a thin powder layer previously deposited on a substrate. The forming process goes along the scanning direction of the laser beam. Each cross-section (layer) of the part is sequentially filled with elongated lines (vectors) of molten powder. The quality of a part produced by this technology depends strongly on the quality of each single vector and each single layer. Identification of the optimal process parameters of laser power, scanning speed and hatching distance is a crucial task because these parameters happen to be the most influential on the parts characteristics: surface quality, porosity, hardness and mechanical properties [9].

Accuracy and part surface quality has become the focus of AM community with the increased requirement of prototyped functional parts, enhanced material properties for strength and dimensional tolerance comparable to conventionally producible parts. Since the whole object is manufactured starting from tessellation of a 3D CAD model, the contour of a DMLS part is a stepped approximation of the contour of the nominal CAD model. As a result of this, all parts manufactured by AM processes exhibit a staircase effect. The uniform slicing procedure directly affects the extent of the staircase effect that appears especially along inclined planes and curved surfaces. As the inclination angle is reduced or the layer thickness is increased, the stair-effect becomes more pronounced. When the slicing thickness is thinner, the staircase is smaller and the surface will be smoother. The error associated with the staircase effect can be quantified

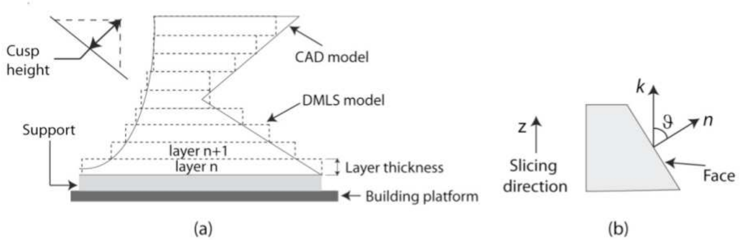

Figure 5.1: (a) Staircase effect on the DMLS model; (b) Building orientation (See Ref. [3]).

by considering the cusp height in Figure 5.1(a) which is the maximum distance between the nominal part boundary and the boundary of the part produced by DMLS. In any building orientation, the part is defined with its base on the xy-plane, the building direction along the z axis and the angle ϑ defined as the angle between the vector normal to the face (n) and the slicing direction (k) - see Figure 5.1(b). When the intersection angle ϑ is equal to or less than the critical value, the region needs adding support. The need to improve the surface finish of the parts produced by DMLS has led to a variety of researches on reducing of the staircase effect on inclined and curved surfaces and on the choice of the process parameters. In this study, starting from the results obtained previously on the optimization of process parameters on surface finish of AlSiMg sample produced by DMLS [9], values which can modify and increase the surface roughness were chosen. Samples dimension were 11.1 × 11.1 × 5 mm and they were orientated with angles from 90° to 0°. The parts with angles from 40° to 30° show a higher surface roughness due to the staircase effect.

Table 5.1: Thermal properties of parts [12]. Heat treatment (last column) by annealing process for 2 h at 573 K for stress relieve (See Ref. [3]).

	As built	Heat treated
Thermal conductivity		
- in horizontal direction	103 ± 5 $W/m/K$	173 ± 10 $W/m/K$
- in vertical direction	119 ± 5 $W/m/K$	175 ± 10 $W/m/K$
Specific heat capacity		
- in horizontal direction	920 ± 50 $J/kg/K$	890 ± 50 $J/kg/K$
- in vertical direction	910 ± 50 $J/kg/K$	900 ± 50 $J/kg/K$

However, a higher surface roughness should not be detrimental concerning the residual sub-surface porosity, otherwise the heat transfer performance may be negatively affected. To avoid such effect, the laser speed on the surface and sub-surface region must be kept as constant as possible. This is not trivial because during scanning a certain time is needed to accelerate the mirrors to the desired speed. This is due to inertia of mirrors used for scanning. During this time, the laser beam moves at a non constant speed: hence more energy is applied at the edges of the part than in the bulk. To avoid this situation, the mirror is accelerated already before the start of the part so that it has reached the desired speed before the beginning of exposure (skywriting option in EOS GmbH technology). This strategy proved to be effective for building the present samples with extremely low porosity (see Fig. 5.5). Low porosity ensures very good thermal properties of parts, which can be improved even further by heat treatment, as shown in Table 5.1.


(a) (b) (c) (d)

Figure 5.2: Tested samples made of AlSiMg alloy by direct metal laser sintering (DMLS): (a) sample #1, average roughness $R_a = 16$ μm; (b) sample #2, $R_a = 24$ μm; (c) sample #3, $R_a = 43$ μm; (d) sample #4, finned surface, roughly $R_a = 22$ μm as average on both sides (See Ref. [3]).

After being manufactured and removed from the building platform, five parallelepiped facets are milled in order to fit into the convective heat sensor presented in Chapter 3. The remaining sample facet maintains the original roughness due to the DMLS manufacturing and it will be named rough surface in the following description. The first three samples are characterized by flat rough surfaces, see subplots (a, b, c) in Fig. 5.2. In the fourth sample, see subplot (d) in Fig. 5.2, the rough surface has an additional orthogonal fin of size $11.1 \times 10 \times 2$ mm, in order to explore finned surfaces as well. Finally, the fifth sample, see Fig. 5.3, is obtained by milling both horizontal surfaces and fin half sides of the fourth sample. For convenience, the tested samples (reported in Fig. 5.2) are identified by the standard average roughness R_a. However, a more sophisticated surface characterization (with respect to R_a) will be discussed in the following section. Those samples were obtained by varying the angle between the rough surface and the hatching DMLS plane in order to explore the impact of this parameter on the surface morphology and consequently on the thermal performances.

Figure 5.4 shows the angle of construction of the samples, the process parameters used for rough surface and the average roughness obtained.

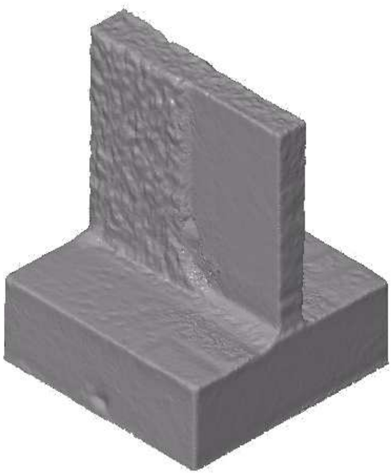

Figure 5.3: Example of 3D optical scan of sample #5 made by milling both horizontal surfaces and fin half sides, after testing sample #4. The other physical dimensions remain the same (See Ref. [3]).

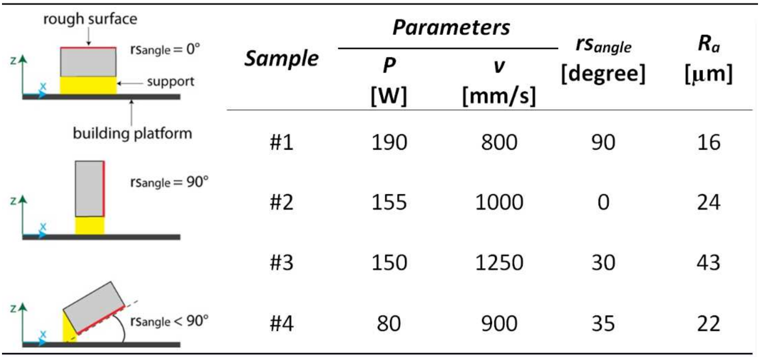

Sample	Parameters		rs_{angle} [degree]	R_a [µm]
	P [W]	v [mm/s]		
#1	190	800	90	16
#2	155	1000	0	24
#3	150	1250	30	43
#4	80	900	35	22

Figure 5.4: Process parameters and orientation in the building platform of the samples produced by DMLS, where P and v are laser power and scan speed, respectively [9] (See Ref. [3]).

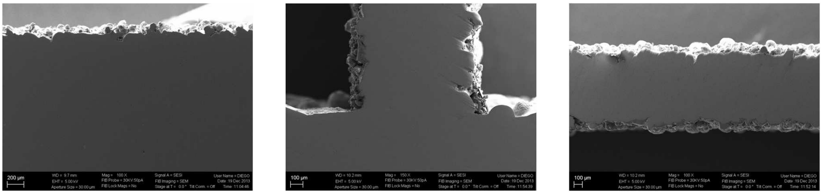
(a) (b) (c)

Figure 5.5: Characterization of the residual porosity of the DMLS samples by Field Emission Scanning Electron Microscopy (FESEM): No sub-surface porosity is visible. (a) sample #1; (b) sample #4, fin root; (c) sample #4, finned surface, fin middle (See Ref. [3]).

The angle considered was the one comprised between the rough surface and building platform (rs_{angle}). The considered samples have extremely low porosity (see Fig. 5.5). Heat treatment has been applied to all tested samples, in order to improve further their thermal properties (see Table 5.1 for details). Smooth samples (both in aluminum and copper) made by milling with $R_a \approx 1\ \mu m$ were also used as a reference. The latter roughness value is typical of heat dissipators for electronics, which are usually obtained by traditional manufacturing techniques, and hence it is particularly suitable for estimating the relative thermal enhancement.

5.3. Morphological and radiative characterization of rough surfaces

In this section, a detailed morphological analysis is reported for the tested samples shown in Fig. 5.2. First of all, the samples were characterized by a 3D optical scanner ATOS Compact Scan 2M (GOM GmbH) with the results reported in the subplots (a, c, e) of Fig. 5.6. The latter figures reveal a complex multi-scale morphology (at least for samples #1 and #3), which could be ascribed to the contour parameters used together with the powder adopted. In fact the mean particle diameter ranges from 0.5 to 40 μm, but the small particles are far more (in number) than the bigger ones, thus creating clusters with complex morphology at the micro-metric scale. On the other hand, in sample #2, as described in the previous paragraph,

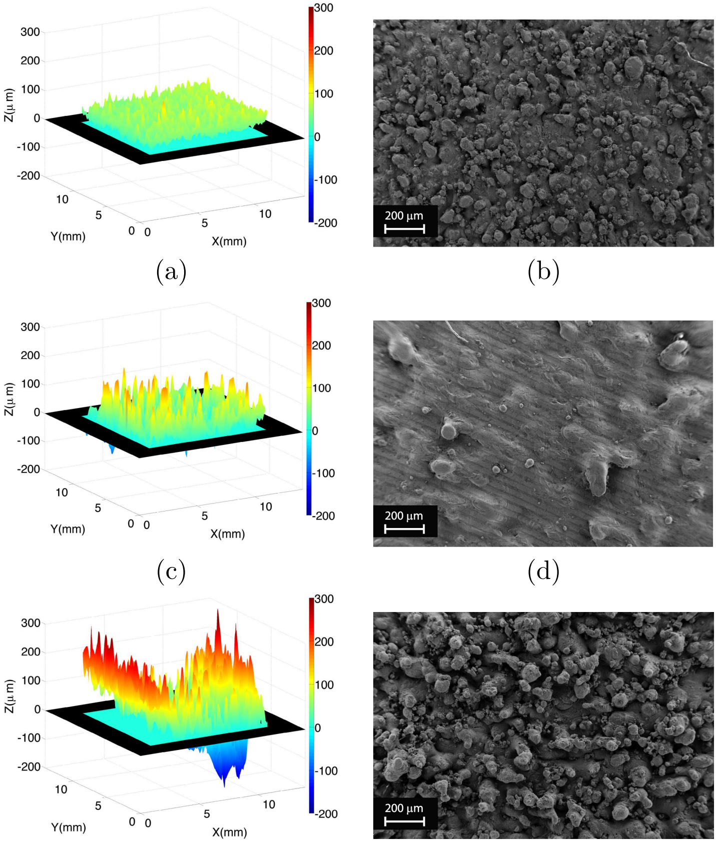

(a) (b)

(c) (d)

(e) (f)

Figure 5.6: Surface morphological characterization of flat samples: (a, c, e) by 3D optical scanner referring to the fluid-dynamic plane and (b, d, f) by Field Emission Scanning Electron Microscope; (a, b) sample #1, $R_a = 16$ μm; (c, d) sample #2, $R_a = 24$ μm; (e, f) sample #3, $R_a = 43$ μm (See Ref. [3]).

the rough surface was parallel to the hatching plane, so associated to different building parameters, and this allows the free metal surface (due to laser melting) to smooth out more homogeneously. It could be noticed that the FESEM images are reported by planar view, thus it is not simple to estimate therein the actual height of the peaks.

In order to make more quantitative analysis, let us introduce the so-called *R-parameters* [94] and the *S-parameters* [95]. First, the arithmetic average height parameter R_a is defined as

$$R_a = \frac{1}{n} \sum_{i=1}^{n} |z_i - z_m|, \tag{5.1}$$

where z_i is the height of the generic rough surface point i-th with respect to the reference plane, $z_m = z_m(s)$ is the least squares mean line of the rough profile (not necessarily constant), s is the generalized coordinate of the profile and n is the number of profile points measured by a rugosimeter. Clearly, the above definition holds under the assumption of homogeneously distributed profile points, as usually occurs in this kind of measurements. Another popular *R-parameter* is given by R_z, which is the difference in height between the average of the five highest peaks and the five lowest valleys along the assessment length of the profile. This value is usually larger than R_p, which is the maximum height of the linear profile.

Previous parameters have the limitation of referring to a specific profile measured by the rugosimeter and they may lead to inaccurate estimates for the whole surface. Hence the *S-parameters* [95] have been proposed. The arithmetical mean height of the surface S_a has a definition very similar to Eq. (5.1), but now z_m is the least squares mean plane of the rough profile, namely $z_m = z_m(s_1, s_2)$, where s_1 and s_2 are the two planar generalized coordinates. Similarly, S_p is the maximum height of the peak and S_q is the root mean square height of the surface. Moreover, high order moments are also commonly used. For example, the skewness S_{sk} (third order moment) and the kurtosis S_{ku} (fourth order moment). The sign of S_{sk} indicates the predominance of peaks (i.e. $S_{sk} > 0$) or valley structures ($S_{sk} < 0$) on the surface as compared to a Gaussian distribution ($S_{sk} = 0$). On the other hand, S_{ku} indicates the presence of inordinately high peaks/deep valleys ($S_{ku} > 3$) or lack thereof ($S_{ku} < 3$) making up the texture with respect to a Gaussian distribution ($S_{ku} = 3$). More details can be found in Ref. [95].

Samples in Fig. 5.2 were characterized in terms of the *R-parameters* using a RTP80 instrument (SM instruments) for roughness measurements. On the other hand, the *S-parameters* were computed by applying the standard definitions [95] to the three-dimensional profiles obtained by the optical scanner (where, in order to apply the previous definitions, an interpolated homogeneous mesh was adopted). All results are reported in Table 5.2. The tested sample surfaces show a peak distribution close to a Gaussian,

Table 5.2: Morphological statistical moments of tested samples (see Fig. 5.2): *R-parameters* (R_z and average R_a); *S-parameters* (maximum S_p, average S_a, root mean square S_q, kurtosis S_{ku} and skewness S_{sk}). For sample #4, left and right denote the corresponding sides of the fin. A_r is the roughness surface area and A is the reference planar area (See Ref. [3]).

Sample	R_z [μm]	R_a [μm]	S_p [μm]	S_a [μm]	S_q [μm]	S_{ku}	S_{sk}	A_r/A [%]
#1	79.1	15.8	41	12	15	3.01	0.31	1.1
#2	132.6	23.5	89	27	34	2.88	0.32	3.4
#3	237.8	43.0	118	36	45	2.78	0.32	6.9
#4 (left)	99.5	20.6	38	15	18	2.89	-0.21	-
#4 (right)	108.8	23.9	67	25	31	2.59	0.12	-

i.e. $S_{ku} \approx 3$ and $S_{sk} \approx 0$. More importantly, the flat surfaces reveal $S_a/S_p \approx 0.3$, while both sides of the fin have $S_a/S_p \approx 0.4$.

Table 5.3: Estimated emissivity of tested samples (see Fig. 5.2): Al refer to milled smooth samples ($R_a \approx 1$ μm) used as reference for computing heat transfer enhancement (See Ref. [3]).

Sample (see Fig. 5.2)	R_a [μm]	Real [°C]	Estimated [°C]	ϵ
Al	1	50.5	50.8	0.10
#1	16	55.5	55.6	0.35
#2	24	52.5	52.0	0.20
#3	43	43.9	43.0	0.39

It is well known that roughness can influence the surface emissivity and consequently radiative heat transfer. Since the present study focuses on convective heat transfer only, the contribution due to radiative heat transfer is removed by post-processing the experimental data. To this end, emissivity of surfaces is estimated through methodology described in 3.4.2. The results are reported in Table 5.3. As expected, these data clearly show that the rough samples present higher emissivity compared to the smooth one, although no evident relationship between the emissivity ϵ and the average roughness R_a was found. The higher emissivities of sample #1 and #3 might be explained by the multi-scale morphology, already pointed out by the FESEM analysis (see Fig. 5.6).

5.4. Experimental results

In this section, the experimental data and the measured heat transfer enhancements are reported for the tested samples. The experimental data about convective heat transfer (sample #1, #2 and #3 in Fig. 5.2) are reported in Fig. 5.7 in terms of the Nusselt number Nu_L and the Reynolds number Re_L defined in Chapter 3.

As pointed out in Chapter 3, Maddox & Mudawar [8] worked with a similar setup and already realized that the heating edge is the appropriate length (more than the channel hydraulic diameter) for scaling the experimental results. The latter evidence was later confirmed in Ref. [72]. For this reason, the experimental results are presented in terms of Nu_L and Re_L.

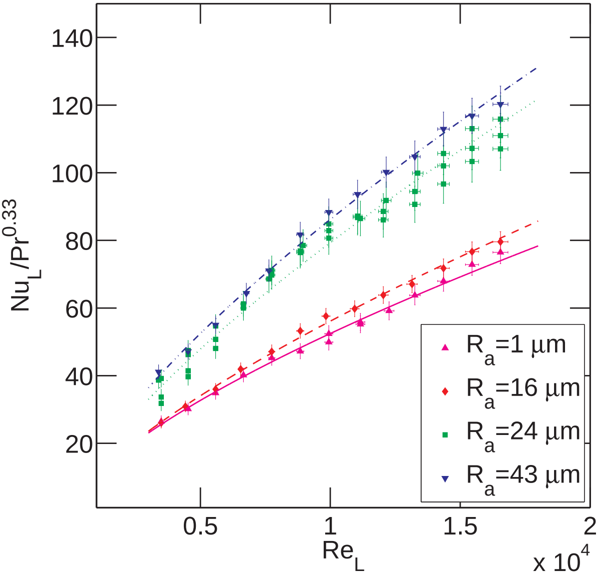

Figure 5.7: Experimental data about convective heat transfer (sample #1, #2 and #3, see Fig. 5.2). Smooth sample ($R_a \approx 1\ \mu m$) with the identical geometry was used as reference (See Ref. [3]).

Table 5.4: Experimental data about convective heat transfer for the flat reference, i.e. $R_a \approx 1\ \mu m$ (See Ref. [3]).

v $[m/s]$	Re_L	T_s $[K]$	T_a $[K]$	$\frac{V_h^2}{R_h}$ $[W]$	h $[W/m^2K]$	$\frac{Nu_L}{Pr^{1/3}}$	σ_h $[\%]$
3.4	3.49×10^3	335.0	302.4	0.1271	30.80	26.47	6.55
4.4	4.53×10^3	331.0	302.2	0.1271	35.10	30.17	5.97
5.4	5.58×10^3	327.2	302.2	0.1270	40.58	34.88	5.48
6.4	6.66×10^3	324.2	302.5	0.1270	46.75	40.17	5.14
7.4	7.75×10^3	321.2	301.9	0.1270	52.67	45.27	4.88
8.4	8.84×10^3	319.9	301.4	0.1270	54.95	47.23	4.79
9.4	9.94×10^3	318.2	300.7	0.1269	58.08	49.91	4.69
9.4	9.94×10^3	317.2	300.4	0.1275	60.96	52.39	4.65
10.5	1.12×10^4	316.4	300.4	0.1274	64.24	55.21	4.59
10.5	1.12×10^4	316.5	300.8	0.1273	65.00	55.86	4.58
11.5	1.23×10^4	315.3	300.4	0.1274	68.85	59.17	4.52
12.4	1.33×10^4	314.3	300.4	0.1273	74.19	63.76	4.46
13.4	1.44×10^4	313.3	300.3	0.1273	79.07	67.96	4.42
14.4	1.55×10^4	312.5	300.4	0.1273	84.75	72.83	4.38
15.4	1.65×10^4	312.0	300.5	0.1274	88.97	76.47	4.36

First of all, and more importantly, the rough surfaces made by direct metal laser sintering (DMLS) show an enhanced convective heat transfer. In particular, even though the average roughness R_a is not the best parameter to scale the heat transfer enhancement (see [3]), as expected the rougher the better. For a more quantitative analysis, the experimental data of the smoothest $R_a \approx 1\ \mu m$ reference surface are reported in Table 5.4 and those of the roughest $R_a = 43\ \mu m$ sample #3 are reported in Table 5.5. Defining the heat transfer enhancement E as the percentage increase of the rough surface for convective heat transfer with respect to the smoothest reference (assumed representative of milling processes), the sample #3 showed a peak enhancement of 73% and an average of 63%. This enhancement could not be simply explained in terms of effective area increase, as visible in Table 5.2.

Table 5.5: Experimental data about convective heat transfer for the sample #3, i.e. $R_a = 43\ \mu m$ (See Ref. [3]).

v $[m/s]$	Re_L	T_s $[K]$	T_a $[K]$	$\frac{V_h^2}{R_h}$ $[W]$	h $[W/m^2K]$	$\frac{Nu_L}{Pr^{1/3}}$	σ_h $[\%]$
3.3	3.39×10^3	324.2	303.5	0.1293	47.82	41.10	5.21
4.4	4.53×10^3	321.7	303.5	0.1293	54.87	47.16	4.96
5.4	5.58×10^3	319.2	303.5	0.1292	63.98	54.98	4.78
6.5	6.77×10^3	316.7	303.2	0.1290	74.90	64.37	4.65
7.3	7.64×10^3	315.0	302.8	0.1289	82.66	71.04	4.57
8.4	8.84×10^3	311.1	300.5	0.1280	95.04	81.68	4.52
9.4	9.94×10^3	310.4	300.6	0.1276	102.74	88.30	4.49
10.4	1.10×10^4	309.7	300.4	0.1274	108.93	93.62	4.48
11.4	1.22×10^4	309.1	300.5	0.1273	116.58	100.19	4.47
12.4	1.33×10^4	308.7	300.5	0.1268	121.85	104.72	4.47
13.4	1.44×10^4	308.1	300.4	0.1266	131.37	112.91	4.47
14.4	1.55×10^4	307.8	300.4	0.1264	135.91	116.80	4.47
15.4	1.65×10^4	307.6	300.4	0.1262	139.91	120.24	4.47

Table 5.6: Experimental data about convective heat transfer for the (single) finned reference ($R_a \approx 1\ \mu m$, smooth). For computing the average convective heat transfer coefficient and the Nusselt number, the total sample surface area was used (See Ref. [3]).

v $[m/s]$	Re_L	T_s $[K]$	T_a $[K]$	$\frac{V_h^2}{R_h}$ $[W]$	h $[W/m^2K]$	$\frac{Nu_L}{Pr^{1/3}}$	σ_h $[\%]$
3.4	3.54×10^3	315.2	297.9	0.3605	52.85	45.69	3.38
4.4	4.59×10^3	312.4	297.8	0.3601	63.05	54.52	3.02
5.4	5.66×10^3	310.1	297.5	0.3592	73.92	63.91	2.78
6.4	6.75×10^3	308.3	297.4	0.3591	84.92	73.42	2.64
7.4	7.85×10^3	307.0	297.3	0.3587	96.22	83.20	2.56
8.4	8.96×10^3	306.1	297.4	0.3582	106.49	92.07	2.53
9.4	1.01×10^4	305.7	297.6	0.3580	114.77	99.23	2.51
10.3	1.11×10^4	305.4	297.7	0.3576	120.77	104.41	2.50
11.2	1.21×10^4	305.0	297.7	0.3575	129.20	111.70	2.50
12.5	1.35×10^4	304.5	297.8	0.3570	139.55	120.65	2.50
13.4	1.45×10^4	304.3	297.7	0.3662	147.07	127.16	2.49
14.5	1.58×10^4	303.8	297.8	0.3656	159.28	137.72	2.51
15.4	1.68×10^4	303.6	297.7	0.3653	164.01	141.80	2.52

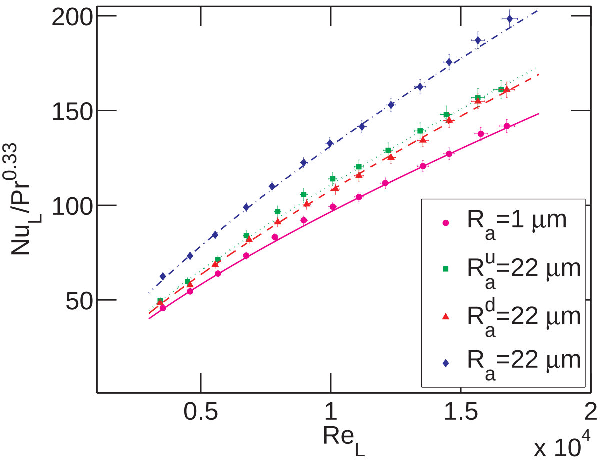

Figure 5.8: Experimental data about convective heat transfer of finned surfaces (sample #4 and #5, see Figs. 5.2 and 5.3). Smooth sample ($R_a \approx 1\ \mu m$) with the identical geometry was used as reference. R_a^u and R_a^d refer to sample #5 mounted with smooth half fin upstream and downstream, respectively (See Ref. [3]).

Table 5.7: Experimental data about convective heat transfer for the sample #4 ($R_a = 22\ \mu m$, maximum roughness). For computing the average convective heat transfer coefficient and the Nusselt number, the total sample surface area was used (See Ref. [3]).

v $[m/s]$	Re_L	T_s $[K]$	T_a $[K]$	$\frac{V_h^2}{R_h}$ $[W]$	h $[W/m^2K]$	$\frac{Nu_L}{Pr^{1/3}}$	σ_h $[\%]$
3.4	3.54×10^3	323.3	304.7	0.5229	72.26	62.48	2.89
4.4	4.59×10^3	319.3	303.3	0.5251	84.73	73.26	2.68
5.3	5.55×10^3	318.5	304.6	0.5195	97.58	84.37	2.58
6.4	6.75×10^3	315.2	303.2	0.5240	114.47	98.97	2.46
7.3	7.74×10^3	313.9	303.0	0.5233	127.22	109.99	2.42
8.4	8.96×10^3	313.8	304.0	0.5230	141.75	122.55	2.40
9.3	9.96×10^3	312.1	303.0	0.5247	153.52	132.73	2.38
10.4	1.12×10^4	311.6	303.0	0.5243	163.67	141.51	2.38
11.4	1.23×10^4	311.1	303.1	0.5238	176.88	152.93	2.38
12.4	1.34×10^4	311.4	304.0	0.5184	187.99	162.54	2.40
13.4	1.45×10^4	310.0	303.0	0.5235	203.07	175.58	2.41
14.4	1.57×10^4	309.6	303.1	0.5235	216.42	187.12	2.42
15.5	1.69×10^4	310.0	303.8	0.5235	229.52	198.44	2.45

In order to prove that the previous enhancements are not limited to flat surfaces only, some experimental tests were performed with (single) finned rough surfaces as well. The experimental data about convective heat transfer of finned surfaces (sample #4 and #5, see Figs. 5.2 and 5.3) are reported in Fig. 5.8, again in terms of the Nusselt number $Nu_L = h\,L/\lambda$ and Re_L, where h is the average convective heat transfer coefficient for finned surfaces. For a more quantitative analysis, the experimental data of the smoothest $R_a \approx 1\ \mu m$ finned reference surface are reported in Table 5.6 and those of the roughest $R_a = 22\ \mu m$ sample #4 are reported in Table 5.7. The heat transfer enhancement is confirmed in this case as well: The sample #4 showed a peak enhancement of 40 % and an average of 35 %. The enhancement is smaller than that the one observed in the case of flat surfaces (roughly half). First, It should be noticed that the roughness parameters for the finned sample #4 are smaller than those of the roughest flat sample #3, as reported in Table 5.2. Second, the fluid-dynamic conditions of the finned sample are completely different than those considered in the previous case: especially the fin tip yields the development of a new velocity boundary layer, superposing with the developing thermal boundary layer.

Further tests were designed to investigate the distribution of convective heat transfer on the latter sample. The fin area is 3/4 the total convective area. By assuming also that convective heat transfer coefficient on the horizontal surfaces of the smooth finned sample is equal to that on the smooth flat sample, it is possible to find out that convective heat transfer coefficient on fin sides is almost twice than that on horizontal surfaces. Hence it is important to investigate particularly the fin sides. The sample #5 (see Fig. 5.3) was made by milling horizontal surfaces and half of the fin sides of the previous sample #4. Consequently it was tested once by mounting it with smooth half fin upstream and once downstream (corresponding to R_a^u and R_a^d in Fig. 5.8). We found that smoothing (upstream) half of the fin sides the convective heat transfer is almost cut by half as well, confirming that most of the heat transfer is due to the fin. However, mounting the same sample #5 in downstream setup, the heat transfer reduction is even larger: This indicates that rough regions of the fin sides are more effective when farther from the leading edge of the boundary layer.

Finally, it is worth to discuss influence of roughness on friction factor, i.e. pressure drops. As discussed in Chapter 2, heat transfer devices performance criteria usually evaluates both thermal (heat transfer) and fluid-dynamics (pressure drops) performances, in order to guarantee the desired heat transfer rate with minimum operating cost (pumping power).

In this preliminary study, the sole heat transfer performances are measured. Nevertheless, it is possible to estimate friction factor of different flat rough surfaces through the Reynolds analogy (see [38] and Colburn's relation therein). That links the friction factor with the convective heat transfer, namely $Nu \propto f$. Under this assumption, it could be easily verified that aerothermal efficiency $\eta_A \propto (Nu/Nu_{ref})^{2/3}$, suggesting that rough surfaces experiencing enhanced heat transfer could guarantee enhanced aerothermal efficiency, too. The Reynolds analogy was derived under strong simplifying assumptions, which may not be applicable to any rough surface with any possible morphology. However this represents a first step, which requires further experimental verification.

5.5. Discussion

In this Chapter, the potential of the DMLS artificial roughness are experimentally investigate and optimized for convective heat transfer enhancement, in manufacturing flat and finned heat sinks. For rough flat surfaces, a peak of convective heat transfer enhancement of 73% (63% on average) is experienced, while, for rough (single) finned surfaces, a peak enhancement of 40% (35% on average) is found. Owing to a huge space of process parameters to be explored, the present work can be regarded as a first (but essential) step aiming at unveiling the great potential of DMLS in high efficiency heat transfer devices. Moreover, the presented results can be easily extended to other industrial sectors involving turbulent flows over walls. Please refer to [3] for additional information (e.g. theoretical model). Beyond the possibility to control surface roughness, a popular peculiarity of DMLS is the extreme flexibility in shapes of the fabricated parts. This feature is investigated in the following chapter to design high efficiency heat transfer devices.

6. Pitot tube based heat exchanger by DMLS

Peculiar features of DMLS are possibility to control surface roughness and capability of fabricating complex 3D structured. The first one has been investigated in Chapter 5; The following chapter focuses on the second. Here, a novel heat transfer device is conceived, designed and tested. Its *unusual morphology* is purposely designed to exploit ”Pitot tube” effect to generate secondary air flows aiming to enhance heat transfer. That device is extremely challenging (if not impossible) to be fabricated by traditional manufacturing techniques. Here it is easily fabricated in one step by DMLS, taking advance of the *extreme flexibility in shape* of manufactured parts. Higher heat transfer efficiency (i.e. convective heat flux) is reached, when compared with a standard reference device. More important, here the aim is to shed light additive manufacturing can lead a revolution in designing next generation heat transfer devices, when its versatility in shapes is fully exploited. Contents of this Chapter can be also found in [10].

6.1. Motivations

In this work, a novel heat transfer device based on *Pitot tube* effect is designed and manufactured by AM. Starting from a conventional plate fin heat sink (PFHS) considered as reference setup, that has been re-designed by introducing (i) hollow fins and, on the top of fin array, (ii) a pressure plug, which is in communication with (iii) several openings at the bottom of hollow fins. The basic idea is exploiting the Pitot tube effect for inducing secondary flows orthogonal to the main flow within fins. Consequently, heat transfer augmentation is achieved in the region where the velocity field is less vigorous (i.e. bottom of fins), by perturbing fluid-dynamics structures (i.e. boundary layers).

The Chapter is organized as follows: In Section 6.2, the heat exchanger design is described; In Section 6.3, the experimental characterization of the Pitot and reference heat exchanger is presented and examined; In Section 6.4, conclusions are drawn and perspectives are discussed.

6.2. Description of Pitot heat exchanger

Two heat exchangers have been manufactured, tested and compared in this Chapter, namely the proposed innovative heat exchanger and the corresponding reference one. The heat exchanger with Pitot tubes has been manufactured by DMLS, according to the process discussed in Section 5.2. Concerning process parameters, those have been already reported in Tab. 5.1 (refer to sample #1); Nevertheless, a more detailed description of them can be found in [9] (Tab. 1).

As depicted in Fig. 6.1, the Pitot heat exchanger is made of: (i) a 11x11x5 mm^3 parallelepiped; (ii) three 2x10x10 mm^3 hollow fins; (iii) a 11x10x6 mm^3 pressure plug (i.e. stagnation pressure tap). The parallelepiped is the bottom part of heat exchanger, whereas hollow fins are located on its upper side. Each fin is equally spaced from neighboring ones by 2 mm, and fin walls are 0.5 mm thick. Hence, the cavity volume is 1x9x10 mm^3 in each fin. Moreover, eight ellipsoidal openings (i.e. static pressure taps) have been placed at the bottom of each fin wall. The latter openings have dimensions 1.6x0.8 mm^2, and are arranged along three rows in a staggered configuration. Finally, the walls of the pressure plug are 1 mm tick laterally, while the remaining ones are 0.5 mm tick. The present heat exchanger has been manufactured in one step by DMLS, whereas bottom and lateral sides of the parallelepiped have been refined by milling, in order to properly insert it into the housing of the heat flux sensor described in Chapter 3.

A reference heat exchanger (i.e. PFHS) made of copper and manufactured by traditional milling has been also realized and tested for comparison purposes (Fig. 6.2). This conventional heat exchanger consists of a parallelepiped with three fins, with the same dimensions as in the Pitot heat exchanger; however, it differs from the Pitot heat exchanger as it does not have hollow fins, pressure plug and openings.

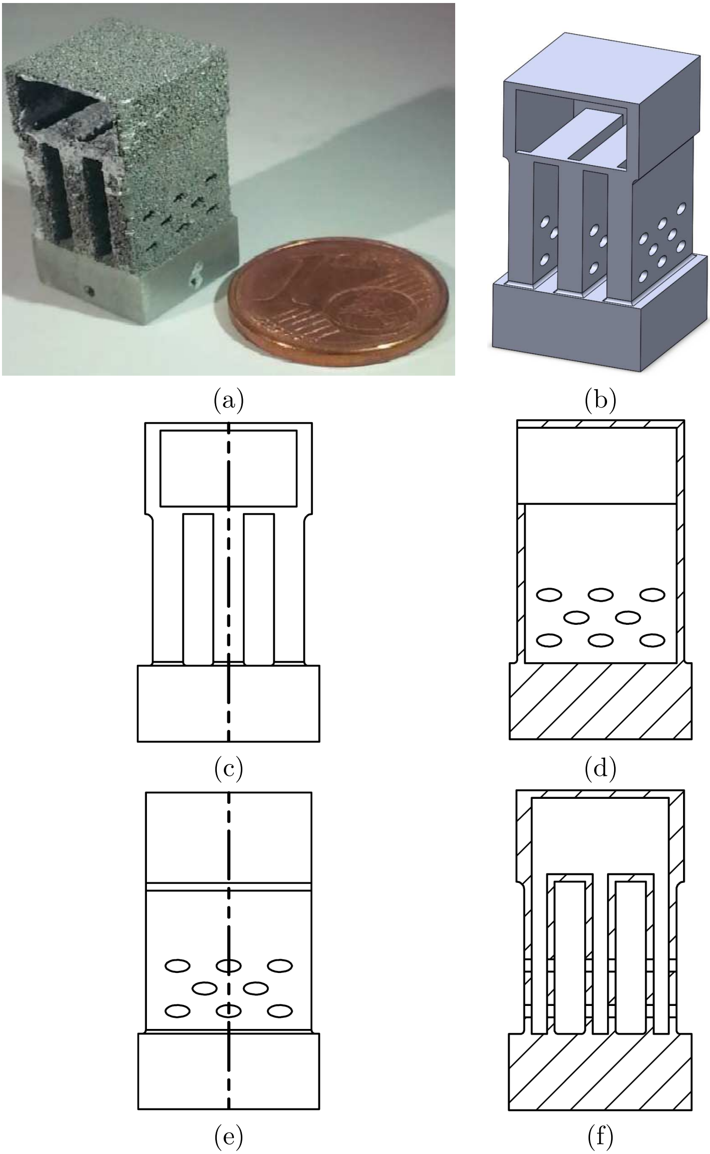

Figure 6.1: Heat exchanger with Pitot tubes embedded into the fins. (a) Picture of the prototype. Drawings of the prototype: (b) isometric view; (c, f) front views; (d, e) lateral views. Dashed lines in (c, e) define the cross-sections represented in (d, f), (See Ref. [10]).

Figure 6.2: Reference heat exchanger: plate fin heat sink - PFHS (See Ref. [10]).

6.3. Experimental characterization

The Pitot heat exchanger has been first tested in the *open configuration* (Fig. 6.1). For the sake of comparison, a *closed configuration* has been also tested, where a thin copper foil is glued at the bottom of the pressure plug, thus preventing the Pitot effect without affecting the overall shape of the heat exchanger. In fact, in the closed configuration, the foil is intended to stop the secondary flows at the bottom of fins, by inhibiting the fluid communication between pressure plug and fin openings. Testing the Pitot heat exchanger in both open and closed configuration is crucial to demonstrate the impact of the sole Pitot effect on heat transfer enhancement. In fact, the heat transfer enhancement due to secondary flows can be quantified by a direct comparison between the two configurations.

Experimental characterization has been carried on by the experimental rig described in Chapter 3. Convective thermal transmittance ($Tr = hA$) of heat exchangers is reported in Fig. 6.3 as function of the heated edge, average velocity based Reynolds number $Re_L = vL/\nu$, defined in Chapter 3.

It is worthwhile to note that the thermal transmittance of the Pitot heat exchanger with open configuration is higher than the closed one, which is in turn higher than the transmittance of the reference heat exchanger (i.e. PFHS). The superior performance of the open Pitot configuration as compared to the closed one demonstrates the heat transfer improvement by the secondary flows due to Pitot effect.

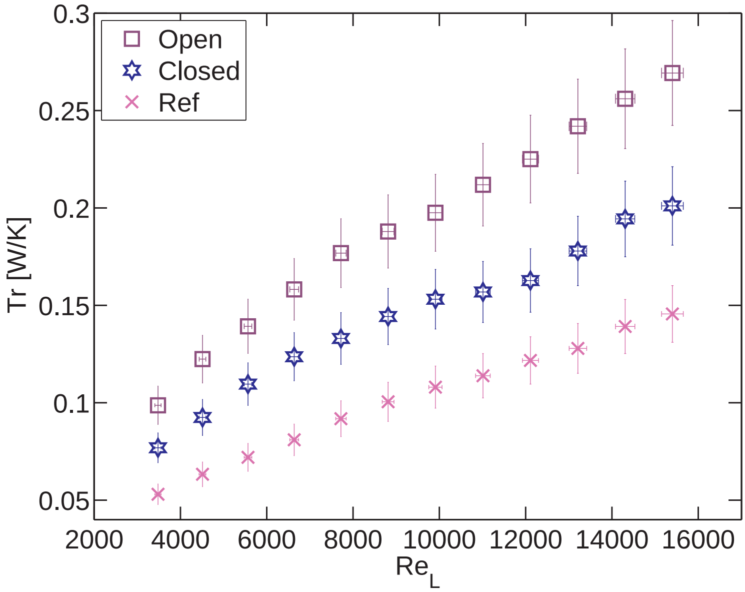

Figure 6.3: Convective thermal transmittance measured at different Reynolds numbers, for open Pitot (purple squares), closed Pitot (blue stars), and reference (pink crosses) heat exchangers (See Ref. [10]).

As expected, the pressure increase in the plug induces a secondary air flow circulation along the fin cavities, which exits from the openings at the bottom of fin array (Fig. 6.4a). Hence, the resulting convective heat transfer enhancement stems from two phenomena. First, the secondary air flow along the fin cavities cools down the inner fin walls, therefore an additional heat transfer area is involved in the heat transfer process. Second, air flows out of the openings orthogonally to the primary air flow and fin walls, thus interfering with the boundary layer and consequently enhancing the local heat transfer coefficient on the external fin walls.

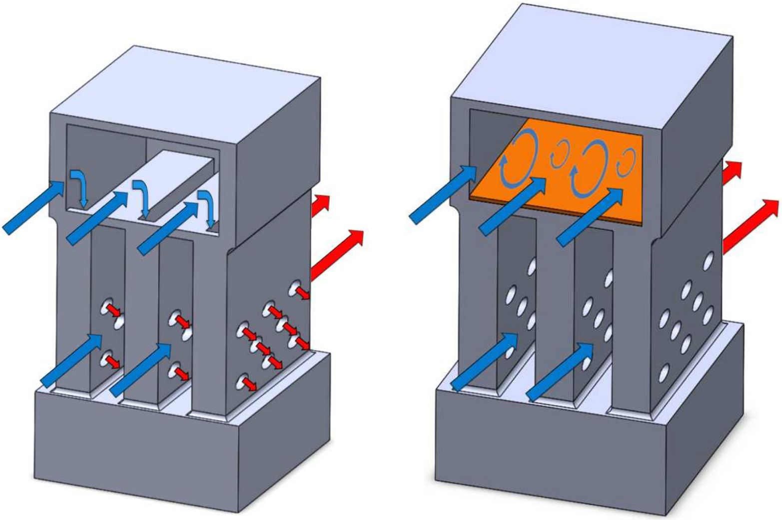

(a) (b)

Figure 6.4: Schematics of the air flow patterns in the Pitot heat exchanger with (a) open and (b) closed configurations (See Ref. [10]).

The Pitot heat exchanger with closed configuration shows thermal transmittances lower than the open one, because the fluid separation between pressure plug and fins cavities prevents the creation of secondary air flows. Hence, the kinetic energy of air entering the tap is dissipated by eddies (Fig. 6.4b). From preliminary results, the open Pitot configuration exhibits maximum and average Tr enhancements up to 38% and 32%, respectively, as compared to the closed ones.

Finally, It is worth to stress that the reference heat exchanger (i.e PFHS) has the lowest thermal transmittance among the tested configurations. This happens because the conventional heat exchanger benefits neither of the additional heat transfer area provided by the pressure plug (still present in the closed Pitot configuration), nor of the secondary flows induced by the Pitot tubes. Additionally, the innovative heat exchanger can also benefit of the artificial roughness readily available in parts manufactured by AM, as extensively reported in Chapter 5. In conclusion, the proposed heat exchanger based on the Pitot tube effect shows a maximum (average) enhancement in convective thermal transmittance of 95% (88%), as compared to the reference case. It is worth to emphasize that the proposed solution is a *passive* heat transfer augmentation technique, which does not need any additional energy source to work.

Concerning augmentation in pressure drops, it should be highlighted that, generally, behavior in terms of pressure drops of reference PFHS and Pitot heat exchanger are expected to be different. In fact, introduction of pressure plug implies augmentation of frontal cross section of heat exchanger. Moreover, secondary air flows from static tap placed on the fins, perturbing fluid-dynamic behaviour, can also affect overall pressure drops. As discussed in Sections 2.2 and 2.4, type of configuration (shrouded or unshrouded) plays a crucial role in determining the relevance of pressure drops induced by different heat exchangers (PFHS or Pitot). In the proposed work, both Pitot heat exchanger and PFHS are studied in unshrouded configurations. Moreover, frontal cross section of both the heat sinks is very small (about 2 cm^2) if compared with overall wind tunnel cross section, i.e. nearly 360 cm^2. Hence, as discussed in Section 2.2, eventual augmentation in pressure drop induced by Pitot heat exchanger do not lead to augmentation in overall circuit pressure drop. Moreover, excellent heat transfer performances of Pitot heat exchanger suggest that increase in pressure drops of Pitot heat exchanger are expected to be nearly negligible, since they do not lead to augmentation of bypass effect. Hence, Pitot heat exchanger is supposed to be a valid solution also from the point of view of pressure drops (i.e. operative costs), in the proposed unshrouded configuration.

6.4. Discussion

In this study, an unconventional heat exchanger is proposed, which implements an innovative *passive technique* for heat transfer augmentation. The proposed device has been designed and manufactured in a single step by exploiting the capabilities and flexibility of direct metal laser sintering (i.e. selective laser melting) in fabricating complex shaped components. Given a main flow field, the proposed *Pitot heat exchanger* induces secondary flows passing through the fin cavities and exiting orthogonally to the main flow. As a result, this solution significantly improves the convective heat transfer by concurrently (i) increasing heat transfer area and (ii) enhancing local heat transfer coefficient on fin walls, especially in regions where the flow field is less vigorous (fin bottom). The latter is achieved by inducing perturbation in fluid-dynamics structures (i.e. boundary layer breakage). The reported experiments show up to 95% increase in thermal performances of Pitot heat exchanger as compared to standard one. The sole Pitot tube effect is estimated to be responsible of 40% enhancement in thermal performances.

The preliminary results reported in here are intended to shed light on the new frontiers that additive manufacturing are opening in heat transfer engineering. In particular, the extreme geometrical flexibility offered by additive manufacturing may lead to new ways in conceiving and designing next-generation heat transfer devices.

7. Conclusions and perspectives

7.1. Survey and conclusions

In the present thesis, novel methods devoted to develop high heat transfer efficiency devices have been presented. These methods rely on both novel manufacturing techniques, belonging to the class of additive manufacturing (AM), and thermal and fluid-dynamics studies and optimization procedures.

As a first result, optimization of a traditional heat exchanger from a real application, i.e. million of units produced per year, is presented; That is manufactured by extrusion. A thermal fluid-dynamic model is experimentally validated (from an industrial experimental test rig) and used for optimization purposes. Results demonstrate there is room for efficiency optimization even in well established heat transfer devices configurations based on traditional manufacturing techniques [1].

Then, an experimental rig for ”in house” thermal characterization is designed. It guarantees high precision measurement of small convective heat fluxes (forced air) on enhanced solutions investigated hereinafter, namely micro-structured surfaces and small heat transfer devices. To deal with that challenge, an innovative convective heat flux sensor is developed. That exploits the concept of thermal guard to avoid any spurious perturbation between the flow field and investigated surfaces, while it allows to cancel out terms due to spreading conduction phenomenon. Results demonstrate remarkable accuracy in direct measurement of convective heat fluxes through this novel concept [4].

Relying on the proposed experimental rig, various methods for enhanced convective heat transfer are experimentally investigated. Firstly, regular patterns of micro-protrusions are studied. Effect of fluid-dynamics and geometrical length on heat transfer performances are discussed. More important, they have been applied to develop an optimization procedure tailored to deal with AM techniques. Results from both experimental investigation and optimization procedure suggest the existence of an optimal value of protrusion height, that maximize performance-to-cost ratio for patterns made by AM [7].

Then, surface roughness of components built by DMLS has been investigated as an augmentation heat transfer technique. Surface roughness is controlled varying DMLS process parameters and its effect on convective heat transfer is measured. The results demonstrate a remarkable enhancement in convective heat transfer due to DMLS artificial roughness, in the investigated configurations [3]. That preliminary study unveils the potential of AM artificial roughness as an heat transfer enhancement techniques. It has been considered, by academic and industrial institutions, as an important step towards development of next generation gas turbine components [96–98] and electronic cooling devices [99].

Finally, extreme flexibility in shape of parts built by DMLS is exploited to design and fabricate in one step an unconventional heat transfer device, called Pitot heat exchanger. Enhanced heat transfer efficiency is achieved, with regard to standard heat exchangers. Nevertheless, the most important achievement has been to highlight unusual morphologies allowed by AM can pave the way to revolutionary changes in conceiving and designing heat transfer components [10].

7.2. Outlook and perspectives

Additive manufacturing, also called 3D printing, is a manufacturing technique born nearly 30 years ago. In last decades AM evolved, in order to process different materials, increase quality of fabricated parts and reduce costs. As a result, nowadays it allows to fabricate complex 3D parts in metallic alloys with low bulk porosity, hence guaranteeing high thermal conductivity and remarkable mechanical properties. Moreover, it has been demonstrated to be a cost effective choice with regard to traditional manufacturing technique, in producing small batch (hundreds per years) of parts. AM is currently used by aerospace companies to produce components such as gas turbine blades. High efficiency heat transfer is crucial in these components [100].

That encouraging growth could open the possibility AM will be used for mass production of large amount of items, in the future. Probably, AM will integrates traditional manufacturing techniques [101]. Even, has been argued AM could pave the way to a third industrial revolution [102].

Key of present and future development of AM lays in the so called ”think additive” attitude. It means focus on peculiar features of AM, not allowed by traditional techniques, and exploit them. They are flexibility in shapes of built parts, capability of built in one piece complex systems fabricated so far connecting together many different parts, possibility to reduce material used to fabricate them (hence reducing weight and costs), possibility to tune surface roughness. ”Think additive” advice has been already receipt in field of structural mechanics where peculiarities of AM are used to develop more efficient, reliable and lighter devices. See as example structural supports depicted in [103] and fuel nozzles for gas turbines described in [104, 105].

On the other hand, ”think additive” attitude has not been receipt yet in the field of thermal system design. Very few examples of such a spirit in developing heat transfer devices can be found, so far (e.g. [99]). Nevertheless, Additive manufacturing is used nowadays in application where thermal management is a crucial issue. This work is expected to encourage scientific and industrial community toward a shift in approaching design of new technological solutions for heat transfer based on AM.

8. Conflicts of Interest

The author declares no conflict of interest. Permissions to reproduce contents from [3, 4, 7, 10] have been granted by the publisher through Copyright Clearance Center service.

9. Curriculum Vitae

Luigi Ventola

Personal Data

Date of birth:	9th April 1987
Sex:	male
Place of birth:	Avellino (Italy)
Citizen of:	Italy

Education

- **PhD thesis (2013-2016)**
  - Title: High-efficiency heat transfer devices by innovative manufacturing techniques
  - Tutors: Prof. Dr. P. Asinari and Dr. E. Chiavazzo
  - Department: Energy department
  - Place: Polytechnic of Turin (Italy)
- **Master degree in Energy and Nuclear Engineering (2008-2011)**
  - Title: Computational fluid dynamics and population balance based modeling of fluidized systems for gasification.
  - Tutor: Prof. Dr. D.L. Marchisio
  - Department: Chemical engineering

  - Place: Polytechnic of Turin (Italy)

Work experience

- **Research fellow (2011-2012)**
  - Place: Polytechnic of Turin (Italy)
- **Ventilation system analyst (2011)**
  - Place: Cantene S.r.l., Turin (Italy)
- **Production engineer (2011)**
  - Place: Ahlstrom Turin S.p.A., Mathi, Turin (Italy)

Publications

- L. Ventola, G. Curcuruto, M. Fasano, S. Fotia, V. Pugliese, D., E. Chiavazzo, and P. Asinari. Unshrouded plate fin heat sinks for electronics cooling: Validation of a comprehensive thermal model and cost optimization in semi-active configuration. *under review for publication on MDPI energies*, 2016.

- M. Fasano, L. Ventola, F. Calignano, D. Manfredi, E. P. Ambrosio, E. Chiavazzo, and P. Asinari. Passive heat transfer enhancement by 3D printed Pitot tube based heat sink. *International Communications in Heat and Mass Transfer*, 74:36 – 39, 2016.

- M. I. Shahzad, M. Giorcelli, L. Ventola, D. Perrone, N. Shahzad, E. Chiavazzo, P. Asinari, M. Cocuzza, and A. Tagliaferro. Convective heat transfer enhancement for electronic device applications using patterned MWCNTs structures. *Heat Transfer Engineering*, 37(9):783–790, 2016.

- L. Ventola, M. Dialameh, M. Fasano, E. Chiavazzo, and P. Asinari. Convective heat transfer enhancement by diamond shaped micro-protruded patterns for heat sinks: Thermal fluid dynamic investigation and novel optimization methodology. *Applied Thermal Engineering*, 93:1254–1263, 2016.

- E. Chiavazzo, M. Isaia, S. Mammola, E. Lepore, L. Ventola, P. Asinari, and N.M. Pugno. Cave spiders choose optimal environmental factors with respect to the generated entropy when laying their cocoon. *Scientific Reports*, 5(7611):1–8, 2015.
- M. Sangermano, L. Calvara, E. Chiavazzo, L. Ventola, P. Asinari, V. Mittal, R. Rizzoli, L. Ortolani, and V. Morandi. Enhancement of electrical and thermal conductivity of Su-8 photocrosslinked coatings containing graphene. *Progress in Organic Coatings*, 88:143-146, 2015.
- L. Ventola, F. Robotti, M. Dialameh, F. Calignano, D. Manfredi, E. Chiavazzo, and P. Asinari. Rough surfaces with enhanced heat transfer for electronics cooling by direct metal laser sintering. *International Journal of Heat and Mass Transfer*, 75:58–74, 2014.
- E. Chiavazzo, L. Ventola, F. Calignano, D. Manfredi, and P. Asinari. A sensor for direct measurement of small convective heat fluxes: Validation and application to micro-structured surfaces. *Experimental Thermal and Fluid Science*, 55:42–53, 2014.
- L. Ventola, L. Scaltrito, S. Ferrero, G. Maccioni, E. Chiavazzo, and P. Asinari. Micro-structured rough surfaces by laser etching for heat transfer enhancement on flush mounted heat sinks. *Journal of Physics: Conference Series*, 525(1), 2014.
- L. Ventola, E. Chiavazzo, F. Calignano, D. Manfredi, and P. Asinari. Heat transfer enhancement by finned heat sinks with micro-structured roughness. *Journal of Physics: Conference Series*, 494(1), 2014.

Proceedings

- E. Chiavazzo, M. Isaia, S. Mammola, E. Lepore, L. Ventola, P. Asinari, and N.M. Pugno. Do spiders know thermodynamics? *The Constructal Law and the Second Law conference*, Parma (Italy), May 2015.
- L. Ventola, F. Calignano, D. Manfredi, E. Chiavazzo, and P. Asinari. Micro finned surfaces for heat transfer enhancement. *3rd-National Congress of Italian Mechanics Coordination* , Napoli (Italy), June 2016.

Bibliography

[1] L. Ventola, G. Curcuruto, M. Fasano, S. Fotia, V. Pugliese, D., E. Chiavazzo, and P. Asinari. Unshrouded plate fin heat sinks for electronics cooling: Validation of a comprehensive thermal model and cost optimization in semi-active configuration. *under review for publication on MDPI energies*, 2016.

[2] M. I. Shahzad, M. Giorcelli, L. Ventola, D. Perrone, N. Shahzad, E. Chiavazzo, P. Asinari, M. Cocuzza, and A. Tagliaferro. Convective heat transfer enhancement for electronic device applications using patterned MWCNTs structures. *Heat Transfer Engineering*, 37(9):783–790, 2016.

[3] L. Ventola, F. Robotti, M. Dialameh, F. Calignano, D. Manfredi, E. Chiavazzo, and P. Asinari. Rough surfaces with enhanced heat transfer for electronics cooling by direct metal laser sintering. *International Journal of Heat and Mass Transfer*, 75:58–74, 2014.

[4] E. Chiavazzo, L. Ventola, F. Calignano, D. Manfredi, and P. Asinari. A sensor for direct measurement of small convective heat fluxes: Validation and application to micro-structured surfaces. *Experimental Thermal and Fluid Science*, 55:42–53, 2014.

[5] L. Ventola, L. Scaltrito, S. Ferrero, G. Maccioni, E. Chiavazzo, and P. Asinari. Micro-structured rough surfaces by laser etching for heat transfer enhancement on flush mounted heat sinks. *Journal of Physics: Conference Series*, 525(1), 2014.

[6] L. Ventola, E. Chiavazzo, F. Calignano, D. Manfredi, and P. Asinari. Heat transfer enhancement by finned heat sinks with micro-structured roughness. *Journal of Physics: Conference Series*, 494(1), 2014.

[7] L. Ventola, M. Dialameh, M. Fasano, E. Chiavazzo, and P. Asinari. Convective heat transfer enhancement by diamond shaped micro-protruded patterns for heat sinks: Thermal fluid dynamic investi-

gation and novel optimization methodology. *Applied Thermal Engineering*, 93:1254–1263, 2016.

[8] D.E. Maddox and I. Mudawar. Single- and two-phase convective heat transfer from smooth and enhanced microelectronic heat sources in a rectangular channel. *Journal of Heat Transfer*, 111:1045–1052, 1989.

[9] F. Calignano, D. Manfredi, E. P. Ambrosio, L. Iuliano, and P. Fino. Influence of process parameters on surface roughness of aluminum parts produced by dmls. *The International Journal of Advanced Manufacturing Technology*, 67(9):2743–2751, 2013.

[10] M. Fasano, L. Ventola, F. Calignano, D. Manfredi, E. P. Ambrosio, E. Chiavazzo, and P. Asinari. Passive heat transfer enhancement by 3D printed Pitot tube based heat sink. *International Communications in Heat and Mass Transfer*, 74:36 – 39, 2016.

[11] R.L. Mason, R.F. Gunst, and J.L. Hess. *Statistical Design and Analysis of Experiments: With Applications to Engineering and Science.* John Wiley, 2003.

[12] EOS datasheet, EOS aluminium AlSi10Mg for EOSINT M 270, 2011.

[13] S.V. Garimella, A.S. Fleischer, J.Y. Murthy, A. Keshavarzi, R. Prasher, C. Patel, S.H. Bhavnani, R. Venkatasubramanian, R. Mahajan, Y. Joshi, B. Sammakia, B.A. Myers, L. Chorosinski, M. Baelmans, P. Sathyamurthy, and P.E. Raad. Thermal challenges in next-generation electronic systems. *IEEE Transactions on Components and Packaging Technologies*, 31(4):801–815, 2008.

[14] A. Joardar and A.M. Jacobi. Heat transfer enhancement by winglet-type vortex generator arrays in compact plain-fin-and-tube heat exchangers. *International Journal of Refrigeration*, 31(1):87 – 97, 2008.

[15] S. Gupta, A. Chaube, and P. Verma. Review on heat transfer augmentation techniques: Application in gas turbine blade internal cooling. *Journal of Engineering Science and Technology Review*, 5(1):57–62, 2012.

[16] C. Gillot, A. Bricard, and C. Schaeffer. Single- and two-phase heat exchangers for power electronic components. *International Journal of Thermal Sciences*, 39:826–832, 2000.

[17] F.P. Incropera. Liquid immersion cooling of electronic components. *Bulletin of the International Centre for Heat and Mass Transfer*, 3:29–64, 1989.

[18] H.Y. Zhang, D. Pinjala, and P.-S. Teo. Thermal management of high power dissipation electronic packages: From air cooling to liquid cooling. pages 620–625, 2003.

[19] X. Chen, H. Ye, X. Fan, T. Ren, and G. Zhang. A review of small heat pipes for electronics. *Applied Thermal Engineering*, 96:1–17, 2016.

[20] J.B. Campbell, L.M. Tolbert, C.W. Ayers, B. Ozpineci, and K.T. Lowe. Two-phase cooling method using the r134a refrigerant to cool power electronic devices. *IEEE Transactions on Industry Applications*, 43(3):648–656, 2007.

[21] R. Remsburg. *Advanced Thermal Design of Electronic Equipment.* Chapman & Hall, New York, 1998.

[22] W. M. Kays and A. L. London. *Compact Heat Exchangers.* Krieger Publishing Company, 1984.

[23] A.M.Y. Razak. *Industrial Gas Turbines.* Woodhead Publishing, 2007.

[24] S. Kakac, A. E. Bergles, F. Mayinger, and H. Yuncu. *Heat Transfer Enhancement of Heat Exchangers.* Kluwer, Dordrecht, The Netherlands, 1999.

[25] P.M. Ligrani, M.M. Oliveira, and T. Blaskovich. Comparison of heat transfer augmentation techniques. *AIAA Journal*, 41(3):337–362, 2003.

[26] J.R. Culham and Y.S. Muzychka. Optimization of plate fin heat sinks using entropy generation minimization. *Components and Packaging Technologies, IEEE Transactions on*, 24(2):159–165, 2001.

[27] C. J. Shih and G. C. Liu. Optimal design methodology of plate-fin heat sinks for electronic cooling using entropy generation strategy. *IEEE Transactions on Components and Packaging Technologies*, 27(3):551–559, Sept 2004.

[28] W. A. Khan, J.R. Culham, and M.M. Yovanovich. The role of fin geometry in heat sink performance. *ASME Journal of Electronic Packaging*, 128(4):324–330, 2006.

[29] S.W. Chang, T.L. Yang, C.C. Huang, and K.F. Chiang. Endwall heat transfer and pressure drop in rectangular channels with attached and

detached circular pin-fin array. *International Journal of Heat and Mass Transfer*, 51(21-22):5247 – 5259, 2008.

[30] Yue-Tzu Yang and Huan-Sen Peng. Numerical study of pin-fin heat sink with un-uniform fin height design. *International Journal of Heat and Mass Transfer*, 51(19-20):4788 – 4796, 2008.

[31] P.M. Ligrani, G.I. Mahmood, J.L. Harrison, C.M. Clayton, and D.L. Nelson. Flow structure and local nusselt number variations in a channel with dimples and protrusions on opposite walls. *International Journal of Heat and Mass Transfer*, 44(23):4413 – 4425, 2001.

[32] M.A. Elyyan, A. Rozati, and D.K. Tafti. Investigation of dimpled fins for heat transfer enhancement in compact heat exchangers. *International Journal of Heat and Mass Transfer*, 51(11-12):2950 – 2966, 2008.

[33] Y. Chen, Y.T. Chew, and B.C. Khoo. Enhancement of heat transfer in turbulent channel flow over dimpled surface. *International Journal of Heat and Mass Transfer*, 55(25-26):8100 – 8121, 2012.

[34] S.V. Garimella and P.A. Eibeck. Heat transfer characteristics of an array of protruding elements in single phase forced convection. *International Journal of Heat and Mass Transfer*, 33(12):2659 – 2669, 1990.

[35] G.I. Mahmood, M.Z. Sabbagh, and P.M. Ligrani. Heat transfer in a channel with dimples and protrusions on opposite walls. *Journal of Thermophysics and Heat Transfer*, 15(3):275–283, 2001.

[36] S. Mancin, C. Zilio, A. Diani, and L. Rossetto. Air forced convection through metal foams: Experimental results and modeling. *International Journal of Heat and Mass Transfer*, 62(1):112–123, 2013.

[37] S.W. Chang, T.M. Liou, and M.H. Lu. Heat transfer of rectangular narrow channel with two opposite scale roughened walls. *International Journal of Heat and Mass Transfer*, 48(19-20):3921–3931, 2005.

[38] A. Bejan and A.D. Kraus. *Heat Transfer Handbook*. John Wiley, Hoboken, 2003.

[39] R. Neugebauer, B. Muller, M. Gebauer, and T. Toppel. Additive manufacturing boosts efficiency of heat transfer components. *Assembly Automation*, 31(4):344–347, 2011.

[40] A. Diani, S. Mancin, C. Zilio, and L. Rossetto. An assessment on air forced convection on extended surfaces: Experimental results and numerical modeling. *International Journal of Thermal Sciences*, 67:120–134, 2013.

[41] R.M. Shaalan, A.M. Saleh, O. Mesalhy, and L.M. Elsayed. Thermo/fluid performance of a shielded heat sink. *International Journal of Thermal Sciences*, 60:171–181, 2012.

[42] S. Lee. Optimum design and selection of heat sinks. *IEEE Transactions on Components, Packaging, and manufacturing Technology*, 18:812–817, 1995.

[43] A. Chen. Aluminum extrusion design and the role it plays in high performance cooling solutions for power electronics. *Applied Power Electronics Conference*, 2014.

[44] E.M. Sparrow, B.R. Baliga, and S.V. Patankar. Forced convection heat transfer from a shrouded fin array with and without tip clearance. *Journal of Heat Transfer*, 100(4):572–579, 1978.

[45] K.S. Lau and R.L. Mahajan. Effects of tip clearance and fin density on the performance of heat sinks for vlsi packages. *IEEE Transactions on Components, Hybrids, and Manufacturing Technology*, 12:4:757–765, 1989.

[46] R.S. Lee, H.C. Huang, and W.Y. Chen. A thermal characteristic study of extruded-type heat sinks in considering air flow bypass phenomenon. *Semiconductor Thermal and Temperature Measurement Symposium, 1990. SEMI-THERM VI, Proceedings., Sixth Annual IEEE*, pages 95–102, 1990.

[47] H. Iwasaki, T. Sasaki, and M. Ishizuka. Cooling performance of plate fins for multichip modules. In *Thermal Phenomena in Electronic Systems, 1994. I-THERM IV. Concurrent Engineering and Thermal Phenomena., InterSociety Conference on*, pages 144–147. IEEE, 1994.

[48] R.A. Wirtz, W. Chen, and R. Zhou. Effect of flow bypass on the performance of longitudinal fin heat sinks. *Journal of Electronic Packaging*, 116(3):206–211, 1994.

[49] H. Jousson and B. Palm. Thermal and hydraulic behavior of plate fin and strip fin heat sinks under varying bypass conditions. *Components and Packaging Technologies, IEEE Transactions on*, 23(1):47–54, 2000.

[50] M. Ishizuka, Y. Yokono, and D. Biswas. Experimental study on the performance of a compact heat sink for LSI packages. *Proceedings of the Institution of Mechanical Engineers, Part A: Journal of Power and Energy*, 214(5):523–530, 2000.

[51] A. Bejan and A.M. Morega. Optimal arrays of pin fins and plate fins in laminar forced convection. *Journal of Heat Transfer*, 115(1):75–81, 1993.

[52] M. Iyengar and A. Bar-Cohen. Least-energy optimization of forced convection plate-fin heat sinks. *Components and Packaging Technologies, IEEE Transactions on*, 26(1):62–70, 2003.

[53] A. Bar-Cohen and M. Iyengar. Least-energy optimization of air-cooled heat sinks for sustainable development. *Components and Packaging Technologies, IEEE Transactions on*, 26(1):16–25, 2003.

[54] G. Maranzana, I. Perry, D. Maillet, and S. Raël. Design optimization of a spreader heat sink for power electronics. *International Journal of Thermal Sciences*, 43:21–29, 2004.

[55] A. Bar-Cohen, R. Bahadur, and M. Iyengar. Least-energy optimization of air-cooled heat sinks for sustainability-theory, geometry and material selection. *Energy*, 31(5):579–619, 2006.

[56] P. Ahmadi, H. Hajabdollahi, and I. Dincer. Cost and entropy generation minimization of a cross-flow plate fin heat exchanger using multi-objective genetic algorithm. *Journal of Heat Transfer*, 133(2), 2011.

[57] M. Lindstedt, K. Lampio, and R. Karvinen. Optimal shapes of straight fins and finned heat sinks. *Journal of Heat Transfer*, 137(6), 2015.

[58] J.R. Culham, Khan W.A., M.M. Yovanovich, and Y.S. Muzychka. The influence of material properties and spreading resistance in the thermal design of plate fin heat sinks. *Journal of Electronic Packaging*, 129:1:76–81, 2007.

[59] C.T. Chen and H.I. Chen. Multi-objective optimization design of plate-fin heat sinks using a direction-based genetic algorithm. *Journal of the Taiwan Institute of Chemical Engineers*, 44(2):257 – 265, 2013.

[60] R. Hossain, J.R. Culham, and M.M. Yovanovich. Influence of bypass on flow through plate fin heat sinks. *23rd IEEE Semiconductor Thermal Measurement and Management Symposium*, 4160915:220–227, 2007.

[61] F.M. White. *Fluid Mechanics*. McGraw-Hill, New York, 1987.

[62] Y.S. Muzychka and M.M. Yovanovich. Modeling friction factors in non-circular ducts for developing laminar flow. *Proceeding in 2nd AIAA Theoretical Fluid Mechanical Meeting*, 1998.

[63] P. Teertstra, M.M. Yovanovich, J.R. Culham, and T. Lemczyk. Analytical forced convection modeling of plate fin heat sinks. *15th IEEE Semiconductor Thermal Measurement and Management Symposium*, pages 34–41, 1999.

[64] E. Chiavazzo and P. Asinari. Reconstruction and modeling of 3D percolation networks of carbon fillers in a polymer matrix. *International Journal of Thermal Sciences*, 49:2272–2281, 2010.

[65] S. Lee, S. Song, V. Au, and K. Moran. Constriction-spreading resistance model for electronic packaging. *ASME/JSME Thermal Engineering Conference*, 4, 1995.

[66] R.C. Baker. *Flow Measurement Handbook: Industrial Designs, Operating Principles, Performance, and Applications*. Cambridge University Press, 2005.

[67] G. Fang, J. Zhou, and J. Duszczyk. Extrusion of 7075 aluminium alloy through double-pocket dies to manufacture a complex profile. *Journal of Materials Processing Technology*, 209:3050–3059, 2009.

[68] Private communication with DENSO Thermal Systems, Poirino (Turin), Italy, 2015.

[69] I.V. Shevchuk, S.C. Jenkins, B. Weigand, J. Von Wolfersdorf, S.O. Neumann, and M. Schnieder. Validation and analysis of numerical results for a varying aspect ratio two-pass internal cooling channel. *Journal of Heat Transfer*, 133(5), 2011.

[70] B. Yuan and M. Gallagher. A hybrid approach to parameter tuning in genetic algorithms. *IEEE Congress on Evolutionary Computation*, 2:1096–1103, 2005.

[71] F.P. Incropera, J.S. Kerby, D.F. Moffatt, and S. Ramadhyani. Convection heat transfer from discrete heat sources in a rectangular channel. *International Journal of Heat and Mass Transfer*, 29:1051–1058, 1986.

[72] C.P. Tso, G.P. Xu, and K.W. Tou. An experimental study on forced convection heat transfer from flush-mounted discrete heat sources. *Journal of Heat Transfer*, 121:326–332, 1999.

[73] H. Bhowmik and K.W. Tou. Experimental study of transient natural convection heat transfer from simulated electronic chips. *Experimental Thermal and Fluid Science*, 29:485–492, 2004.

[74] T. Astarita, G. Cardone, G.M. Carlomagno, and C. Meola. A survey on infrared thermography for convective heat transfer measurements. *Optics & Laser Technology*, 32:593–610, 2000.

[75] M. Mori, L. Novak, and M. Sekavcnik. Measurements on rotating blades using ir thermography. *Experimental Thermal and Fluid Science*, 32:387–396, 2007.

[76] H. Ay, J.Y. Jang, and J.N. Yeh. Local heat transfer measurements of plate finned-tube heat exchangers by infrared thermography. *International Journal of Heat and Mass Transfer*, 45:4069–4078, 2002.

[77] S. Montelpare and R. Ricci. An experimental method for evaluating the heat transfer coefficient of liquid-cooled short pin fins using infrared thermography. *Experimental Thermal and Fluid Science*, 28:815–824, 2004.

[78] T.S. O'Donovan, T. Persoons, and D.B. Murray. High-resolution hot-film measurement of surface heat flux to an impinging jet. *Meas. Sci. Technol.*, 22:105402, 2011.

[79] H. Mocikat and H. Herwig. Heat Transfer Measurements with Surface Mounted Foil-Sensors in an Active Mode: A Comprehensive Review and a New Design. *Sensors*, 9:3011–3032, 2009.

[80] M. Schwerter, T. Beutel, L.M. Schädel, S. Büttgenbach, and A. Dietzel. Flexible hot-film anemometer arrays on curved structures for active flow control on airplane wings. *Microsystem Technologies*, 2014.

[81] EKO Instruments. EKO heat flow sensors. http://eko-eu.com/.

[82] A. Kalani and S.G. Kandlikar. Pool boiling of FC-87 over microchannel surfaces at atmospheric pressure. *Proceedings of the ASME 2012 10th International Mechanical Engineering Congress & Exposition*, 2012.

[83] H. Czichos, T. Saito, and L. Smith. *Handbook of Materials Measurement Methods*. Springer, 2006.

[84] D.G. Holmberg, C.A. Womeldorf, and W.L. Grosshandler. Design and uncertainty analysis of a second-generation convective heat flux calibration facility. *Proceedings of American Society of Mechanical Engineers (ASME) Heat Transfer Division*, 2001.

[85] S.J. Kline and F.A. McClintock. Describing uncertainties single-sample experiments. *Mechanical Engineering*, pages 3–8, 1953.

[86] C.W. Leung, H.J. Kang, and S.D. Probert. Horizontal simulated printed-circuit board assembly in fully-developed laminar-flow convection. *Applied Energy*, 56(1):71 – 91, 1997.

[87] C. S. B. Grimmond and T. R. Oke. Aerodynamic properties of urban areas derived from analysis of surface form. *Journal of Applied Meteorology*, 38(9):1262–1292, 1999.

[88] S.B. Pope. *Turbulent flows*. Cambridge university press, 2000.

[89] H. Schlichting and K. Gersten. *Boundary-Layer Theory*. Springer, 2000.

[90] J.P. Kruth, G. Levy, F. Klocke, and T.H.C. Childs. Consolidation phenomena in laser and powder-bed based layered manufacturing. *CIRP Annals - Manufacturing Technology*, 56(2):730 – 759, 2007.

[91] M. Wong, I. Owen, C.J. Sutcliffe, and A. Puri. Convective heat transfer and pressure losses across novel heat sinks fabricated by selective laser melting. *International Journal of Heat and Mass Transfer*, 52(1 - 2):281 – 288, 2009.

[92] A. Simchi. Direct laser sintering of metal powders: mechanism, kinetics, and microstructural features. *Materials Science and Engineering: A*, 428:148–158, 2006.

[93] D. Manfredi, F. Calignano, M. Krishnan, R. Canali, E.P. Ambrosio, and E. Atzeni. From Powders to Dense Metal Parts: Characterization of a Commercial AlSiMg Alloy Processed through Direct Metal Laser Sintering. *Materials*, 6:856–869, 2013.

[94] ISO 4287: Geometrical product specification (GPS) - surface texture: Profile method - terms, definitions and surface texture parameters (R-parameters).

[95] ISO 25178: Geometrical product specification (GPS) - surface texture: areal (S-parameters).

[96] J.C. Snyder, C.K. Stimpson, K.A. Thole, and D.J. Mongillo. Build direction effects on microchannel tolerance and surface roughness. *Journal of Mechanical Design, Transactions of the ASME*, 137(11), 2015.

[97] J.C. Snyder, C.K. Stimpson, K.A. Thole, and D. Mongillo. Build direction effects on additively manufactured channels. *Journal of Turbomachinery*, 138(5), 2016.

[98] C.K. Stimpson, J.C. Snyder, K.A. Thole, and D. Mongillo. Roughness effects on flow and heat transfer for additively manufactured channels. *Journal of Turbomachinery*, 138(5), 2016.

[99] E.M. Dede, S.N. Joshi, and F. Zhou. Topology optimization, additive layer manufacturing, and experimental testing of an air-cooled heat sink. *Journal of Mechanical Design, Transactions of the ASME*, 137(11), 2015.

[100] N.M. Yusop, A.H. Ali, and M.Z. Abdullah. Conjugate film cooling of a new multi-layer convex surface of turbine blades. *International Communications in Heat and Mass Transfer*, 45:86–94, 2013.

[101] 3D printing scales up. The Economist, 2013.

[102] The third industrial revolution. The Economist, 2012.

[103] 3D printing wonderful widgets. The Economist, 2015.

[104] Heavy metal. The Economist, 2014.

[105] The FAA cleared the first 3D printed part to fly in a commercial jet engine from GE. available from: http://www.gereports.com/post/116402870270/the-faa-cleared-the-first-3d-printed-part-to-fly/ (accessed 03.04.16). GE Reports, 2015.

[106] ANSYS FLUENT. 12.0/12.1 documentation, ansys, inc.

[107] Wakefield-vette, BGA thermal solutions matrix. (2015). available from: http://www.wakefield-vette.com/resource-center/downloads/brochures/intergrated-heatsink-wakefield.pdf (accessed 18.03.16).

Appendix

A. Computational fluid dynamics (CFD) model

A computational fluid dynamics (CFD) model was used to obtain the mathematical relation between average and axial velocities in the wind channel described in Chapter 3, i.e. $\mathrm{Re}_D = 0.694\ (\mathrm{Re}_D^x)^{1.0162}$ (see Section 3.4.2). A rectangular flow channel with the same section as the real one, but much longer entrance length (roughly 60 hydraulic diameters) was considered. The reason being that the constant velocity profile used as inlet condition requires a longer length than real one to develop asymptotically. As a matter of fact, the throttling valve in the real channel is an effective turbulence promoter, which makes the developing length much shorter. The numerical model required roughly 2 millions of computational cells in order to obtain mesh-independent results and a special care was used in meshing the boundary layer. In particular, the maximum $y^+ = \Delta y / y_0$ (normalized dimensionless distance of the first cell centroid from the wall) used in the simulations at the maximum Reynolds number was 1.9, i.e. the viscous sublayer ($< 5y_0$) was correctly meshed [106]. The standard $k - \epsilon$ turbulence model was adopted for closing the Reynolds-averaged Navier-Stokes (RANS) equations [106]. Because the near-wall mesh was fine enough to resolve the viscous sublayer, the adopted enhanced wall treatment reduces to the traditional two-layer zonal model [106].

A second model has been developed to compute heat transfer coefficient through the sample. The main goal of this second model was to compute the convective heat transfer coefficient h, under different flow conditions. The numerical simulations were used to support the experimental results obtained by the proposed sensor, at least in case of flat surfaces. Fully developed turbulent velocity profile, obtained from the previous model, was imposed at the inlet of the computational domain. The sample and the guard were modeled as an isothermal surface with a temperature higher than that of air, such that the temperature difference $T_s - T_a$ was roughly the same as in the experimental measurements. In this second model, a length of 0.69 m, was considered because the fully developed inlet profiles were already available. The mesh of the cross section was the same as the previous model. On the other hand, a fine homogeneous mesh with 1 *mm* of grid spacing was chosen along the fluid flow, but close to the upstream edge of the sensor guard, where a finer mesh of 0.1 *mm* spacing was necessary. These choices granted mesh-independent results. Overall, the above numerical model required roughly 6 millions of computational cells.

For both previous models, some simulations were performed for validation purposes in the following range $3 \times 10^4 \leq \mathrm{Re}_D \leq 17 \times 10^4$ (which is consistent with the experiments reported in this work). Assuming the smooth channels, the numerical results were compared in terms of the Darcy friction factor and the Nusselt number against the Blasius correlation and Gnielinski correlation, respectively [38]. The maximum deviations between the numerical results and the phenomenological correlations were 6.7 % and 2.1 % respectively.

B. Data regression procedure

In the following, the details of data regression presented in Section 4.3 are exposed. Being $\{\frac{\Delta Tr_R}{V}\}$ the (9×1) column vector whose i-th component is the value of $\frac{\Delta Tr_R}{V}$ of the i-th sample, we impose:

$$\left\{\frac{\Delta Tr_R}{V}\right\} = [M]\{C\}, \tag{B.1}$$

where $[M]$ is a (9×9) matrix and $\{C\}$ is the (9×1) column vector of model constants defined in Section 4.3. Being $\{M_i\}$, the i-th row of $[M]$, defined as:

$$\begin{aligned}\{M_i\} = \Bigg\{ & \left(\widehat{\lambda_p}\right)_i, \left(\widehat{\frac{A}{A_n}}\right)_i, \left(\widehat{\frac{V}{AY_0}}\right)_i, \left(\widehat{\lambda_p^2}\right)_i, \left(\widehat{\frac{A}{A_n}}^2\right)_i, \left(\widehat{\frac{V}{AY_0}}^2\right)_i, \\ & \left(\widehat{\lambda_p}\right)_i \left(\widehat{\frac{A}{A_n}}\right)_i, \left(\widehat{\lambda_p}\right)_i \left(\widehat{\frac{V}{AY_0}}\right)_i, \left(\widehat{\frac{A}{A_n}}\right)_i \left(\widehat{\frac{V}{AY_0}}\right)_i \Bigg\}.\end{aligned} \tag{B.2}$$

$\{M_i\}$ is a vector containing all the geometrical features of the i-th sample. Being $[M]$ and $\left\{\frac{\Delta Tr_R}{V}\right\}$ known, a vector $\{C\}$ containing the unknown constants of the model could be obtained as:

$$\{C\} = [M]^{-1} \left\{\frac{\Delta Tr_R}{V}\right\}, \tag{B.3}$$

where $[M]^{-1}$ is the inverse of the $[M]$ matrix.

C. Commercial versus optimized heat sink

In the following, a representative commercial micro-protrusion patterned (micro pin-fin) heat sink and the optimized patterns presented in section 4.5 are compared. In particular, the model 662-15 by Wakefield-vette™ extruded heat sink for integrated circuits is chosen as representative commercial heat sink.

Protrusion base edge $d_c = 1.52\ mm$, protrusion height $H_c = 2.4\ mm$, root surface area $A_{n,c} = (43.5)^2\ mm^2 = 1892\ mm^2$, and number of protrusions $N_c = 168$ of the commercial heat sink are extracted from heat sink data sheet [107]. Protrusions volume is calculated as $V_c = d_c^2 H_c N_c = 931.6$ mm^3. Moreover, data sheet [107] reports that 662-15 commercial heat sink experiences, for air velocity $v = 965\ LFM = 4.9\ m/s$, a thermal resistance of $2.2\ K/W$, corresponding to a thermal transmittance $Tr_c = 0.45\ W/K$. The corresponding performance-to-cost ratio is $Tr_c/V_c = 4.88$ $10^{-4}\ W/K/mm^3$.

Values of Tr for the optimized patterns presented in section 4.5 are referred to the root surface area $A_n = 123\ mm^2$. Volume of a 662-15 commercial heat sink characterized by root surface area $= 123\ mm^2$ is $V_c' = VA_n/A_{n,c} = 60.6\ mm^3$, and its transmittance can be estimated as $Tr_c' = Tr_c A_n/A_{n,c} = 0.03\ W/K$. Moreover, fin efficiency of commercial heat sinks (made of aluminum) is nearly 100 % (the same that would be experienced by a copper micro-pin fin heat sink).

Air velocity $v = 4.9\ m/s$ corresponds to a Reynolds number $Re_L = 0.5$ 10^{-4}. Hence 662-15 commercial heat sink will be compared to the optimized heat sink that guarantees $Tr_{opt} = Tr_c' = 0.03\ W/K$ at $Re_L = 0.5$ 10^{-4}. Drawings and design parameters of this optimized heat sink can be found in 1st row of Tab. 4.7, and 3rd row of Tab. 4.4, respectively. Volume of optimal heat sink is $V_{opt} = 36.8\ mm^3$, while the corresponding performance-to-cost ratio is $Tr_{opt}/V_{opt} = 8.42\ 10^{-4}\ W/K/mm^3$.

In conclusion, optimization procedure based on the proposed model leads to enhance Tr/V, i.e. thermal performance per unit production cost, up to 73%, with regard to the considered commercial heat sink.